2014

High-resolution lidar mapping and analysis to quantify surface movement of Swift Creek landslide, Whatcom County, WA

Benjamin R. Ferreira
Western Washington University

HIGH-RESOLUTION LIDAR MAPPING AND ANALYSIS TO QUANTIFY SURFACE MOVEMENT OF SWIFT CREEK LANDSLIDE, WHATCOM COUNTY, WA

By
Benjamin R. Ferreira

Accepted in Partial Completion

Of the Requirements for the Degree

Master of Science

Kathleen Kitto, Dean of Graduate School

ADVISORY COMMITTEE

Chair, Dr. Scott Linneman

Dr. Douglas H. Clark

Dr. Robert Mitchell

Paul Pittman

MASTER'S THESIS

In presenting this thesis in partial fulfillment of the requirements for a master's degree at Western Washington University, I grant to Western Washington University the non-exclusive royalty-free right to archive, reproduce, distribute, and display the thesis in any and all forms, including electronic format, via any digital library mechanisms maintained by WWU.

I represent and warrant this is my original work, and does not infringe or violate any rights of others. I warrant that I have obtained written permissions from the owner of any third party copyrighted material included in these files.

I acknowledge that I retain ownership rights to the copyright of this work, including but not limited to the right to use all or part of this work in future works, such as articles or books.

Library users are granted permission for individual, research and non-commercial reproduction of this work for educational purposes only.

Any further digital posting of this document requires specific permission from the author.
Any copying or publication of this thesis for commercial purposes, or for financial gain, is not allowed without my written permission.

Benjamin Ferreira

November 26, 2014

HIGH-RESOLUTION LIDAR MAPPING AND ANALYSIS TO QUANTIFY SURFACE MOVEMENT

A Thesis

Presented to

The Faculty of

Western Washington University

In Partial Fulfillment

Of the Requirements for the Degree

Master of Science

By

Benjamin R. Ferreira

November, 2014

ABSTRACT

I investigated the applicability of using terrestrial laser scanning (TLS) to quantify surface displacement of the Swift Creek landslide, an active earth flow in the foothills of northwest Washington State. Five surveys were completed from October, 2009-April, 2011 to identify and measure spatial and temporal changes in the movement of the landslide. The seasonally variable movement patterns at the site provide an ideal environment to test the effectiveness of newly emerging methods to measure surface displacement.

Iterative closest point (ICP) analysis and image cross-correlation via particle image velocimetry (PIV) were applied to sequential TLS datasets to identify and match features in multi-temporal data. ICP utilizes a distance-based function to match point-cloud surfaces whereas PIV is essentially a pixel-matching algorithm applied to derived DEMs and slope-gradient images.

Results of the analysis revealed that the ICP and PIV methods applied to LiDAR data are suitable for measuring surface displacement on actively deforming landscapes. Total movement rates of 25 boulders on the toe ranged from 3.3 to 39.3 m/yr, with seasonal changes evident in their movement patterns. PIV analysis produced a spatially continuous displacement field when the time between surveys was less than about five months. Results show that the toe is a highly dynamic zone with as many as five discrete zones of movement.

To gain a better understanding of the overall dynamics of the Swift Creek landslide, I applied PIV analysis to airborne LiDAR acquired in 2006 and 2011 that extended the spatial coverage to the entire basin. Movement rates on the main body of the landslide were 3.0 (+/- 0.9) m/yr over the five years. Using both terrestrial and airborne LiDAR data allowed me to circumvent the limitations of each to quantify movement across the whole landslide. My data suggests that the landslide undergoes a transition from a predominately sliding mass in its upper portion to a flow near the top of the unvegetated toe based on increasing velocity and more variable movement patterns observed in this area.

TABLE OF CONTENTS

LIST OF FIGURES

1. INTRODUCTION

Earth flows are a common type of mass movement that generally occur in mountainous regions underlain by weak, fine-grained rocks (Savage and Baum, 2005). As defined by Hungr et al. (2001), earth flows are slow-moving slope failures that slide along transient shear boundaries and deform internally, forming a flow-like mass. While movement is often continuous, it is rarely steady. Differences in surface lithology and slope can cause zones of the slide to behave differently; whereas changes in precipitation can cause the whole mass to accelerate or even stop in some cases (e.g., Iverson and Major, 1987; Coe et al., 2003; Daehne and Corsini, 2012). In extremely rare instances, heavy precipitation can destabilize an earth flow and cause a catastrophic collapse (e.g., Geertsema et al., 2006). By affecting the timing, magnitude and grain size of the sediment entering fluvial systems, earth flows can cause dramatic changes in sediment budgets (Mackey and Roering, 2011). The increased sediment load can create secondary hazards, such as flooding, that extend miles downstream.

The monitoring of earth flows is important in hazard mitigation and risk reduction for two reasons: (1) to identify, observe and quantify changes in the hazards associated with unstable slopes; and (2) to develop a better understanding the conditions and triggers that lead to slope failures (Brückl et al., 2006; Corsini et al., 2005). A common approach when monitoring slopes for movement involves the measurement of surface deformation, which is a primary indicator of slope instability. Displacement measurements can be used to indicate the direction and rate of movement and can be interpreted to infer the mode of movement and slip surface geometry (Teza et al., 2007). Changes in velocity can help identify the mechanisms that drive the transition from earth slides to earth flows (Daehne and Corsini,

2012). Furthermore, landslide displacement is important in identifying failure patterns as it allows for the estimation of strain rates and deformation patterns (Teza et al., 2007). A key component in measuring surface displacement is the need for accurate and precise geospatial data.

Advances in geospatial technology have improved the monitoring and detection of earth flows by increasing the accuracy and spatial and temporal coverage of data. Because working on unstable slopes is an inherently difficult proposition and in many cases not feasible, methods of remotely acquiring data have become popular in earth flow analysis.

The monitoring of earth flows typically involves either frequent GPS-based measurements of particular points or infrequent, basin-wide surveys of the surface topography using remote sensing. These options generally offer increased spatial coverage at the expense of temporal coverage (in the latter case) and the opposite for the former. In situ tools (such as GPS) can provide very accurate and precise data with continuous temporal coverage. For example, monitoring of the Slumgullion earth flow in Colorado used a total of 30 GPS stations (11 on stable terrain and 19 on the landslide) and other field instrumentation (extensometers and piezometers) to document the relationship between seasonal variations in earth flow velocities and changes in precipitation (Coe et al., 2003). Considering the spatial and temporal variability in the movement of earth flows, it is reasonable to question whether such a limited number of points are representative of overall movement on such large earth flows.

Alternatively, airborne LiDAR technology has been applied in numerous studies to provide spatially complete data to detect, monitor and analyze the kinematics of earth flows (Derron and Jaboyedoff, 2010; Kasperski et al., 2010; Mackey and Roering, 2011; Prokop and

Panholzer, 2009). Although these studies expand the spatial coverage to include the entire earth flow, they typically do so at the expense of temporal resolution. Given the seasonal variability documented in deep-seated earth flows (Coe et al., 2003), sporadic basin-wide geodetic surveys may miss key kinematic events that affect the behavior and sediment production of the slide.

Space-based interferometric synthetic aperture radar (InSAR) is another promising remote-sensing platform to measure surface displacement. InSAR provides accurate and spatially complete data coverage, but has issues resolving displacement rates greater than about 10 cm per month (Aryal et al., 2012). Some rapid earth flows may move several meters per second (Petley and Allison, 1997), but even creeping landslides often move faster than InSAR can resolve. Given the wide range of surface displacement in active earth flows, LiDAR and InSAR both have difficulty resolving the entire spectrum of earth flow motion. The dynamic movement of slow-moving material makes earth flows an ideal environment to test other newly emerging methods to quantify surface displacement.

Terrestrial laser scanning (TLS) or ground-based LiDAR comprises a portable unit that can rapidly and precisely survey large swaths of land at centimeter-scale resolution. By offering complete spatial coverage and the ability to quantify a wide range of surface displacements, TLS has become increasing popular to monitor and characterize earth flows. Using an adapted application from fluid dynamics, Aryal et al. (2012) was able to apply a cross-correlation method to multi-temporal TLS data of the slow Cleveland Corral landslide in California to calculate spatially complete surface displacement fields. The author utilized particle image velocimetry (PIV) software, applied to greyscale slope-gradient image pairs

derived from digital-elevation models (DEMs) to quantify net displacements (of less than five meters) on a reactivated landslide. The PIV application is a promising tool studying landslide kinematics, yet it has been applied sparingly.

This thesis describes a methodological approach to measure surface displacement using TLS and PIV at earth flows, using the Swift Creek landslide in Washington State as a case study (Figure 1). More accurately defined as a complex earth slide – earth flow, the site provides a complex geomorphic environment to test the effectiveness of using TLS for landslide deformation analysis. Although numerous studies exist involving TLS methods and landslide applications (e.g., Abellán et al., 2006; Kasperski et al., 2010; Teza et al., 2007), few have been conducted in densely forested regions such as the Pacific Northwest, where the benefits of remotely acquired data can be substantial.

The Swift Creek landslide poses a documented health and safety risk to local residents (Schreier and Lavkulich, 2007). Future sediment management efforts include will need to account for the large volume of sediment being produced by the landslide (Whatcom County Public Works, 2012). Previous studies at the field site have documented the behavior of the earth flow between 2002 and 2003 using GPS (McKenzie-Johnson, 2004). This project expands on past efforts in terms of spatial sampling, duration and precision in hopes of better understanding the transfer of material at the site. To this end, I also incorporated two airborne LiDAR datasets to extend the spatial coverage to include the main body of earth flow.

1.1. Research Objectives

The primary goal of this project is to develop a method to acquire and apply terrestrial LiDAR data to analyze geomorphological change at the actively deforming toe of a large landslide. Using the Polyworks software suite from Innovmetric (Innovmetric, 2010), I processed unorganized single scans into georeferenced point clouds. Using a best-fit application within the Polyworks software, based on iterative closest point (ICP) matching, I quantified the displacement of 25 individual boulders on the landslide. In order to create a more spatially complete displacement map, I chose to apply PIV to both TLS and airborne LiDAR to achieve a better understanding of the limitations and challenges with collecting and synthesizing terrestrial LiDAR data, as well as monitoring overall surface displacement at a difficult to monitor site.

In order to accomplish the research objectives outlined above, I developed a method to acquire and process high-resolution terrestrial LiDAR data for complex change detection. This thesis will:

- Provide a brief background on earth flows, LiDAR and processing 3D data
- Describe the methods used to acquire and process terrestrial LiDAR data
- Apply PIV analysis to LiDAR surface data to measure displacement
- Utilize data to measure displacement using an automated surface matching program
- Create DEMs to compare changes in ground surface elevation and to investigate volumetric changes at the site

2. BACKGROUND

2.1. Earth flows

Landslide is a general term for the mass movement of soil or rock which occurs on slopes where the resisting strength of the slope material is surpassed by gravity acting on the material. When these slopes fail, they typically do so along zones or planes of weaknesses in the underlying material at depths ranging from a few centimeters to more than 100m. This thesis focuses on the kinematics of a deep-seated landslide, with a failure plane deeper than 5 meters (Petley and Allison, 1997).

Landslides are relatively common in areas with high topographical relief. Changes in external forces such as tectonics, climate or land use can affect the sometimes delicate balance between resisting forces and gravity. Factors that cause slope failures are numerous and include both natural and man-made elements. Daehne and Corsini (2012) described the three main variables: underlying factors, such as steep slopes or weak geological formations; secondary factors such as changes in land-use or extensive weathering; lastly, triggering factors, such as intense rainfall or seismic activity that occur immediately before failure. Several of these factors often act in conjunction to cause slope failure. During periods of uplift or increased precipitation, for example, fluvial incision increases due to greater stream power; as the river channel incises, the slope of the hillside becomes steeper until the slope is no longer stable. At that point, mass wasting processes activate and remove material and reduce the slope angle.

Landslides can be classified based on the Cruden and Varnes (1996) classification scheme which uses the mode (fall, topple, slide, flow, etc.), the type of material (bedrock, soil) and the rate of movement, ranging from a few millimeters per year (extremely slow) to several meters per second (extremely fast), to categorize mass movements. Since there are a variety of mass-wasting movement styles occurring simultaneously at the project location, a brief description of the two most prevalent modes, slides and flows, are briefly summarized below.

SLIDES

The term slide refers to the downslope sliding of material (e.g., bedrock, soil, or both) over a distinct failure surface that separates the stable material below from the unstable material above (Cruden and Varnes, 1996). The sliding mass is separated from the underlying material by a rupture surface or a thin zone of intense strain, the result of shear failure within the weak zone (Cruden and Varnes, 1996). Slides typically fall into one of three classes: rotational, translational, or a combination of the two.

Translational slides have an underlying failure surface that is nearly planar, with very little rotation or tilting of the sliding mass. The failure surface is often along geologic discontinuities such as bedding planes or the boundary between soil and rock. Translational slides also tend to be shallow and involve only the upper few meters of material.

Rotational slides have an underlying failure surface that is curved and concave. Their movement is roughly rotational, with the center axis parallel to the ground surface. Due to the nature of concave rupture surfaces, rotational slides tend to incorporate deeper material than translational slides.

FLOWS

The term flow refers to a viscous mass of material that exhibits internal deformation in which shear surfaces are closely spaced, short-lived and usually not preserved (Cruden and Varnes, 1996). The flowing mass is separated from the underlying material by a zone of weakness, the result of shear failure within the weak zone. The main difference between slides and flows is the mobility of the material, which is usually a direct result of water content. Internal deformation of the material (as opposed to sliding along the margins and the presence of slickensides) can be used to differentiate flows from slides.

Some landslides, such as the Swift Creek landslide in this study, have attributes of both slides and flows thus, can be defined as a composite earth slide-earth flow. For simplicity's sake, the term earth flow will be used herein to describe earth slides, earth flows and composite earth slide-earth flows.

2.2. Basics of LiDAR

A number of methods have traditionally been used to monitor landslides. The array of methods can generally be divided into point-based and surface-based techniques. The point-based methods, such as GPS or total station surveying, generally acquire reliable data, but provide sparse spatial coverage and require physically surveying each data point. On the other hand, surface-based methods such as photogrammetry or satellite interferometry cover a much larger area with a higher sampling density, but also with less precision, particularly in heavily forested areas. Over the past decade, Light Ranging and Detection (LiDAR)

technology has emerged as one of the best tools to achieve a high point sampling density along with a high degree of certainty.

LiDAR is a remote sensing technology that consists of a laser transmitter and an optical detector which work in tandem to determine the travel time of reflected pulses. Both airborne and terrestrial LiDAR are based on the same time-of-flight, laser-based distance measuring technology (Lichti et al., 2002). Thousands of pulses per second are emitted towards the target at a direction characterized by azimuth and zenith angles. The reflected pulse is recorded; the total travel time is divided in half and then converted into a distance by multiplying the travel time by the speed of light. In this matter, the Cartesian coordinates (*x, y, z*) of the reflected points can be logged. Stationary terrestrial scanners use internal mirrors to incrementally move the laser beam to cover a large area (Oppikofer et al., 2009), whereas airborne units are mobile. In both instances, a broad area can be surveyed quickly with high precision.

LiDAR technology is highly useful in landslide monitoring because it can provide accurate surface elevation data at a high spatial resolution. Beginning in the early 1990s, LiDAR systems have typically been mounted to planes and flown several hundred meters above the ground surface. Over the past decade, terrestrial and unmanned aerial-based versions have emerged to offer precise three-dimensional data with a high spatial resolution that has so far been unsurpassed. The ability to detect movement on the order of centimeters over a large area makes this technology appealing for landslide studies in remote and hard to reach areas.

A key difference in the two modes of acquiring LiDAR data is the ability to filter out undesirable data. Although both airborne and terrestrial LiDAR are able to return multiple

data pulses (e.g., first returns, last returns), the elevated scanning position of airborne LiDAR allows for better penetration of vegetation and a high likelihood of hitting the ground surface. In the case of terrestrial LiDAR, the laser has a difficult time penetrating vegetation due to the oblique scanning angle and therefore the operator must be careful to scan from a location that is clear of obstructions

The use of airborne and terrestrial LiDAR to characterize landslide deformation is widespread and has many applications ranging from landslide identification and mapping (Glenn et al., 2006; Jaboyedoff et al., 2012) to monitoring earth flow (Corsini et al., 2009) and rockfall displacement (Abellán et al., 2006). In most cases, the dense 3D point data are interpolated to create a raster-based DEM or a vector-based triangulated irregular network (TIN) and used to detect changes in elevation, which are attributed to areas of net accumulation or depletion of slide material. Although valuable for volumetric change estimates, such interpretations are limited in scope because they are unable to resolve surface displacement velocities or vectors which are better indicators of movement than changes in elevation (Teza et al., 2007).

A common approach to measuring changes using LiDAR data is when two datasets (acquired at different times and covering the same area) are simply subtracted from one other to create a so-called DEM of difference (Schwab et al., 2008). However, interpreting landslide deformation through elevation data alone is less desirable than using surface displacement data since it is unable to resolve the lateral component of motion which is inherently important to characterizing earth flows that are driven largely by sliding along a basal shear surface (Savage and Baum, 2005). Furthermore, translation rates can be used to estimate

deformation patterns, strain rates and can been used in earth flow modeling (Malet et al., 2005; Teza et al., 2007).

2.3. Aligning and transforming 3D data

The reference frame of TLS data is typically based on the location of the instrument so that changes in the physical position of the scanner, result in a change to the reference system. For this reason, data sets acquired from different scan positions need to be rectified so that the disparate reference systems are aligned.

In a three-dimensional (3D) dataset, the position of every data point *(p)* can be described in a 1x4 matrix (Equation 1), using *x*, *y* and *z* values based on the distance to the origin of the coordinate system being used (Teza et al., 2007).

$$p = \begin{vmatrix} x \\ y \\ z \\ 0 \end{vmatrix} \quad [1]$$

A key advantage to using matrices to describe the transformation of points is the ability to multiply and add or subtract matrices from one another. In this manner, the change in position (Δp) from position *a* to position *b* can be characterized as follows in Equation 2.

$$\Delta p = \begin{vmatrix} x_b \\ y_b \\ z_b \\ 0 \end{vmatrix} - \begin{vmatrix} x_a \\ y_a \\ z_a \\ 0 \end{vmatrix} = \begin{vmatrix} x_b - x_a \\ y_b - y_a \\ z_b - z_a \\ 0 \end{vmatrix} \quad [2]$$

When dealing with assembled point clouds (*P)*, the point clouds retain their initial reference system during multi-temporal alignment (e.g., assembled point clouds are based on their own local coordinate system). When the point clouds are aligned to other datasets (via 3D transformations), the coordinate system of the assembled point clouds are transformed in the alignment process. The 3D transformation (*T*) that best describes the change in position of the assembled point clouds (determined by ICP matching, Section 2.4) can be characterized in a 4 x 4 transformation matrix, with values of *m* (Equation 3).

$$T = \begin{vmatrix} m_{11} & m_{12} & m_{13} & m_{14} \\ m_{21} & m_{22} & m_{23} & m_{24} \\ m_{31} & m_{32} & m_{33} & m_{34} \\ m_{41} & m_{42} & m_{43} & m_{44} \end{vmatrix} \quad [3]$$

The transformation of datasets is accomplished via translation (i.e., shifting), rotation and scaling. A significant advantage of using a 4x4 matrix to describe these transformations is the ability to describe the three modes of transformations within a single matrix. Considering the aim of this project is measuring displacement (i.e., translation), I will not focus on the rotational or scaling aspects of the transformation matrix.

The values defining the translation of rigid bodies (*t)* along each axis are contained in the fourth column of the 4x4 matrix (Equation 4).

$$T_t = \begin{vmatrix} 0 & 0 & 0 & t_x \\ 0 & 0 & 0 & t_y \\ 0 & 0 & 0 & t_z \\ 0 & 0 & 0 & 0 \end{vmatrix} \quad [4]$$

A simple alternative to manually differencing the alignment matrices (ΔP) is to reset the alignment matrix of the "before" point cloud (P_a) to the origin of the coordinate system (i.e., zero) before aligning it to the reference point cloud (See Appendix). Using this approach, the alignment matrix of the newly aligned dataset (P_b) will reflect the change in position without the need to subtract the original alignment matrix (Equation 5).

$$\Delta P = \begin{vmatrix} x_b \\ y_b \\ z_b \\ 0 \end{vmatrix} - \begin{vmatrix} 0 \\ 0 \\ 0 \\ 0 \end{vmatrix} = \begin{vmatrix} x_b \\ y_b \\ z_b \\ 0 \end{vmatrix} \quad [5]$$

By tracking changes in the respective 3D transformational matrices of the datasets, I hope to be able to quantify changes in the 3D position of unstable features on an earth flow.

2.4. Surface matching applications

A necessary component of measuring displacement is the ability to resurvey identifiable features (e.g., benchmarks) over time. With LiDAR data, this is not a simple task since the data are acquired remotely. Furthermore, with LiDAR data there is no way of knowing if subsequent surveys will capture the same points since data are collected over an area with a resolution that is often expressed in terms of points per square meter. The likelihood of capturing identical points in subsequent surveys is quite low. For this reason, it is necessary to compare surfaces.

Two approaches to comparing surfaces were used in this study: (1) a point cloud matching application which applies an ICP algorithm to align 3D point data based on the distance between neighboring points and (2) a pixel intensity-based cross-correlation application (PIV) that identifies corresponding surfaces in greyscale slope-gradient image pairs (derived from DEMs) based on the similarity of the surrounding pixel intensities.

The ICP method is based on a two-step matching and transformation process (Teza et al., 2007) that follows an initial rough manual alignment. In the first step, for each point in point cloud *A*, its nearest neighbor is found in point cloud *B*. The transformation to achieve the alignment is carried out and the square root of the sum of the squared distances (RMSD) between nearest neighboring points is calculated. The two steps continue in an iterative process until the RMSD falls below a defined threshold. In this project, the ICP procedure was used extensively to align contemporaneous and multi-temporal TLS data for displacement analysis.

Particle image velocimetry uses a DEM-based, cross-correlation mathematical function to align images via horizontal and vertical (2D) shifts to maximize the similarity of pixel intensity values in a region using statistical analysis (Raffel et al., 2007). In practical terms, the application uses two greyscale slope-gradient images derived from DEMs of the same area (at different times) and applies 2D shifts to each cell in one image to find the corresponding pixel intensity in the second image. Originally designed for fluid dynamics in the 1980s, it has only recently been applied to earth flows (e.g., Aryal et al., 2012; Daehne and Corsini, 2012) and geotechnical studies involving soil strength (White et al., 2003).

The applicability of PIV to earth flow studies is based on the assumption that the earth flow morphology has remained mostly intact, either due to low deformation rates or frequent surveys. While exact features (such as mounds or large rocks) are subject to change over time (from rotation or differential movement), larger scale derivative features such as aspect, slope or surface roughness are more likely to retain their shape (Daehne and Corsini, 2012). For example, an erosional gulley or ridgeline on an earth flow is subject to displacement and perhaps some deposition and erosion; however, the general shape of the feature is likely to be retained. In this manner, PIV is able to track the changes in position (*x, y)* of these features by correlating the derived greyscale pixel values (ranging from 0-254) of the features at different times. Although a number of derivative factors such as topographic aspect, surface roughness or hill-shade values can be used in PIV, greyscale slope-gradient images have been found to be the most reliable for correlation (Daehne and Corsini, 2012). In this study, I follow this recommendation and use greyscale slope-gradient calculations from airborne and terrestrial LiDAR data sets to apply PIV to movement of Swift Creek landslide.

3. STUDY AREA AND GEOLOGIC SETTING

3.1. Study Area

The Swift Creek landslide in Washington State is located within the upper watershed of the South Fork of Swift Creek (referred to simply as Swift Creek). Active for at least the past 80 years, the landslide sends large quantities of sediment down Swift Creek and into the small, low-gradient Sumas River resulting in channel-in-filling and the potential for more frequent and severe flooding (Bayer and Linneman, 2011). Adding to the potential hazards, large quantities of naturally-occurring (chrysotile) asbestos occur in the landslide, the result of extensive weathering of the parent material, serpentinite (Bayer and Linneman, 2011). In the past, dredging was used extensively by local property owners and the county in an attempt to keep Swift Creek within its channel. However, after extensive sampling in 2007, the Environmental Protection Agency issued a report which classified the material as hazardous sediment and recommended that dredged material no longer be transported away from the site due to health and liability concerns (Schreier and Lavkulich, 2007). As a result, there has been a renewed interest by the local government in long-term mitigation to reduce the volume of sediment reaching the creek (Whatcom County Public Works, 2012).

The landslide is located along the western margins of the North Cascades mountain range in Northwest Washington State, situated on the western slopes of Sumas Mountain at an elevation ranging from 900-2400 feet (Figure 1). The climate of the area can be summarized as having mild, wet winters and cool, dry summers (Figure 2). As a result of the cool, damp

climate, large coniferous trees and a thick understory of plants cover the study area, except for the largely unvegetated toe of the landslide (Figure 3).

3.2. Geology

The study area lies within the complex continental margin of the Pacific Northwest. Convergence of the Juan de Fuca Plate beneath the North American Plate and shearing along the Pacific-North America Plate boundary provides the overall mechanism for regional uplift and deformation (Verdonck, 2006). Furthermore, the Puget Sound region serves as a distributed deformation zone that accumulates compressional strain as the Olympic Mountains move northeast relative to the Cascade Range (Miller et al., 2001).

There are two primary bedrock units in the area (Figure 4); the older is a pre-Tertiary ultramafic unit composed primarily of serpentinite (Dragovich et al., 1997). Away from the landslide, this formation is mostly non-serpentinized peridotite and dunite, indicative of extensive alteration of the unit around the landslide. The ultramafic formation is unconformably overlain by late Eocene continental fluvial deposits of sandstones and conglomerates known as the Huntingdon Formation (Dragovich et al., 1997). The bedrock deposits are overlain by alluvium, glacial till and landslide deposits (Dragovich et al., 1997).

3.2.1. Geomorphology

Considered large for landslides in the region, the slide has an estimated volume of 40 million cubic meters (McKenzie-Johnson, 2004). It is 1.4 km in length from the top of the accumulation zone to the toe and approximately 400 m wide. The source area of the landslide

is marked by scarps and extensional features indicating the landslide is retrogressing into an older, inactive slide deposit. Presumably a dormant post-glacial landform, the Swift Creek landslide was probably reactivated shortly before the first aerial photographs taken in 1940 (McKenzie-Johnson, 2004). The exact cause of reactivation is unknown, but changes in land-use, excessive rain, and seismic activity are all possibilities. .

The morphology of the basin differs somewhat from the textbook hourglass earth flow morphology described in Keefer and Johnson (1983). Instead of an amphitheater-like source area and a narrow transport zone, the landslide is lobe shaped with maximum widths (~450 m) near the center of the slide. The toe zone is also anomalous in that it is being constricted by a narrowing bedrock canyon causing pronounced steepening and bulging since the material is unable to spread laterally. McKenzie-Johnson (2004) hypothesized that this steepened toe has been the source of debris flows triggered in the recent past, leading to infilling of the channel below the landslide (Figure 5). The geomorphologic impact of the landslide is apparent; below the landslide the original v-shaped valley has been filled with sediments.

The landslide consists of two main components, as defined in this study: the main body and the toe. The main body is thickly forested with intact soils, but variably tilted trees. The toe is mostly unvegetated and consists of weak, unconsolidated sediments, the exception being an area of conglomeratic blocks along the northern portion of the toe known locally as the Huntingdon blocks (Figure 6).

3.2.2. Previous work at the Swift Creek landslide

The Swift Creek landslide has been the focus of several studies in recent years. The landslide was monitored from June 2002 through July 2003 using GPS (McKenzie-Johnson, 2004). The study found that the main mass of the landslide was moving about 4 m/yr, with some areas on the unvegetated toe moving more than 20 meters in a single year (McKenzie-Johnson, 2004). McKenzie-Johnson concluded that the basal slide plane of the earth flow is rooted near the contact or within the serpentinite unit at a depth of approximately 100 meters. He further hypothesized that observed temporal differences in surface velocities were likely due to changes in groundwater levels, which seems reasonable given the climate of the area and previous work such as Iverson and Major (1987).

The toe of the landslide is largely composed of loose and unconsolidated sediments ranging in size from clay to boulder and composed of serpentinite and conglomerate (Bayer and Linneman, 2011). Mineralogical analysis (using X-Ray Diffraction and Scanning Electron Microscope) of the fine-grained sediment indicates that the serpentinite weathers to form predominately asbestiform chrysotile with minor amounts of chlorite, illite and hydrotalcite (Bayer and Linneman, 2011). The study also estimated that chrysotile constitutes more than 50% (by volume) of the suspended sediment load in Swift Creek.

Previous research has raised interesting questions regarding the balance between erosional and depositional processes on the toe and how seasonal fluctuations in moisture affect each (McKenzie-Johnson, 2004). Furthermore, there is uncertainty regarding the sediment production from the landslide which is a primary concern for secondary hazard mitigation. An early study, produced in 1965, compared their survey data with previous topographic

maps and estimated 94,000 m^3 of annual sediment production (Whatcom County Public Works, 2012). A 2008 study used previous grain size analysis and bedload estimates derived from cross-sectional surveys of Swift Creek on the alluvial fan below the landslide to estimate 37,700 m^3 of bedload sediment production. A distinct limitation of the second estimate is that it does not account for the substantial flux of fine-grained sediment that bypasses the alluvial fan (Bayer and Linneman, 2011). An alternative method to estimate sediment production from the landslide has been to measure the suspended sediment moving through the creek downstream of the landslide. Using discharge and sediment concentration measurements, along with precipitation data, modeling has suggested an erosion rate of approximately 1 m/yr averaged over the toe (Bayer and Linneman, 2011).

4. METHODS

To constrain the movement rates and patterns at the Swift Creek landslide, I used terrestrial LiDAR data to quantify surface displacement via surface matching applications. The terrestrial LiDAR data were acquired in five separate field campaigns between 2009 and 2011. Focused around the toe of the landslide, the data provide precise and detailed information on the displacement patterns over 18 months. Twenty-five boulders on the toe were identified and isolated in each of the five campaigns and their 3D changes in position quantified to measure surface displacement across the toe of the slide. Slope gradient images were derived from the TLS datasets and used in PIV analysis to increase the spatial coverage from 25 individual boulders to the entire toe. Using DEMs created from each of the datasets, a digital image differencing technique was applied to the geospatial data to discern changes in elevation. Incorporating horizontal and vertical movement patterns allows for a detailed investigation of the relationships between velocity and the mass transfer of material from the source zone to the toe of the landslide.

My approach combined field and computer processing techniques to measure vertical and horizontal surface displacement at the Swift Creek landslide. I acquired and processed terrestrial LiDAR data to create georeferenced datasets and developed gridded DEMs from the datasets. Ultimately I compared the datasets to evaluate the ongoing kinematic patterns.

4.1. LiDAR Data

The collection of high quality LiDAR data requires significant planning and quality control to ensure data integrity. In this study, it was critically important given the extensive use of interpolated maps. This section describes the process by which the data was acquired and processed to produce georeferenced point data and DEMs.

4.1.1. Terrestrial LiDAR

The methodology, collection and processing of terrestrial LiDAR data have been described in a number of publications (e.g., Baldo et al., 2009; Derron and Jaboyedoff, 2010; Prokop and Panholzer, 2009). This section provides a detailed description of the procedure used in the collection of TLS data for this study.

DATA ACQUISITION

Scanning Locations

In order to provide maximum spatial coverage, I established four scan sites around the toe of the landslide to collect TLS data (Figure 7). Each scanning location had to meet the following basic criteria:

- be accessible on foot and be within the working range of the TLS (~800 meters).
- provide a clear view of the landslide with minimal vegetation in the foreground

Furthermore, at least one of the sites must include a view of stable features that will serve as control points to align future campaigns.

A number of additional factors were taken into consideration during site selection to minimize the introduction of errors into the data collection process. An important consideration was the issue of the laser beam "footprint" (the size of the laser beam when it reaches the target). When a beam is emitted, the diameter of the beam increases over distance in a principle known as beam divergence. For the Optech Ilris 3D scanner, the footprint of the laser beam is 22 mm @ 100 meters (Optech, 2009), but at 500 meters the footprint increases to nearly 100 mm. This is significant because the reflected point may not be located in the center of the footprint, but will be recorded as such. Therefore, any increase in the size of the footprint results in a decrease in the accuracy of the data. For this reason, minimizing the distance from the scanner to the target is essential to maintain the accuracy specified by the manufacturer.

A second concern with respect to the beam footprint is the angle at which it hits the ground, known as the incidence angle. Because a beam is not a two-dimensional line, but rather a three-dimensional cylinder, the shape of the footprint is circular only when the surface is perpendicular to the beam (Wawrzyniew, 2007). When the beam is not perpendicular to the surface, the footprint of the laser increases as the shape becomes more elliptical. Therefore in areas with moderate to low slopes, elevated scanning sites provide the maximum angle of incidence (Prokop 2008).

Georeferencing network

A network of three artificial targets was installed on tree trunks around the toe of the landslide to provide global positioning of the first survey (Figure 8). Although tree trunks are not necessarily stable features (i.e., they sway in the wind), I concluded that targets placed relatively low (less than about 7 meters above the ground), combined with non-windy weather on the day of the survey would negate the potential for movement. Subsequent surveys were then aligned to the georeferenced dataset using the stable trees and terrain that surround the landslide (Figure 9).

Because of the thick forest canopy in the study area, a survey grade GPS unit and a total station were used to measure the coordinates of the elevated targets. A single temporary benchmark was installed on the northern portion of the toe, in an area with an open view of the sky and within 100 meters of the target locations. Absolute positioning of the benchmark was attained using a Trimble 5700 survey-grade GPS. A static GPS campaign was then conducted over 72 hours in order to establish a precise position for the benchmark. Even though the benchmark was located on the slide, the survey was conducted during the dry months and in an area that appears to be moving slower than the rest of the toe. Immediately following the GPS campaign, a total station was setup over the benchmark and used to record the positions of the three targets relative to the benchmark.

Differential post-processing of the raw GPS data was carried out via online service by the Canadian Centre for Remote Sensing's online global GPS processing service (CSRS-PPP, 2009). Uncertainty in the position was reported as standard deviation. The horizontal accuracy was estimated to be 2 – 4 mm and the vertical accuracy 11 mm. The corrected data

were reported in latitude, longitude and elevation (meters) in the NAD83 datum and the Canadian Spatial Reference System (CSRS) projection. In order to more easily incorporate the total station data, the coordinates were converted to UTM Zone 10 North (NAD83). A Leica total station was used to measure the distances from the benchmark to the center of each artificial target (Table 1).

Data Collection

TLS data were gathered during five separate campaigns from October 2009 through April 2011 using an Optech Ilris 3D-Extended Range scanner (Figure 10). During each campaign, between one and four scans was completed from each of the four scanning sites (Table 2). The campaigns were completed in a single day to minimize the effects of the moving landslide.

The most important parameter that is defined during TLS data collection is the point sampling density, known as point or spot spacing. According to the manufacture's specifications, the Optech Ilris 3D is able to measure a minimum point to point spacing of 2 mm @ 100 meters. However, as was just discussed, the footprint of the laser beam at 100 meters is eleven times larger (22 mm), making it impossible for the scanner to rigorously discern points at such a tight point spacing. Therefore scanning with such a high density is unnecessary because the actual spatial resolution is limited by the size of the footprint. Conversely, scanning with a low point density is also undesirable since information could be lost, resulting in a low-resolution terrain model. With this in mind, Lichti (2006) was able to establish an ideal point spacing of 86% of the beam width. In my study, spot spacing ranged

from 13.4 mm to 74.6 mm and nearly every scan was acquired with a spot density less than the 86% threshold to expedite data acquisition and to limit the total number of data points.

The raw range accuracy for the instrument is listed as 7 mm @ 100 meters (μ_{tls}) at the one-sigma level, meaning that 68% of the time, the recorded distance will fall within 7 mm of the actual distance. While recording accuracies at this precision is standard practice in the laser scanning industry, accuracy in this project is reported at the 95% confidence level (or 2*x* standard deviation).

DATA PROCESSING

The approach to processing raw TLS data into a georeferenced (*x, y, z)* dataset relies on several steps due to the large number of unorganized data points. For this study, Innovmetric's Polyworks (v11) software suite (Innovmetric, 2010) was used to process and analyze the point cloud data. The steps are summarized as follows:

- Remove unwanted vegetation and outliers
- Align contemporaneous scans to produce a three-dimensional model
- Georeference a single dataset using the artificial targets with known coordinates
- Align the other assembled point clouds to the georeferenced dataset using stable features

Manually removing undesirable data points is a straightforward (although laborious) task. Removing a large obstruction, such as a tree, is straightforward; however removing small

obstructions such as blades of grass is impractical. Every effort was made to remove trees and bushes, but removing all vegetation was beyond the scope of this project.

Aligning contemporaneous scans

Aligning contemporaneous multi-scan data in Polyworks IM-Align (Innovmetric, 2010) was based on two steps; a rough semi-manual alignment and a more refined automatic alignment process. Initial alignment was achieved by manually selecting three common points in overlapping regions of each scan. The second step relied on an ICP algorithm to further refine the alignment process by effectively matching surface features and then minimizing the distance between the corresponding points.

Errors in the final alignment process were reported as the mean (μ) difference between neighboring points and the uncertainty as standard deviation values (σ). In this study, errors associated with aligning contemporaneous scans (μ_{local}) were less than ±0.5 mm and standard deviation values (σ_{local}) ranged between 0.6 mm and 5.4 mm, with an average of 3.78 mm (Figure 12). These standard deviation values include the instrumental measurement errors (μ_{tls}). A visual inspection of the aligned data also shows good alignment (Figure 13).

Georeferencing the assembled point-cloud

After aligning the disparate scans into a single point cloud, the dataset was transformed into an absolute coordinate system. This was accomplished by identifying the artificial targets in the LiDAR data and assigning them the Latitude/Longitude coordinates that were measured in the field. An automated best-fit procedure within the IMInspect application (Innovmetric, 2010) was then used to fit the LiDAR points to their respective global coordinates (See

Appendix). Errors were reported as the mean difference between the projected data point coordinates and their absolute coordinates. Using this procedure, the georeferenced dataset (from May, 2010) had a mean deviation value of 2.4 cm.

Aligning multi-temporal scans to the georeferenced dataset

Once the May 2010 dataset was georeferenced, the other campaigns were aligned to it using a similar ICP procedure as outlined by Monserrat (2008). Using Polyworks IM-Inspect, I isolated and aligned stable areas in corresponding campaigns using the automated surface matching feature (via ICP) in Polyworks (Figure 9). In this project, a section of mature conifer forest on the hillside adjacent to the landslide provided stable and common features to use for alignment in sequential campaigns (Figure 8). This was done to utilize the automatic point matching algorithm, which has a much lower uncertainty than the best-fit procedure using artificial targets due to the large number of data points. In order to take full advantage of ICP matching, all data points other than the stable tree trunks were ignored so that the non-stable data points wouldn't negatively affect the matching process since it is based on the distance between all neighboring points. The ICP matching application was then able to align the disparate campaign datasets together using the stable tree trunks and exposed ground surface as common reference features. The result was a time series of 3D georeferenced datasets that were aligned to each other.

Verification of Alignment

In order to verify the accuracy of the alignment, a large, stable boulder at the base of the landslide was omitted during the alignment process. After the multi-temporal datasets were aligned using the stable terrain on the north side of the landslide, the rest of the data were

recovered and a change analysis was completed on the stable boulder using a point-to-point comparison in Polyworks (Table 3). Standard deviation values ranged between 6 mm and 10 mm which is representative of the overall accuracy of the alignment process. The final errors associated with aligning sequential datasets are higher than aligning individual scans (σ_{local}) because the alignment is performed on assembled point clouds and therefore includes σ_{local}.

4.1.1. Airborne LiDAR

The 2006 airborne LiDAR dataset was collected by the US Geological Survey as part of the North Puget Sound LiDAR Consortium around May 8, 2006. Using a Leica ALS-50 LiDAR system, data were meant to be gathered in accordance with the Federal Emergency Management Agency's (FEMA) standards for "standard" resolution LiDAR data. The survey covered 4,490 km^2 of Whatcom and Skagit counties with a fairly low nominal point density of 1.4 m^2. Vegetation was removed by the vendor prior to delivery. Based on FEMA standards, the contract specified a horizontal accuracy of 1 m or better and a vertical accuracy of 18.5 cm in bare areas and 37 cm in vegetated areas (USGS, 2006). Upon verification of the survey, it was determined that the data did not meet the FEMA standards.

In order to verify the accuracy specifications, GPS coordinates were collected by the vendor from 60 sites within the survey area. The ground control points indicate a root mean square vertical error of 16.9 cm, less than the maximum acceptable value of 18.5 cm. The ground control points were collected in open areas however, and further analysis of the survey conducted by the USGS suggests the actual RMSE is closer to 30 cm in densely forested terrain (USGS, 2006).

The bare earth data were provided in gridded ASCII text format, containing *x, y, z* coordinates for each point. The data were provided in Washington State Plane North projection (U.S Survey Feet, NAD83 horizontal datum, NAVD88 vertical datum) in a 6 ft x 6 ft grid.

The 2011 ALSM dataset was commissioned by the local Whatcom County Public Works department and collected around January 1, 2011. A local company, using a Riegl VQ-480 system, covered 10 square miles around the Swift Creek landslide using a very dense spatial sampling. The average point spacing of the dataset is 5.09 points per m^2. To verify the accuracy of the data, an independent surveying firm identified 14 ground-control points within the project area. When compared to the LiDAR data, the RMSE of the control points was 4.9 cm, with an absolute accuracy at the two-sigma level (1.96 x RMSE) of 9.6 cm.

The bare earth data were provided in ESRI GRID format, with a cell size of 2 feet. The data were provided in Washington State Plane North projection (U.S Survey Feet, NAD83 horizontal datum, NAVD88 vertical datum).

4.2. Quantifying surface displacement

4.2.1. Measuring displacement using ICP

After aligning and georeferencing the five terrestrial LiDAR datasets, 25 boulders were identified and isolated in the multi-temporal point clouds. Each boulder was imaged by approximately 1,000 points or more. Nine of the boulders were not readily identifiable in the earliest (October, 2009) survey. A time-series was established for each boulder: October

2009–May 2010, May–October 2010, October 2010–January 2011, and January 2011-April 2011 (Figure 14). For each pairing, the earlier dataset was considered the "reference" and the later dataset was aligned to it using the ICP application following an initial rough manual alignment. The information describing the transformation of the boulders from "before" to "after" was captured in the 4x4 transformation matrix associated with each dataset. Because individual point cloud features were isolated, this shift in the alignment matrices accurately represents the displacement of each feature and not a transformation of the entire point cloud.

After the alignment of each feature to its reference, a point to surface comparison was completed on the aligned features. In the Polyworks environment, a mesh "surface" is interpolated from the point cloud data based on the step spacing and maximum edge length (See Appendix). Results of the change analysis indicate the alignment process resulted in mean point to surface (shortest distance) deviation values ranging from 0.5 mm to – 3.7 mm, with an average of -0.2 mm. Standard deviation values, which are considered a better estimation of uncertainty, ranged from 1.6 cm to 13 cm with an average of 4.9 cm.

Boulder velocities were determined by dividing the net displacements by the number of days between surveys, yielding what I refer to as an average daily velocity. Although this rate is too simplistic to accurately describe changes in the movement rates over day-to-day time scales, it will provide a basis to discuss the overall changes in seasonal movement rates on the toe.

4.2.2. Image Cross-Correlation via PIV

PIV was applied to greyscale slope gradient images derived from the gridded DEMs (Figure 15). Processing of the DEM images included slope analysis using Spatial Analysis tools in ArcGIS, resulting in raster datasets with slope values ranging from 0 in flat areas to 90 degrees on vertical slopes. The greyscale slope gradient images were compared using the program 'PIVlab', an open-source extension in MATLAB following a similar approach used in Aryal et al. (2012). This approach uses congruent DEMs to create greyscale slope gradient image pairs. In order to maximize the effectiveness of PIV, a smoothing function was applied to the datasets to minimize the differences in texture between the multi-temporal datasets. This was accomplished via a low-pass filter in the ArcGIS environment by calculating mean values within a 4x4 cell to reduce the extreme values within each dataset.

The PIVlab program applies a direct cross-correlation algorithm to find correspondence between the two images. The algorithm is computationally complex; it incorporates signal processing of the phase shifts via Fast Fourier Transform (FFT) and applies a Gaussian fit function to find the correlation peak. A complete description of the mathematics involved can be found in Raffel et al. (2007).

The PIV application I used is based on two primary variables, the interrogation area and the step spacing (i.e., resolution). The interrogation area represents the extent to which the application will search for the corresponding pixel values and therefore must be greater than the maximum expected displacement. The PIVlab program incorporates an iterative multi-step process with decreasing interrogation areas and increasing resolution. The initial run produces an imprecise but relatively smooth displacement field; subsequent runs deform the

images based on the initial results to refine the process and improve the correlation peak. In my analysis, an initial interrogation area of 60 pixels was chosen in order to accommodate the maximum expected displacements. I chose a step size of 12 to take advantage of the high-resolution LiDAR data.

4.3. Elevation change analysis

4.3.1. Digital-elevation models

To facilitate the interpretation and analysis of changes in surface topography, DEMs were created from all of the LiDAR datasets ArcGIS 10.2. Although working directly with the raw point data provides the highest accuracy, comparing large volumes of point data is often plagued by insufficient computer memory issues. An accepted alternative is to create an interpolated surface using GIS software (e.g., Corsini, 2009; Buckley, 2008; Prokop, 2009). DEMs were created from each TLS dataset with a cell size of 0.1 meters based on the high resolution of the surveys (spot spacing was generally below 75 mm). The natural neighbor function was used to interpolate the 3D point-cloud data into raster format (e.g., Prokop, 2008).

4.3.2. DEM differencing

A commonly used method to identify changes in elevation is to subtract an older DEM from a more recent DEM (Corsini et al., 2009; Daehne and Corsini, 2012; Kasperski et al., 2010). To investigate topographic elevation change, I completed a DEM of difference using the TLS datasets. In order to differentiate areas of depletion from areas of accumulation, I chose a

detection threshold of +/- 15 cm for the TLS datasets, based on the cumulative errors associated with the datasets (described below). The actual range of detection is considerably less than the thresholds chosen.

In the case of the airborne LiDAR datasets, the uncertainties for each dataset (30 cm for the 2006 dataset and 9.6 cm for the 2011 dataset) were propagated through the analysis. Using a standard formula for error propagation (Equation 6), the cumulative uncertainty (σ_z) with the DEM differencing method using the airborne LiDAR datasets is 31.5 cm.

$$\sigma_z = \sqrt{(\sigma_x)^2 + (\sigma_y)^2} \quad [6]$$

Vertical alignment was examined by identifying two unaltered road surfaces in open areas close to the landslide and comparing the 2006 LiDAR point elevations with the 2011 DEM (Figure 3). A total of nearly 4,000 points from the two sections of road were selected and the points were compared to the 2011 DEM using the Extract Values to Points tool in Spatial Analyst (ArcGIS 10.2). The difference between the observed and expected outcomes were averaged as a whole, and the 2006 LiDAR dataset was 3.3 cm lower than the 2011 DEM (Table 4). Therefore, the 2011 DEM was lowered by that amount. Using the 2006 dataset as the reference was not ideal since the data quality is poorer than the 2011 dataset; however, the 2011 dataset was provided in raster format and therefore a point comparison would have introduced additional interpolation error.

The uncertainty involved with the DEM differencing of TLS datasets was low. In this study, I used artificial targets to roughly align the multi-temporal datasets, followed by ICP matching of thousands of points from stable tree trunks located adjacent to the slide.

Cumulative errors in the acquisition of the data, the alignment of contemporaneous scans and the subsequent alignment of the assembled point clouds, resulted in standard deviation values of between 6 mm and 10 mm for the TLS datasets. Using a standard formula for error propagation (Equation 6), the cumulative uncertainty (σ_z) with the DEM differencing method resulted in a net uncertainty of less than about 13 mm.

4.3.3. TLS volumetric change estimates

The volumetric calculation of mobilized landslide material was carried out in ArcGIS 10.2 using the DEMs. Volumetric change estimates were calculated using a cut and fill approach based on the elevation differences (e.g., Bremer and Sass, 2012). As noted by Dewitte and Demoulin (2005) and Daehne and Corsini (2012), such volumetric calculations do not represent the actual volume of displaced material, but rather provide an estimation of the volume of uplifted or collapsed terrain.

Small differences in the vertical alignment of disparate datasets can result in significant errors during change analysis, especially when dealing with a large surface area. Based on the wide distribution of trees and the independent verification of the stable boulder, the vertical bias between the datasets should be minimal with cumulative errors of less than 13mm (discussed in section 4.2.1). Using the January – April, 2011 TLS DEM of difference as an example, a broad change in surface elevation of +/- 13 mm would result in a net change of about 600 m^3. Considering the total estimated gain of 14,400 m^3 during the time frame, this amount is considered to be negligible.

5. RESULTS

In this section, I present the results of topographical and volumetric change analysis using DEMs and surface displacement analysis on large boulders using pointcloud matching software. Results from elevation and surface displacement analysis confirm that the Swift Creek landslide underwent significant deformation during this study.

5.1. Surface Displacement

5.1.1. Iterative closest point analysis of terrestrial LiDAR data

The results of ICP analysis of 25 boulders on the toe of the landslide are presented in Figure 16. The boulders were displaced to the NW and roughly clustered into two groups based on their average daily velocities (one group, group A, was faster than 4 cm/day and the other, group B, was slower than 2 cm/day). Cumulative displacement vectors derived from TLS data are shown in Figure 17. The disparity in movement between the conglomerate unit in the northeastern section of the toe and the rest of the boulders is apparent. Of the 25 boulders identified for this study, eight could not be positively identified in the first dataset established in October 2009. Total horizontal displacement of the 17 boulders over the 18 months ranged from 3.3 – 39.3 meters. Considering the average standard deviation value of about 5 cm for each point cloud, these values are well within the detectable limit of movement achieved using this method.

Average velocity rates of the 25 boulders varied across the landslide from a low of 0.6 cm/day to a high of 9.4 cm/day. This represents a wide range of motion, with some boulders

moving 15x faster than others. Over the course of a year, these rates work out to a range of 2.2 – 34.3 m/yr.

The movement rates of the boulders varied over the course of the study. The maximum velocity during the study was observed in boulder 021, which reached 12.1 cm/day during May to October, 2010. During the four intervals of the TLS investigation, the average daily velocities for the two groups ranged from 0.75 – 1.2 cm/day for the slow group (group B) and 4.0 – 5.8 cm/day for the faster group A (Figure 17). The slowest intervals for both groups occurred between the October, 2010 to January, 2011 time-series, with the average group velocities about 20-25% lower than the average over the eighteen months of the study.

During the other three intervals, average velocities within the two groups were less variable than the slow period discussed above. Average group A velocities ranged from a low of 5.27 cm/day (May – October, 2010) to a high of 5.84 cm/day (October, 2009 – May, 2010). Average group B velocities ranged from a low of 0.98 cm/day (May – October, 2010) to a high of 1.19 cm/day (January – April, 2011). The average group velocity over the entire eighteen month study was 5.1 cm/day for group A and 1.0 cm/day for group B. Therefore the average group velocities increased by 12% (over the eighteen month average) for group A and 16% for group B.

Out of the 17 boulders identified in the October, 2009 to May, 2010 survey, all but two experienced a decrease in average daily velocity during the subsequent May to October, 2010 period. The average daily velocities in group A slowed by 0.57 cm/day, while group B experienced an average decrease of 0.16 cm/day. The trend continued between October, 2010 and January, 2011 when 23 out of the 25 boulders experienced a decrease in average daily

velocity. Group A slowed, on average, 1.58 cm/day while group B slowed by 0.21 cm/day. The velocity of all 30 boulders increased during the final interval, covering January to April, 2011.

The two clusters of boulders followed the same velocity trend of decreasing velocities beginning around May, 2010 and continuing until sometime in the following winter; however, the relative changes in velocity were quite different. The boulders experiencing the greatest rates of movement also saw the largest changes from interval to interval. For example, the faster group slowed down an average of 1.6 cm/day during the 3rd time-series, whereas the slower cluster only saw its velocity change by 0.2 cm/day. During the following interval, the faster group increased in velocity by 1.5 cm/day; the slower group only gained 0.5 cm/day.

5.1.2. Image cross-correlation using airborne LiDAR data

In general, PIV was able to resolve displacement across the landslide, with the exception of highly deformed areas on the toe (Figure 19). Since PIV requires slope-scale features to retain their geomorphic shape, highly deformed terrains are unlikely to be preserved enough for correlation (Daehne and Corsini, 2012). The flowing nature of sections of the toe at Swift Creek made PIV unsuitable for measuring surface displacement over such a long time period using airborne LiDAR (Figure 19). However, the body and most of the toe were not highly deformed during the study and provide suitable terrain for PIV analysis.

In velocity field calculations it is not uncommon for the PIV analysis to contain some vectors that are invalid (e.g., Daehne and Corsini, 2012). In order to remove erroneous vectors from

the airborne LiDAR PIV analysis (Figure 19), a two-step vector validation process was completed. Evidence for flawed vectors included large displacement values in stable areas and vectors in the wrong direction over the landslide. A significant number of the erroneous vectors were located on the toe (Figure 19). In the first validation step, an area-wide filter was applied to the vectors to remove those with velocities larger than a threshold of five times the standard deviation of the velocity field. Visual inspection showed that the global filter removed most of the erroneous data, while retaining a large number of vectors. The second step, a manual removal of vectors, was applied sparingly and only in cases where the vectors were undeniable inaccurate.

In order to verify the effectiveness of PIV analysis using airborne LiDAR, an analysis was completed using the stable terrain around the landslide (Figure 20). Out of 3,105 displacement vectors, 49 vectors were deemed incorrect based upon displacement values greater than two pixels (3.6 m). Of the remaining vectors, average displacement was 0.01 pixels along the x-axis and 0.15 pixels along the y-axis. The standard deviation values were +/- 0.5 pixels or 0.9 meters.

The large number of erroneous vectors in the highly deformed parts of the toe precluded manually removing them. Instead, I opted to employ automated filtering based on standard deviations and local median filters resulting in the retention of many erroneous vectors. After the filtering process, an automated interpolation was applied to the missing data points using a nearest neighbor technique. In order to avoid excessive interpolation, every effort was made to retain the original vectors. Ninety-five percent of vectors over the main body of the landslide were retained (Figure 19).

Despite overall movement to the northwest, surface displacement is variable across the body of the landslide; the rates vary both down gradient and perpendicular to the flow direction (Figure 21-24). The average net displacement across the body of the landslide was 7.8 pixels (1 pixel = 1.8 meters) or 14.0 meters over the 5 year period between airborne LiDAR surveys, working out to an annual displacement rate of 3.0 meters per year (Figure 24). The upper reaches of the landslide (near the head) are moving faster than the rest of the body, with net displacements as high as 19 meters (10.6 pixels) over the 5 year period or 4.1 meters per year (Figure 18). These results are similar, albeit a bit slower than previous GPS surveys that showed the main mass moving around 4 – 5 meters per year (Linneman and Pittman, 2009).

Results of PIV analysis on the toe using TLS data are presented in Figures 26 – 29. The toe of the Swift Creek landside is a highly dynamic zone. While ICP results provided evidence for two kinematic zones, PIV analysis reveals at least three or more discrete zones on the toe. Movement is slowest along the northern boundary of the toe (e.g., the Huntingdon blocks), with velocities that ranged between 5 – 8 mm/day. This rate is slightly slower than the velocity of the main body of the earth flow, which PIV estimated at 8.2 mm/day. This slow zone is separated from the faster moving material by a sharp boundary that is oriented NW-SE. The slow zone on the north side of the boundary gradually increases in velocity upslope. The upper reaches of this area recorded a large degree of variability between survey intervals. Minimum velocities were recorded during the October 2010 – January 2011 period (Figure 27), followed by maximum velocities during the subsequent January – April, 2011 period (Figure 28). Average velocities in this zone ranged from 1.5 – 2.7 cm/day.

The material on the southern portion of the toe exhibits greater surface displacement than the Huntingdon blocks and appears to experience greater temporal variability as well, although not as much as the upper reaches of the toe in the NE portion. Observed velocities ranged between 4.0 – 5.3 cm/day, with minimum displacements occurring in October, 2010 – January, 2011 (Figure 27), followed by the maximum rate between January to April, 2011 (Figure 28).

The fastest area on the landslide is in the central portion of the toe (Figure 28). Displacement rates on the advancing lobe of material at the front of the flow were slowest in this area during the October, 2010 – January, 2011 period (Figure 27), with average velocities of 4.2 cm/day. Velocities increased in the subsequent period and reached a maximum velocity of 5.7 cm/day during the January – April, 2011 time period (Figure 28).

To verify the measured displacement rates on the toe using ICP, I estimated the errors associated with PIV analysis of TLS data by comparing them to the displacement values obtained via ICP analysis. Seven of the 25 boulders used in ICP analysis were selected based on their wide spatial distribution. The approximate position of the boulders was identified in the PIV images and the relevant vector for each boulder was analyzed. In total, 24 features were compared. Comparing the measured values in ICP with the results of PIV revealed a mean error of around 0.3 meters and an average standard deviation of 0.50 meters (Table 6).

5.2. Changes in elevation

Five DEMs were used to detect and measure changes in the topography at the site. A first differential DEM was created by subtraction of the 2006 and 2011 DEMs (Figure 29).

Results from the comparison provide evidence of significant changes in elevation across the landslide. In order to avoid confusion, increases in elevation will be referred to as accumulation or "gains", while decreases in elevation will be referred to as depletions or "losses". The use of these terms is not meant to imply the origin or nature of the transport mechanisms (i.e., accumulation does not necessarily indicate deposition).

Overall, depletion was found to have occurred over a broad area of the main mass, with some regions experiencing more than 10 meters of elevation loss (Figure 39). Typical losses of 2 – 4 meters were common across most of the upper slide. There is evidence of fluvial erosion in the lower reaches of the toe, where a lobe-shaped zone of depletion can be seen in an area that contains a deep gulley.

The primary accumulation zone is located on the toe of the landslide, an area that has experienced the greatest change in elevation over the five year time span. Along the margins of the advancing toe, more than 10 meters of material has been gained in three distinct zones. A second accumulation area appears in the upper reaches of the landslide, below the crown of the slide.

Multi-temporal analysis of TLS surface elevation data was carried out using five DEMs providing coverage from October 2009 to April 2011. All of the change diagrams record some degree of deformation on the landslide. The results of the change analysis are presented in Figures 31-32.

Changes in elevation around the toe of the Swift Creek landslide between October 11, 2009 and May 5, 2010 (206 days) are presented in Figure 32. Analysis reveals a complex

kinematic environment with significant displacement (up to 5 m) of material along a narrow lobe at the front of the toe. Immediately upstream of the lobe, there is strong evidence for intense stream downcutting (as much as 4 meters) based on the sinuosity of the disparity and the location of the stream. Losses within the stream channel is not uniform, but it does appear to be concentrated in the lower half of the toe and is greatest along the southern lateral margin where it joins another small tributary of Swift Creek.

Increases in elevation occurred across most of the toe between May 5, 2010 and October 4, 2010 (152 days) (Figure 33). In comparison to the previous time-series, there is significantly less variability in the movement patterns. A substantial amount of material (up to 4 meters) accumulated along the leading front lobe of the toe. The period between October 4, 2010 and January 19, 2011 (107 days) can be characterized as having fairly extensive depletion across the toe (Figure 34), similar to the previous winter (October 2009 to May, 2010). A significant loss of material is evident along the lateral margin and in the middle of the toe. Pockets of accumulated material were found across the toe and along the front margin, although the gains were fairly small, generally less than 2 m. The final interval covered in this study, January 19, 2011 and April 20, 2011 (91 days) is somewhat difficult to characterize (Figure 35). Areas of accumulation and depletion are spread out across the toe, with neither dominating. It does appear that the central portion of the toe experienced a greater degree of change than the rest of the toe.

In order to better compare the seasonal changes in elevation around the toe, a comparison between the October 4, 2010 and April 20, 2011 (198 days) datasets was completed (Figure 36). This period is quite similar, in both duration and in terms of seasons, to the first interval,

October, 2009 – May, 2010 and is therefore useful for a year to year comparison. The results show that in both intervals, modest accumulation occurred along the northern portion of the toe, while significant areas of depletion were found along the southern portion. Over the eighteen month period, from the first survey on October 9, 2009 to the final survey on April 20, 2011, a significant amount of material was removed and deposited on the toe (Figure 37). The front of the toe experienced the largest increase in elevation during this period

5.3. Mobilized Volumes

Volumetric change analyses show dynamic conditions on the toe of the landslide over short time spans (Figure 38). Ranging from a maximum net depletion on the toe of nearly 25,000 m^3 during the rainy season (October 2010-January 2011) to a maximum net accumulation of approximately 29,000 m^3 during the dry season (May -October, 2010), there is significant variability between terrestrial LiDAR campaigns. There is a seasonal pattern with a net loss of material during the rainy months and a net gain during the dry months (Figure 39**)**. The loss of 25,000 m^3 of material during the rainy season yields an erosion rate on the toe of 60 cm per square meter. For the water year 2009 (October, 2009 to October, 2010), 14,000 m^3 of material was added to the toe. This confirms field observations of a toe that is growing in area and thickness.

6. DISCUSSION

In this section, I evaluate the applicability of using terrestrial LiDAR to study actively deforming earth flows, and also discuss the implications of interpreting landslide movement using derived surface displacement measurements and how the observed patterns relate to overall earth flow dynamics and morphology.

6.1. Effectiveness of using TLS for studying earth flows

Despite some initial difficulty in finding suitable scan locations (due to the thick vegetation), my study has shown that TLS can acquire precise surface-displacement data and is useful in monitoring earth flows. With positional uncertainties less than about 10 mm, this method could be applied to a variety of geologic situations that could benefit from remote geodetic monitoring (e.g., measuring glacial flow or measuring surface change on volcanoes).

Quantifying displacement using terrestrial LiDAR and pixel cross-correlation was less precise than the ICP measurement technique; however, this alternative approach permitted us to obtain displacement data over a much broader area and precision was still acceptable (+/- 0.5 meters).

6.2. Spatial and Temporal Variations

PIV analysis revealed the bulk of the landslide is moving rather coherently, at long-term rates estimated to be about 3.0 (+/- 0.9) meters/year during the period between 2006 and 2011. In contrast, the toe of the landslide is a much more dynamic zone with fast moving zones

exceeding 25 meters per year adjacent to areas with velocities of only 2-3 meters/year. Using ground-based LiDAR, I was able to document significant changes in the temporal movement rates on the toe.

The spatial variability of surface velocity determined by LiDAR point cloud analysis revealed distinct zones of activity on the toe. An overall examination of the surface velocity rates of individual boulders identified two separate clusters (Figure 16). The slower group had average daily velocities below about 2 cm/day, while the faster group has velocities that generally ranged between 4–6 cm/day. The slower cluster represents a fragmented conglomeratic block along the northern margin of the toe that is courser than the surrounding material (Figure 17). This discrepancy in velocity could be due to a number of factors, including material differences (e.g., porosity, strength, rheology), groundwater and surface flow or channeling of the flow down the valley (as opposed to the margins) due to constriction of the valley walls. I investigated the precipitation patterns during this time to better understand the

To better understand the relationship between precipitation and movement patterns, I have included a discussion on the precipitation patterns during my study. There is no weather monitoring in the study area. A weather station (Clearbrook) located 9.4 km away (Figure 2) was used to as a source of precipitation data. Although in close proximity, the stations differ in elevation (< 200 m), leading to enhanced precipitation due to orographic lift. Nevertheless, this weather station should provide a good proxy to the seasonal weather patterns at the site.

The weather during this study was wetter than normal (Figure 40). Beginning around the start of this project in October 2009, the cumulative precipitation (beginning October 1st) was

above normal throughout the entire water year 2009 and most of 2010 (Figure 40). The cumulative monthly precipitation for the 2009 water year ended about 25% above normal. Through the first five months of the 2010 water year was about 35% above normal.

The seasonal precipitation patterns during my study are similar to the "normal" precipitation pattern of wet winters and drier summers (Figure 2). The October 2010 to January 2011 interval experienced the highest cumulative rainfall recorded during the intervals covered in my study (Table 2). During the 107 days between surveys (from October 4, 2010 to January 19, 2011) more than 66.6 cm of rain was recorded. The driest interval in my study was the late spring to early fall period represented by the May to October, 2010 survey interval, when 39.4cm of rain fell. This period is associated with decreasing velocities across the toe (Table 5).

The lag time between the onset of rainfall and landslide movement at the Swift Creek landslide is likely to be on the order of several months (Figure 41). A lag time of this magnitude would seem to support the deep failure plane proposed by McKenzie-Johnson (2004). By comparison the Slumgullion landslide in Colorado, a similar large, slow-moving earth flow with an estimate toe thickness of 12 – 30 m, responds to rainfall in several weeks or less (Coe et al., 2003).

It is difficult to obtain a precise response time given the long time intervals between surveys used in this study (between 90 and 206 days). My data shows that in 2009, during the months of October to December, the average velocity was at its fastest; yet, in 2010, the minimum velocities were recorded during this same period. It seems likely that the longer survey interval missed a significant increase in velocity that was evident in the October, 2010 to

April, 2011 intervals. Increasing the surveying frequency would help to refine the response time to increased precipitation at the site. Nevertheless, one approach to analyze the lag time of deep-seated landslides is to look at the antecedent rainfall amounts over longer time periods. The cumulative monthly precipitation amounts for 2, 4, 6, 9 and 11 months prior to each month are shown in Figures 43-47. Wetter than normal conditions are evident throughout this study.

Based on similar year-to-year seasonal variability in precipitation, I expect the movement patterns at the landslide to follow similar patterns. The cumulative precipitation, over the last few months of my study were especially wet (Figure 43). The velocities of the individual boulders during this period did not increase proportional to the increased precipitation indicating that the response time exceeded the final survey interval.

It appears that the peak average velocities occurred in late-winter to early spring (January to May) and lagged behind peak precipitation by a few months (Figure 41). Based on the delay between peak velocity and peak cumulative precipitation, I suspect the response time to increased precipitation is somewhere between six (Figure 44) and nine months (Figure 45).

The lag between decreasing precipitation and minimum velocities are also delayed by a few months (Figure 41). Considering the precipitation leading up to and during the October, 2010 to January, 2011 interval was near "normal" (Figure 41), I suspect that this period is typically a time of minimum velocities despite the increasingly wet environment. Based on the typical dry period in June-September, it seems likely that it takes around six months for the landslide to dry out and slow down (Figure 45).

By comparing the recorded velocities with the broad precipitation patterns, I was able to document temporal variations in velocity and show that there is a lag between increased precipitation and velocity; however, the magnitude of the lag is less clear because of the long survey intervals used in my study.

6.3. Analyzing elevation changes in the landscape

LiDAR analysis revealed the landscape around the toe of the Swift Creek landslide changed in many ways during this study. With no organic topsoil or vegetation, sediments on the toe are highly susceptible to erosion and easily mobilized by surface water during heavy precipitation events. Because of the widely spaced timing of the surveys, the forward movement of the landslide toe obscures the volumetric losses related to erosion. Each survey represents a single snapshot in time, and each comparison represents the cumulative effects of multiple and competing mass-wasting processes. Given the length of time between surveys, between 90 and 206 days, significant deformation occurred. Although I was unable to describe the short-term (daily to monthly) changes at the site due to the timespan between surveys, the same methods would be able to detect changes with more frequent surveying (detection threshold of 4.9 cm). Shorter surveying intervals would also minimize the advancement of the translating mass of the slide and therefore more accurately capture the volume of displaced material.

The results of ICP analysis of the TLS boulders revealed that all of the 25 boulders experienced a decrease in elevation during each scanning interval. Yet, based on the elevation-differencing analysis, it is clear that many of the boulders were in regions that experienced net increases in elevation (Figure 33). A likely explanation is that the toe is showing an apparent increase in thickness as it advances downslope due to translation of the mass. For this reason, areas that show an increase in elevation do not necessarily represent depositional areas, but rather an advancing surface. I interpret that most of the apparent increases in elevation across the toe of the landslide (excluding the accumulation zones along the leading margins) can be attributed to advancement of the landslide (Figure 48).

The advancing toe, the downslope flow of surface sediments and material, along processes such as shallow slab sliding, debris flows or large down-cutting erosional events have created a landscape that is very complex. Over longer time-spans, the toe is an area that is increasing in size and thickness; however, the fine-grained, weak sediments on the toe are subject to increased erosion and mass wasting processes during periods of high-precipitation. In this manner the toe acts as a source zone for rubble and debris that reach the creek. Differencing of the DEMs produced by TLS resulted in the loss of 25,000 m^3 of material on the toe during the rainiest period in the study, from October 2010 to January 2011 (Figure 38). During times of heavy rainfall and high antecedent ground moisture, when the sediments on the surface of the landslide are saturated and at their weakest, is likely to be a time of high water flow in the creek. One can imagine this scenario leading to a significant removal of material from the landslide since higher flows would transport more material away from the toe. The transport of material is enhanced by slope failures associated with the down-cutting or widening of

channel morphology. Depending on the timing of the slope failures (during the storm or after), the sediments may be transported away from the landslide or be stored in the channels.

The wet period also coincides with the lowest measured surface velocities on the toe, likely because of the preceding dry conditions as discussed above. During these periods of heavy runoff and net depletion, the landslide is likely not moving forward (via translation) quickly enough to compensate for the losses due to mass-wasting and erosion. During the subsequent January to April time period, precipitation decreased yet the toe showed significant increases in velocity and a net volume gain. I interpret this to be the result of both an increase in the velocity of the flow and a decrease in erosional events removing material from the toe leading to a net gain of material.

In addition to the movement of the landslide (and all the mass wasting processes associated with it), Swift Creek and its upper tributaries have an influence on the landslide. At the sides and front of the toe, where the streams have substantial erosive potential during high flow, there is no evidence for an increase in the elevation of the streambed (Figure 49). Over the next several years, as the toe fills the narrow canyon with larger material (due to the proximity of the toe), it will be interesting to see whether the stream has enough power to maintain its current level at the base of the landslide, as it has for the past several years (Figure 49).

6.4. Implications for earth flow mechanics

Examination of surface displacement rates and mass movement processes can help identify the mechanisms that drive the transition from earth slides to earth flows and help characterize

the underlying factors controlling earth flow kinematics (Daehne and Corsini, 2012). In the case of the Swift Creek landslide, the consistent movement of the surface indicated by my study supports previous interpretations (e.g., McKenzie-Johnson, 2004) that the earth flow is driven predominantly by sliding along a basal surface (Figure 22). This interpretation is also consistent with the findings of Savage and Baum (2005), who concluded that the majority of slow-moving landslides move primarily by sliding along basal and lateral shear surfaces with lower internal deformation. The highly variable rates on the toe, coupled with field observations of nearly saturated surface material during the late fall to mid-spring timeframe, supports the characterization that the Swift Creek landslide transitions from a sliding mass to a flow (Figure 50). Based on the high velocities seen in the upper reaches of the toe, I conclude that this transition occurs in the toe or slightly above it (Figure 51). The increase in velocity above the toe (Figure 21) could be a transitional area; however, annual movement rates in the fastest zone on the upper toe are nearly six times faster than the fastest rates observed on the forested terrain above the toe. Therefore, I conclude that the flowing sediments on the surface of the toe of the Swift Creek landslide primarily involve only the top few meters of material, which overlay a predominantly sliding mass. I base this on the movement of individual boulders showing downward displacements while the surrounding surface experiences inflation.

7. CONCLUSIONS

I was successful in applying a newly adapted method to quantify 2D surface displacement and analyze the behavior of a single landslide using terrestrial LiDAR data. I used both terrestrial and airborne LiDAR data to create successive DEMs for qualitative and quantitative descriptions of the mass transfer of material to describe the short and mid-term kinematics of an active earth flow, the Swift Creek landslide in Washington State. The DEMs were used to estimate the volumetric transfer of material on the landslide and to quantify surface displacement over the forested body of the slide.

My study successfully applied a cross-correlation function via a PIV application using airborne LiDAR on the forested body of the landslide and over the toe of the earth flow using TLS data. The success of the PIV method depended on the presence of relatively undeformed geomorphologic surfaces on the landslide. These slope-scale features were retained well on the body of the landslide over the 5 years between airborne LiDAR surveys. Estimated deformation rates over most of the main body were 3.0 (+/- 0.9) m/yr. Rates increased near the head indicative of active retrogression into older slide deposits.

On the rapidly changing toe, PIV was successfully applied to multi-temporal TLS data when surveys were separated by less than about 5 months. The quality of the PIV results over the toe illustrate the limitations to PIV on highly deformed terrain. Over shorter time intervals, the PIV produce a nearly continuous displacement field. The results revealed significant spatial and temporal variability on portions of the toe. The presence of a sharp boundary between slower moving material and the fastest zone of flow was a significant finding in this study.

Cumulative displacement measured via ICP analysis varied dramatically at the site, from 3.3 m to 39.3 m over the 18 months of the study. When features were repeatedly identified in multi-temporal scans, the limit of detection using assembled point clouds and the ICP application was about 10 mm, which is a lower threshold for change was achieved using PIV. The results show that terrestrial LiDAR is well suited to study actively deforming landscapes. Future advances in the automated removal of vegetation and data processing would potentially make this method suitable for rapid analysis of hazardous geologic phenomena.

Elevation change analysis revealed important seasonal characteristics about the volumetric transfer of material on the earth flow. Extensive depletion over a large portion of the main body and a toe that experiences significant accumulation and depletion based on the time of year were the main findings of the analysis.

8. TABLES

GPS Benchmark Position	Transformed UTM Position	
-122 14 59.7819	554959.5742	
48 54 36.9711	5417752.078	
299.749	299.749	(NAD 83)

	Target 1	Target 2	Target 3
Easting	-34.044	-54.394	-80.804
Northing	-43.028	-16.638	70.372
Elevation	18.541	2.041	-15.619
	554925.53	554905.18	554878.77
Final Target Coordinates (UTM)	5417709.05	5417735.44	5417822.45
	318.29	301.79	284.13

Table 1 - Summary of GPS benchmark position and total station data obtained using GPS and total station.

Surveys	Days between scans	Cumulative Rainfall (cm)
10/4/2009 - 05/05/2010	206	103.89
05/06/2010 - 10/04/2010	152	39.40
10/05/2010 - 01/19/2011	107	66.60
1/20/2011 - 04/20/2011	91	42.11

Table 2 - Using data collected at the Clearbrook weather station, located 10km Northwest of the landslide, the cumulative rainfall during each of the four intervals was calculated and the average was found by dividing by the number of days between scans.

	# of points	Mean (mm)	Std Dev (mm)	Points within 2*Std Dev
October, 2009	35347	0.29	9.39	98.80%
October, 2010	23563	0.42	6.48	97.03%
January, 2011	36388	-0.08	9.11	97.41%
April, 2011	31292	-0.29	6.02	95.19%

Table 3 - In order to verify the alignment of the assembled point clouds, a large, stable boulder was omitted from the alignment procedure. After aligning the multi-temporal datasets, a change analysis was completed on the boulder via a point to point comparison in Polyworks. The May, 2010 dataset was used as the reference point cloud and other datasets were compared to it. The results show the uncertainty with the alignment process is relatively low, less than about 10 mm.

2011 - 2006 DEM comparison	# points	Mean ΔZ (m)	RMSE (m)
Road A	2293	-0.019	0.33
Road B	1567	-0.053	0.16
		-0.033	0.27

Table 4 - Two sections of road, located near the landslide and included in both airborne LiDAR surveys (from 2006 and 2011), were used as stable control points to look for discrepancies in the vertical alignment of the two datasets. The point data for the roads in the 2006 dataset were isolated and then subtracted from the 2011 DEM raster. The differences were then averaged and the result was the 2006 dataset was, on average, 3.3 cm lower than the 2011 dataset.

Average daily velocity – cm/day
(Net displacement ÷ # of days per survey interval)

	Group A	Group B
October 4, 2009 - May 5, 2010	5.84	1.14
May 6, 2010- October 4, 2010	5.27	0.98
October 5, 2010 – January 19, 2011	4.01	0.75
January 20, 2011 – April 20, 2011	5.29	1.19

Table 5 - Velocity analysis from the 25 boulders on the toe revealed two clusters of data. Average daily velocities for each group were calculated and are presented above. A subjective velocity of 3 cm per day was selected as the cutoff between the two groups. It should be noted that the fastest average velocity recorded in group B was 2.1 cm/day while the slowest average velocity for group A was 3.7 cm/day.

Boulder		October 2009 - May 2010	May 2010 - October 2010	October 2010 - January 2011	January 2011 - April 2011
8	ICP	2.70	1.46	1.28	1.58
	PIV	2.98	1.52	1.54	1.71
		0.28	0.06	0.26	0.13
4	ICP	13.29	8.20	4.45	5.12
	PIV	X	7.80	4.50	5.05
		-	0.40	0.05	0.07
12	ICP	1.77	1.35	0.29	0.67
	PIV	1.79	1.35	0.42	0.69
		0.02	0.00	0.13	0.02
15	ICP	12.01	8.23	4.60	5.28
	PIV	X	8.03	4.52	5.02
		-	0.20	0.08	0.26
19	ICP	X	2.69	1.84	2.59
	PIV	4.12	2.90	2.00	2.80
		-	0.21	0.16	0.21
24	ICP	9.45	6.67	3.32	3.49
	PIV	X	8.46	4.82	5.27
		-	1.79	1.50	1.78
25	ICP	1.65	1.01	0.43	0.59
	PIV	1.64	0.94	0.53	0.56
		0.01	0.07	0.10	0.03
				Average	.33 m
				Standard Deviation	.50 m

Table 6 - Comparison of displacement rates obtained via ICP and PIV analysis at specific locations across the toe of the Swift Creek landslide.

9. FIGURES

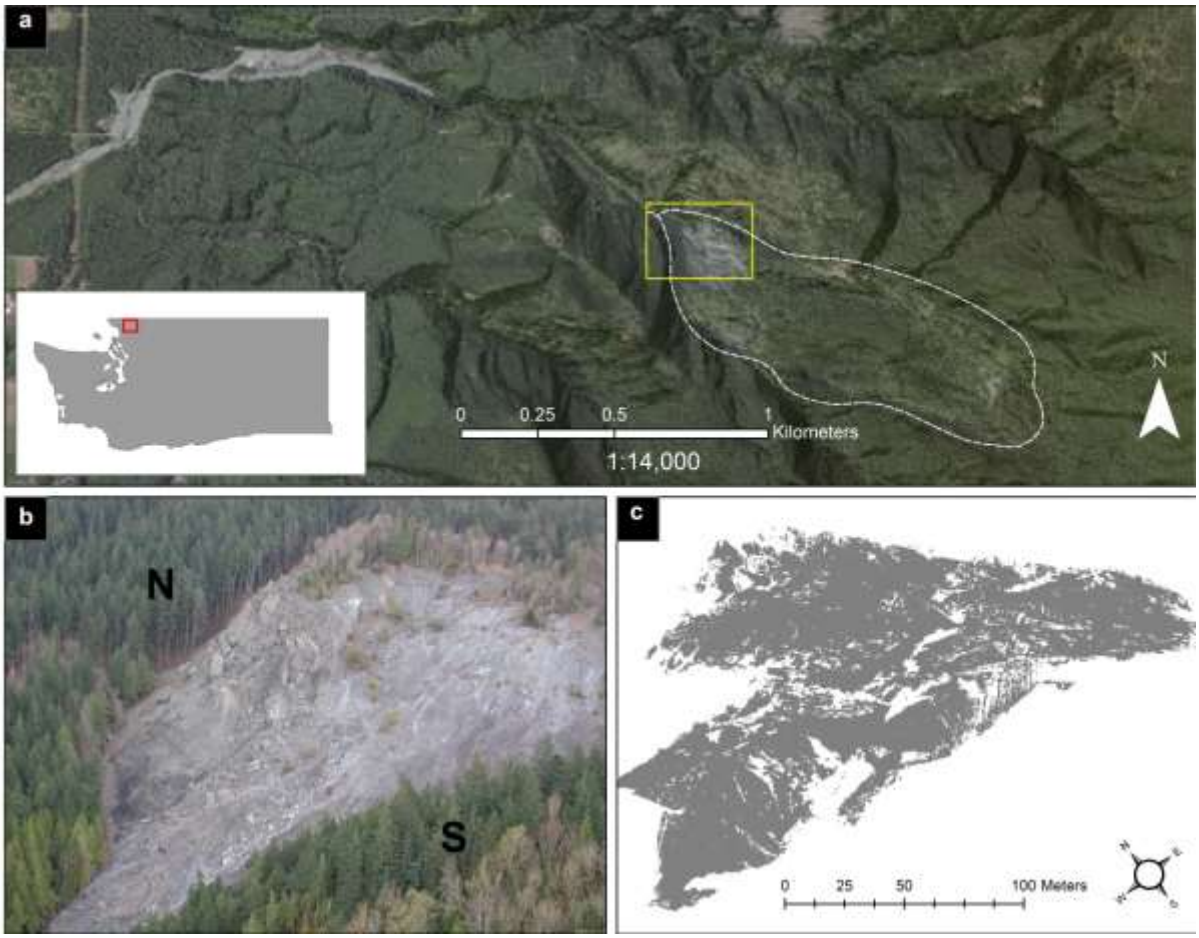

Figure 1 - An overview of the study area. (a) Satellite-Imagery (Google Earth, 2013) draped on a hill-shade showing the Swift Creek basin. The active landslide is presented in dashed white and the unvegetated toe is featured in the yellow region. (b) Aerial view of the unvegetated toe (from 2003), and (c) typical point cloud coverage of the toe acquired with terrestrial LiDAR.

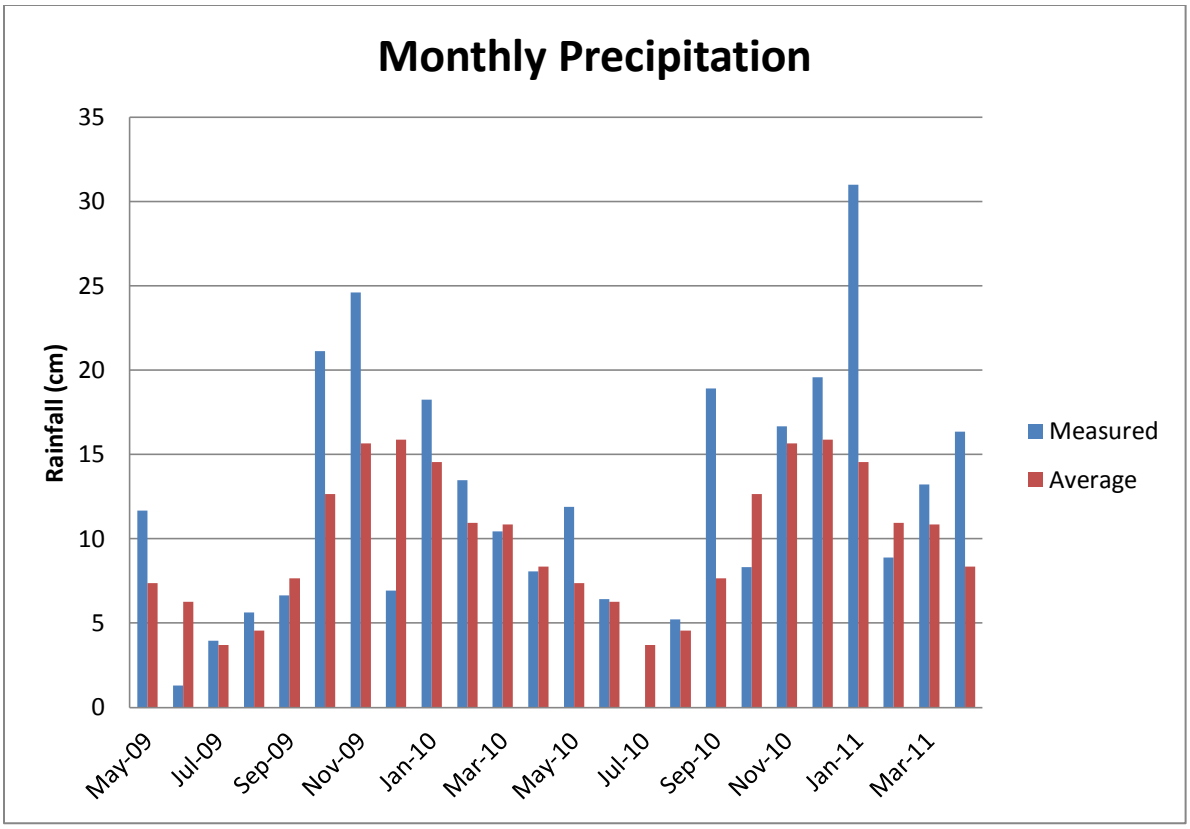

Figure 2 - Monthly precipitation at Clearbrook, WA weather station over the course of this study (including the 5 months prior). The average precipitation is based on the past 30 years.

Figure 3 - Aerial view of the toe of the landslide. A nearby logging road, framed in yellow, was one of two road surfaces used to check for discrepancies between the 2006 and 2011 airborne LiDAR datasets (Road B is pictured above).

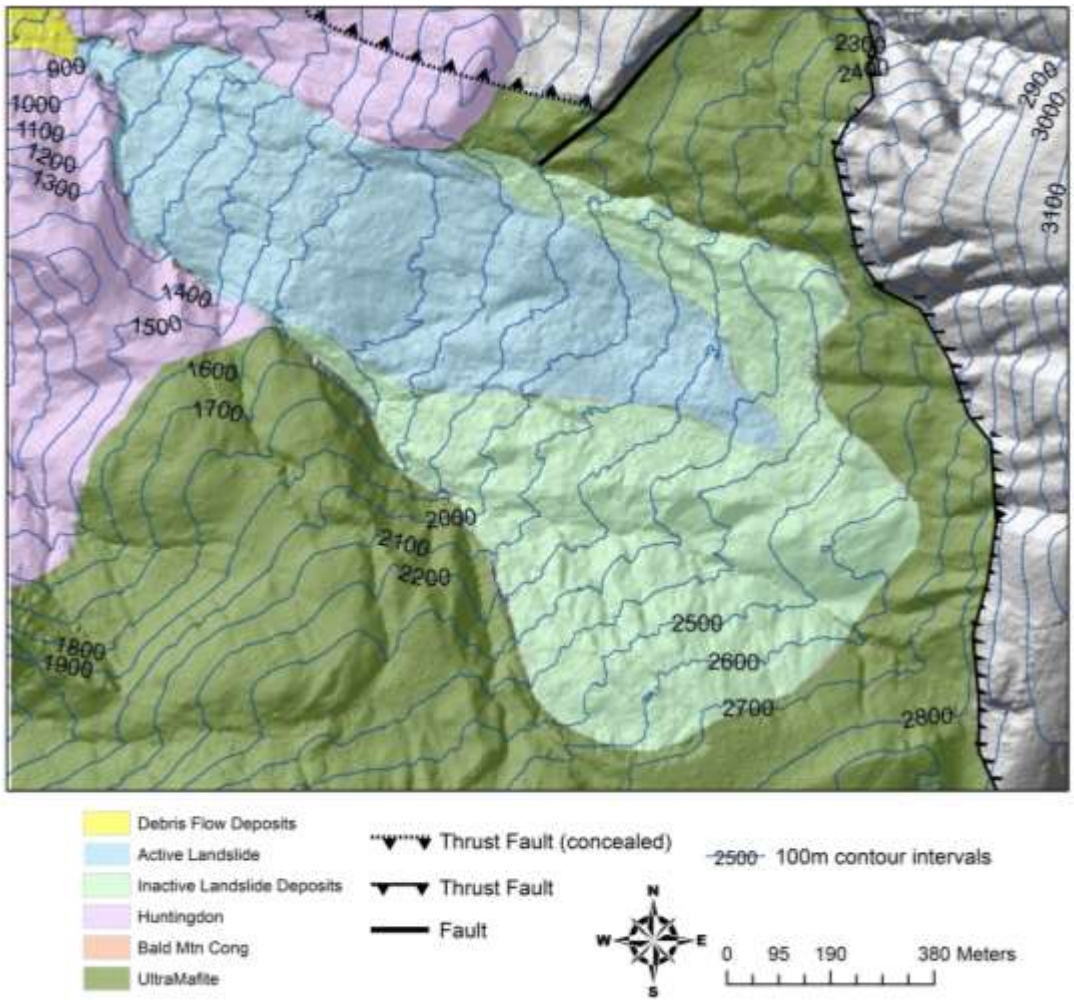

Figure 4 - Generalized geological map of the Swift Creek landslide area (based on (Dragovich et al., 1997).

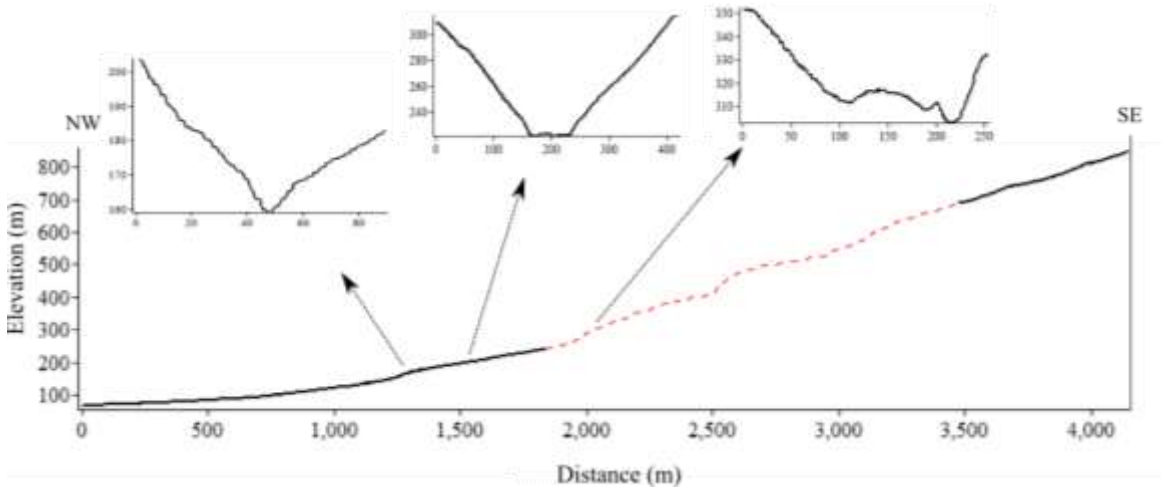

Figure 5 - Topographic profiles across the Swift Creek valley. The three profiles show the landslide, the section below the landslide and the v-shaped channel further downstream.

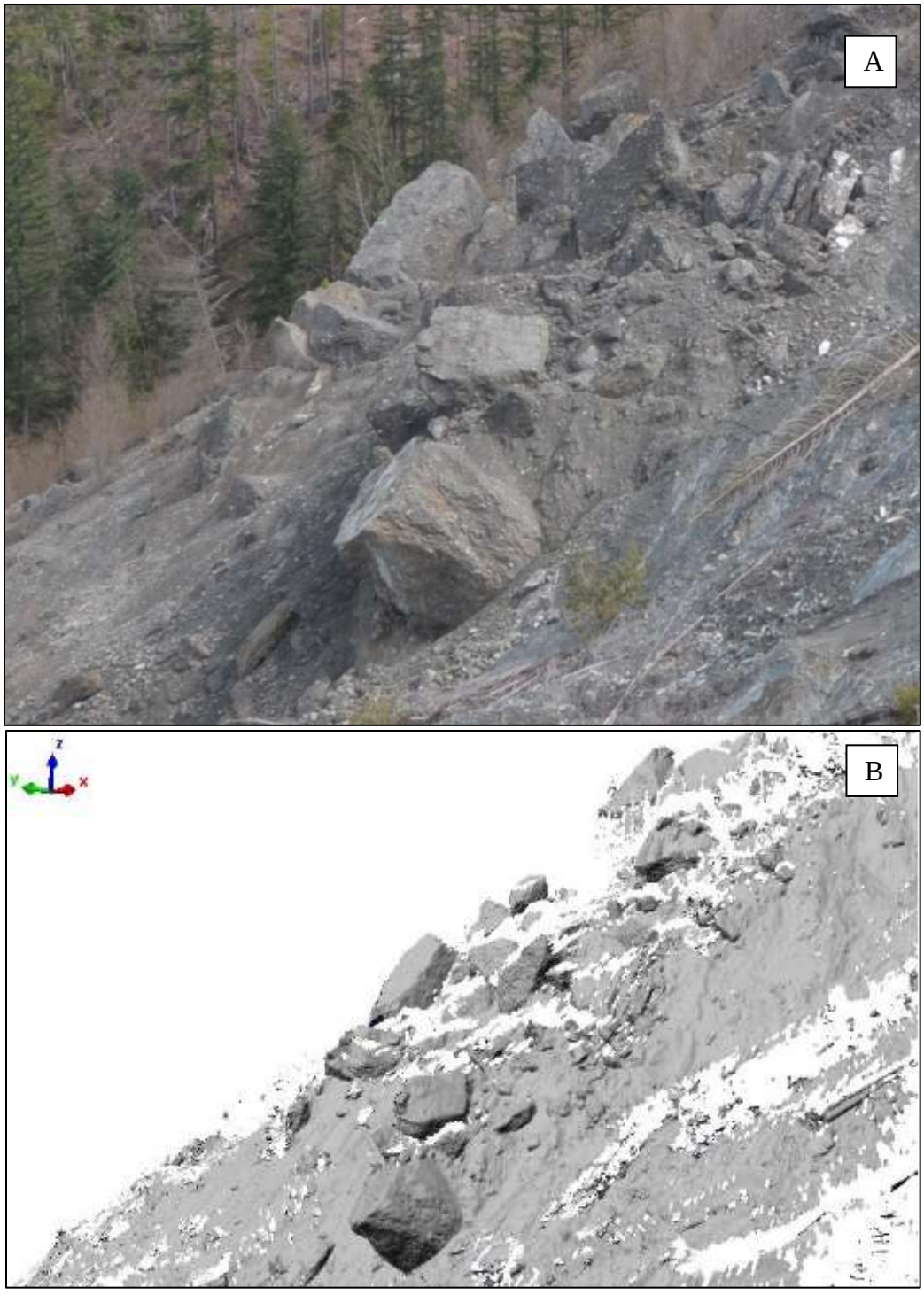

Figure 6 - (a) A photograph of the slow-moving conglomeratic zone (January, 2011). (b) The same area captured by terrestrial LiDAR.

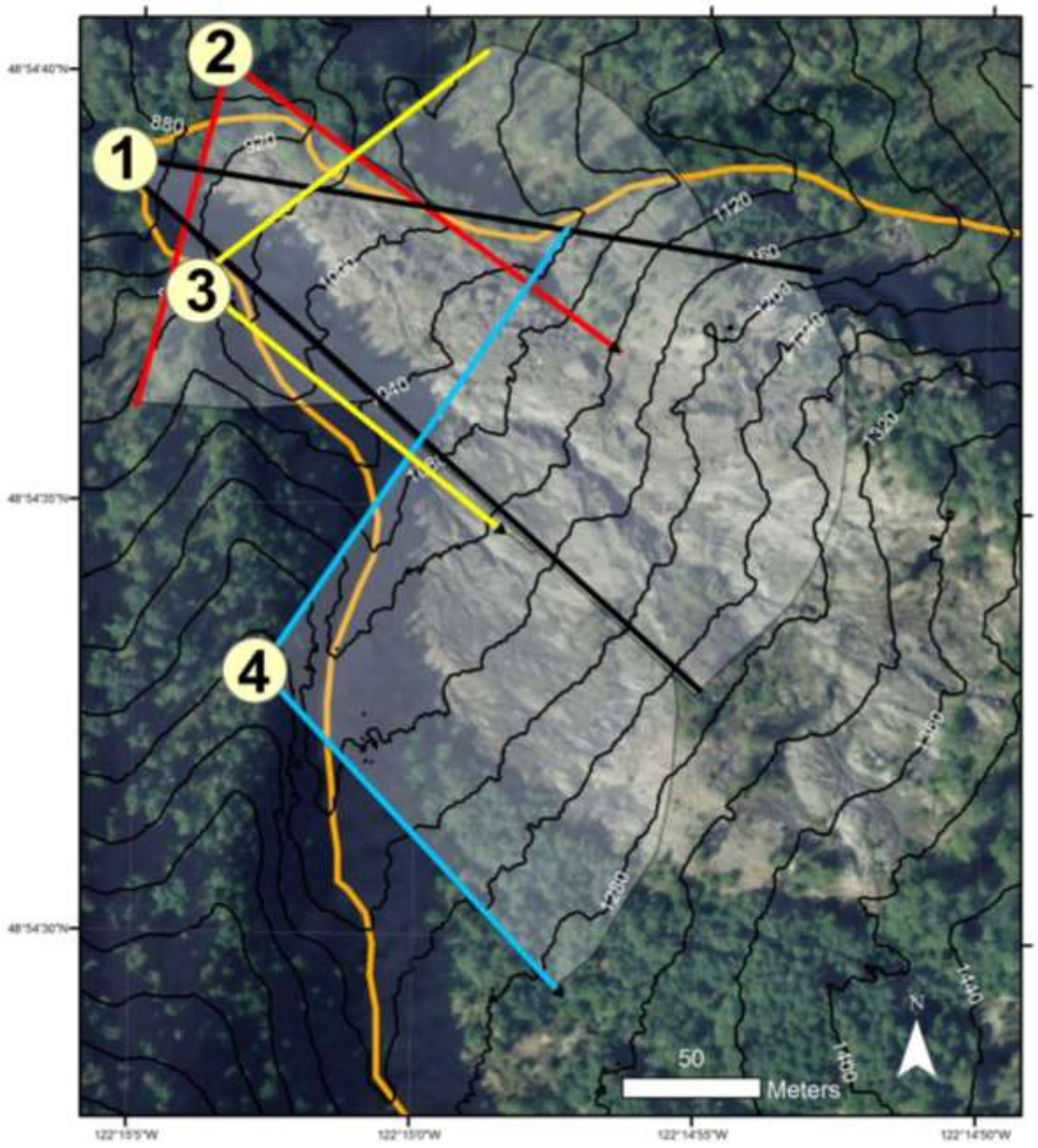

Figure 7 - Overview of the four scanning locations around the toe of the slide. The extent of the landslide is shown in orange and the approximate viewing angles are highlighted in grey (imagery from Google Earth, 2013)

Figure 8 - Photo of the north side of the landslide (May, 2010), showing the network of three artificial targets mounted on stable trees. One target is in the lower-right foreground and the other two are in the upper-left background. The forest and exposed bedrock in the background served as the stable terrain for this study.

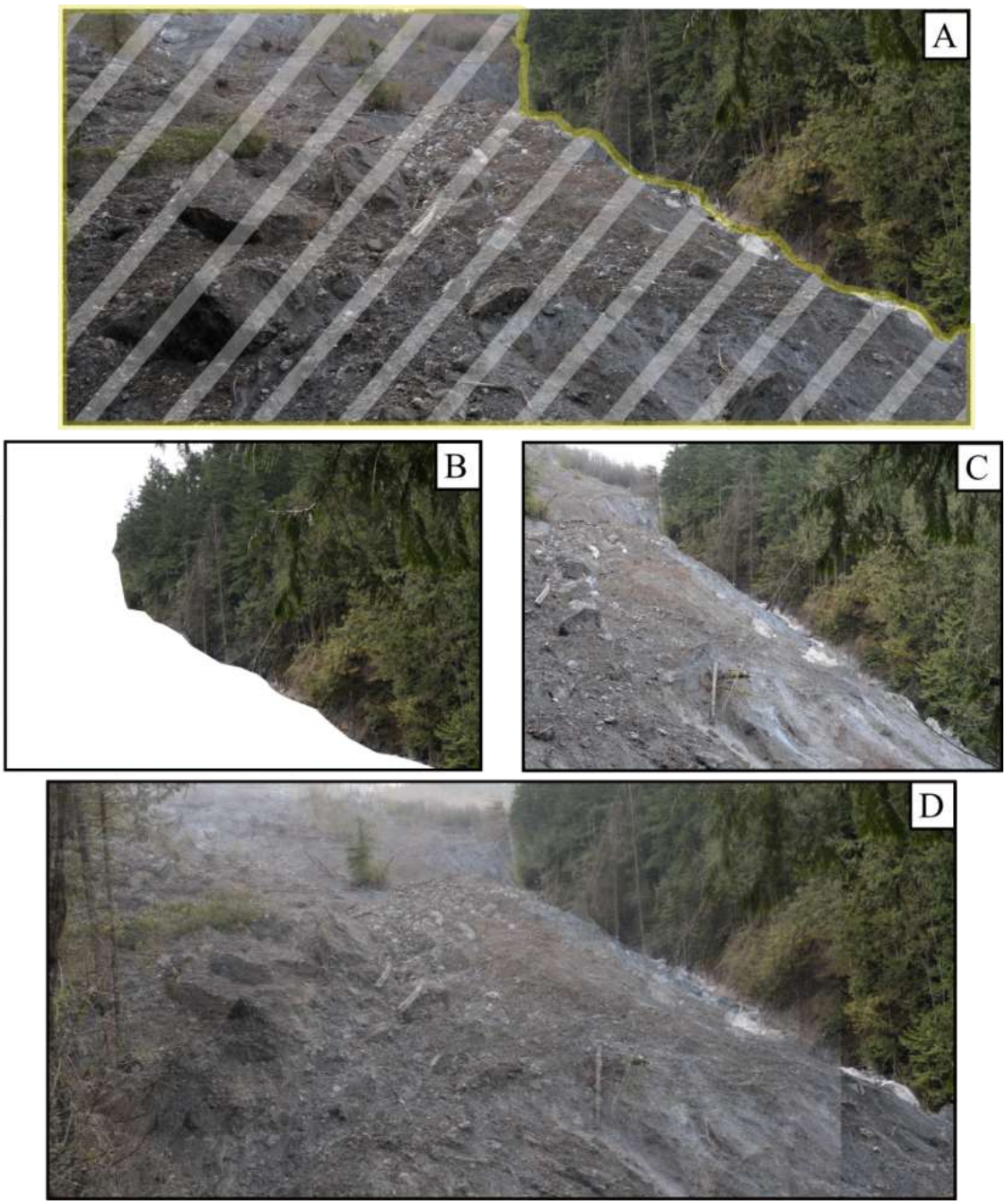

Figure 9 - An overview of the alignment method used in this study. After the initial survey (a), the unstable material in the scene is isolated and removed, leaving only the data for the stable terrain (b). After a subsequent scan (c), the unstable material is again isolated and removed, while retaining the same stable terrain as in the initial survey. Using point matching software, the stable data points can be aligned. Once the stable terrain is aligned, the unstable terrain is recovered and brought back into view (d).

Figure 10 - The Optech ILRIS 3D laser scanner from a position on the north side of the landslide (October, 2009).

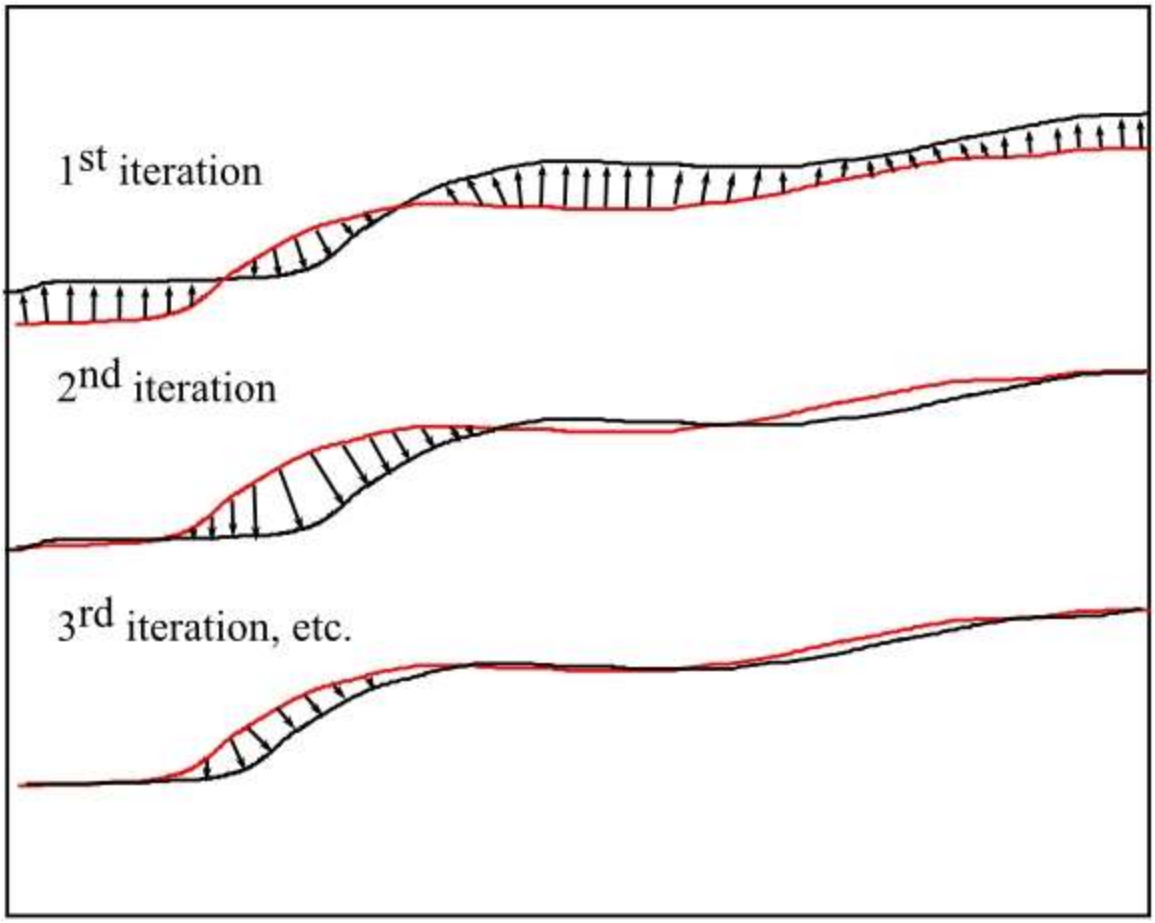

Figure 11 - Basics of the ICP alignment algorithm. For each point in reference point cloud *A (shown in red)*, its nearest neighboring point is located in point cloud *B (black)*, based on the minimum Euclidean distance between points. Using an optimization function based on the sum of the squared distances between neighboring points, the rigid transformation which best represents the relationship between the two point clouds is carried out.

In the simple schematic example above, nearest neighboring points are identified during the first iteration. A transformation was then completed on point cloud *B* which resulted in a shift downward. During the second iteration, neighboring points are much closer, yet still not aligned. This continues in an iterative process until the RMSD value falls below a defined threshold.

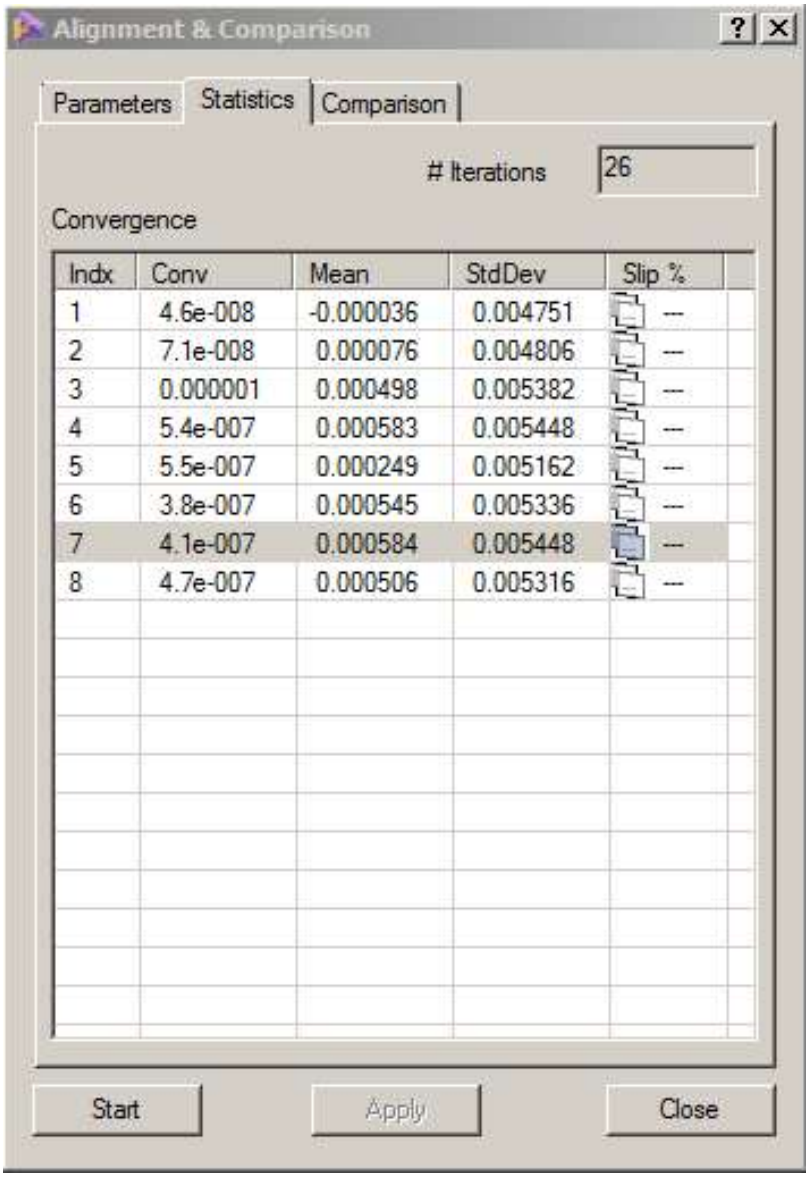

Figure 12 - This example from the January, 2011 TLS dataset shows the typical results of aligning contemporaneous scans. In this case, a total of 8 scans were acquired and aligned to one another through an automated surface matching application within the Polyworks environment (Innovmetric, 2010). These results show an uncertainty of about 5 mm in the alignment process.

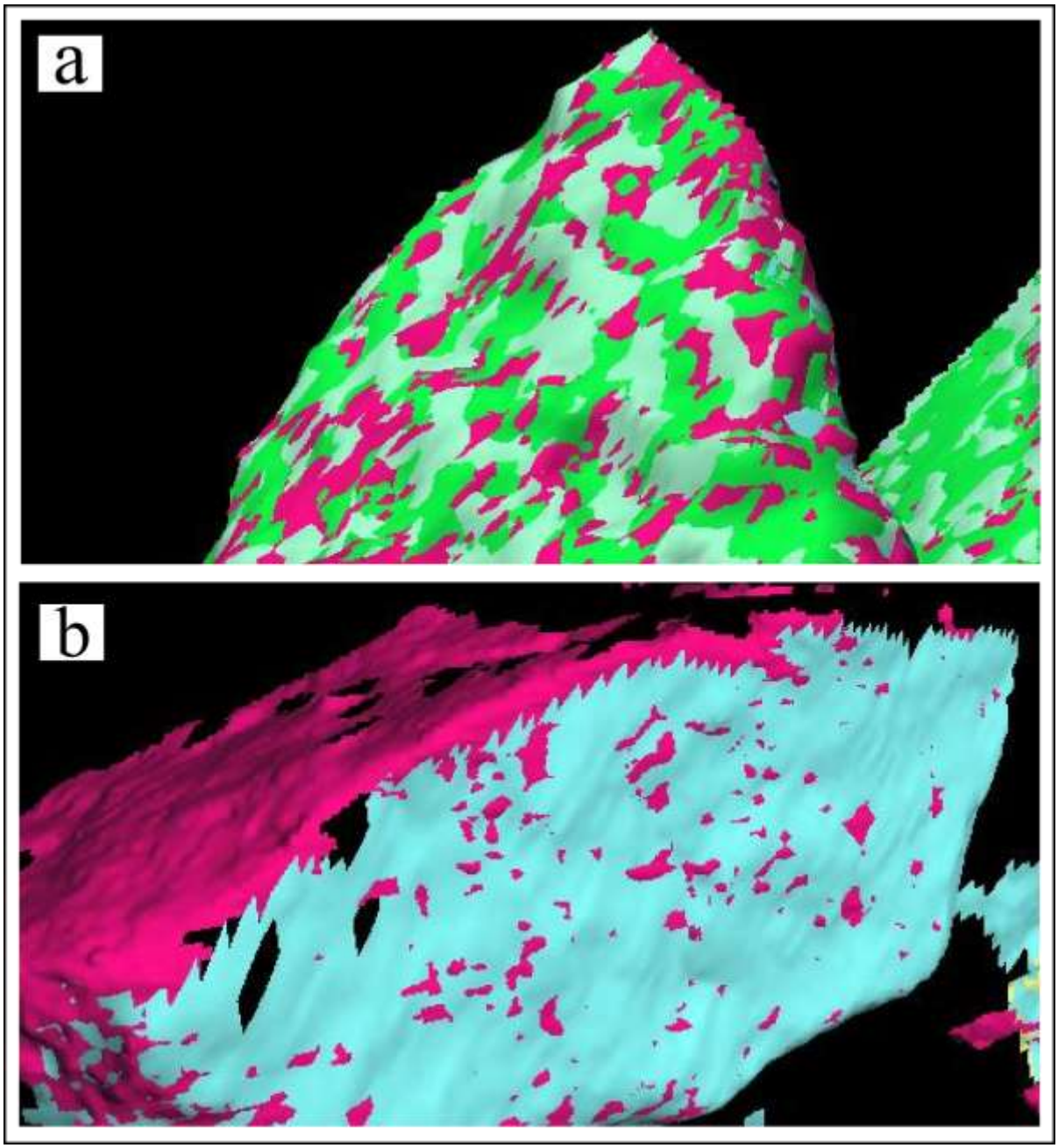

Figure 13 - Two point clouds (shown with a draped mesh) illustrating the variability in alignment. The figure on top (a) is an example of a good alignment of three separate scans. The rock face shows an even distribution of colors (i.e., scans) with no single color dominating the others. The bottom example (b) shows a poorer alignment. The rock face was surveyed in two scans, yet the scan shown in blue is mostly in front of the scan shown in magenta.

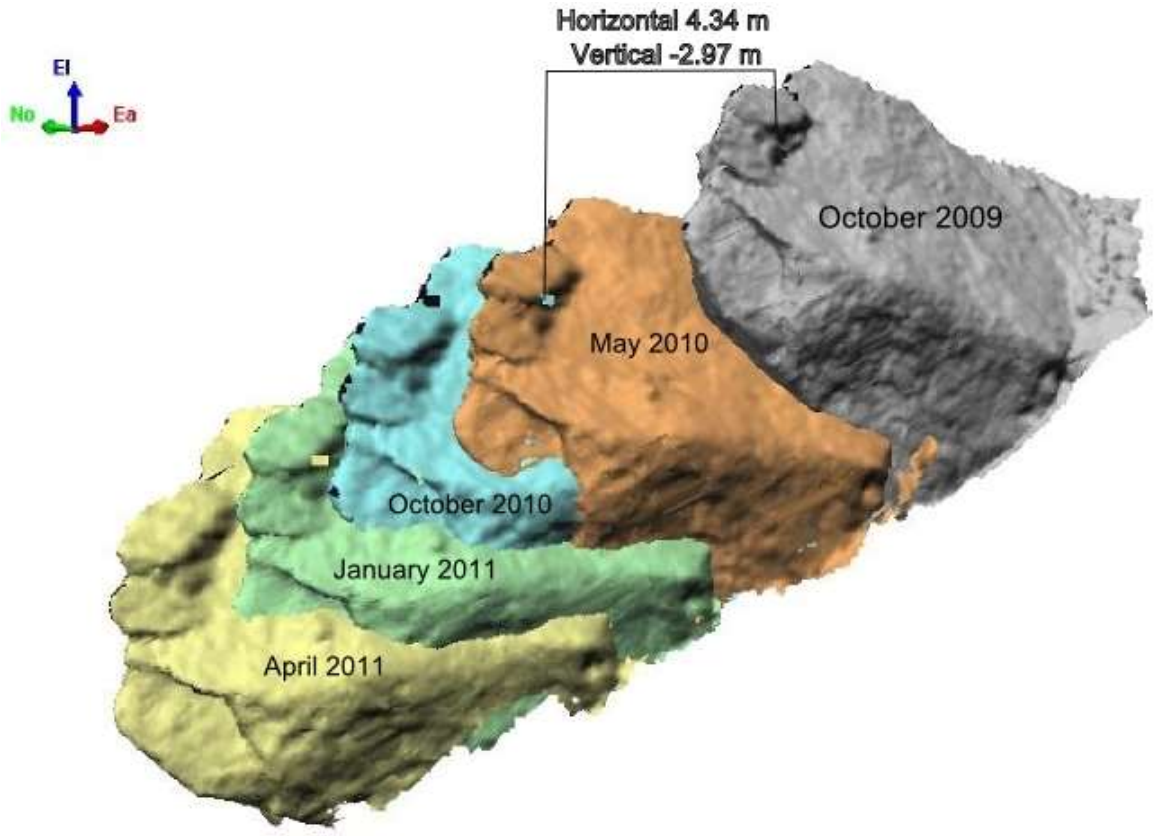

Figure 14 - An example of an isolated boulder, produced from LiDAR point-cloud data and shown with a mesh surface interpolation

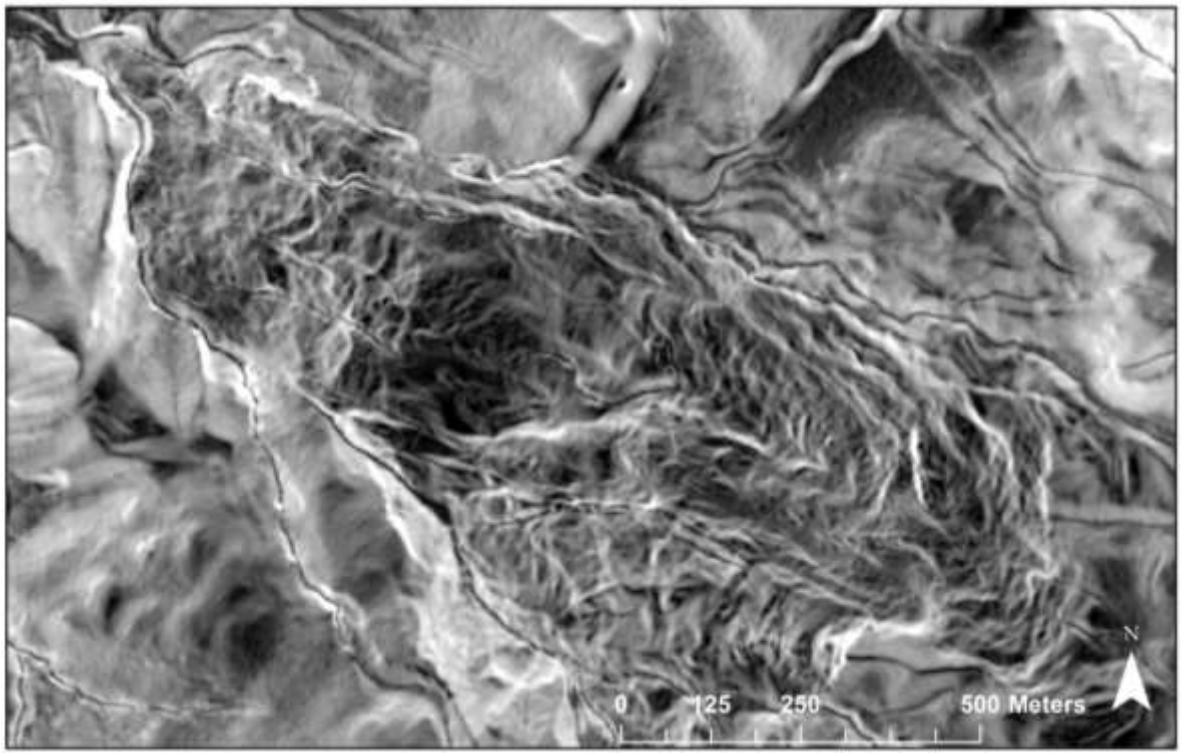

Figure 15 - Greyscale slope-gradient image based upon DEM from the 2011 airborne LiDAR dataset. This image, along with a similar image produced from the 2006 airborne LiDAR dataset were used to measure surface displacement with PIV in MATLAB.

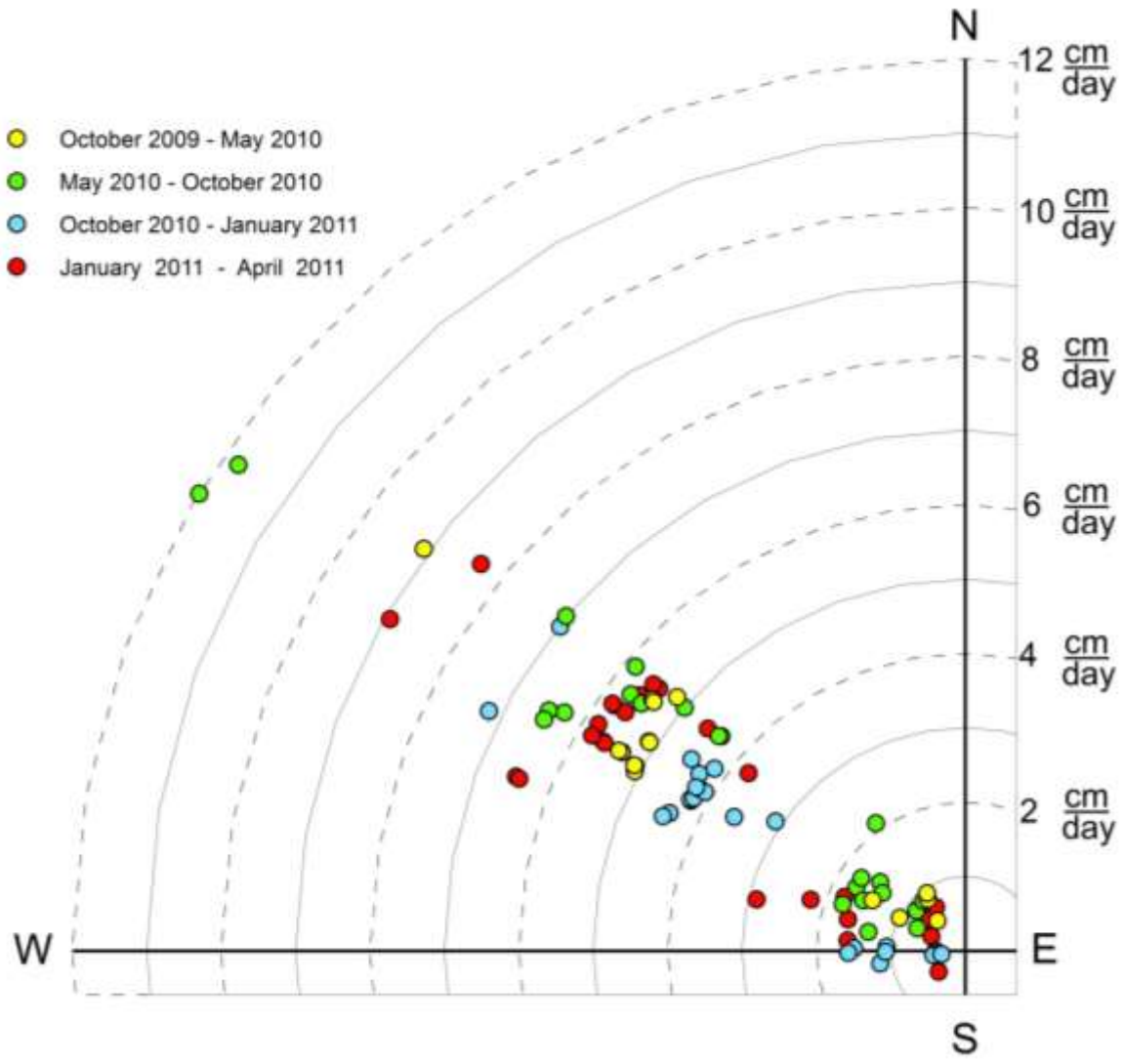

Figure 16 - Average daily velocities for 25 boulders acquired during 5 survey campaigns, covering 18 months of movement. The displacement rates were obtained via an ICP matching application using terrestrial LiDAR data.

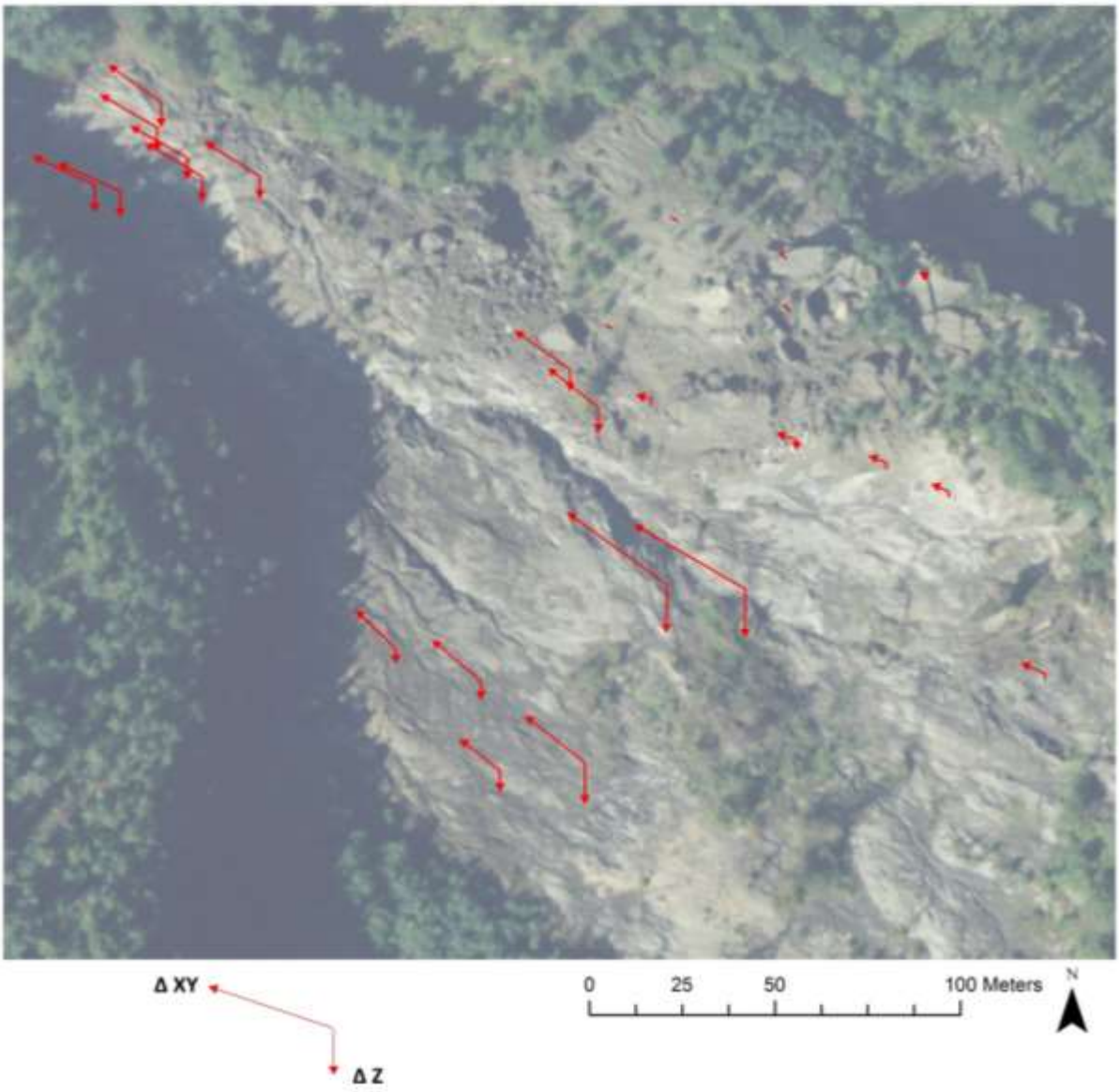

Figure 17 - Cumulative displacement vectors for the 25 boulders on the toe of the landslide (from October, 2009 to April, 2011) were obtained using the ICP algorithm with data acquired by terrestrial LiDAR. All of the boulders recorded a drop in elevation during each of the four intervals (see Figure 48). Although the data are quite precise (uncertainty less than about 5 cm), the spatial coverage is limited.

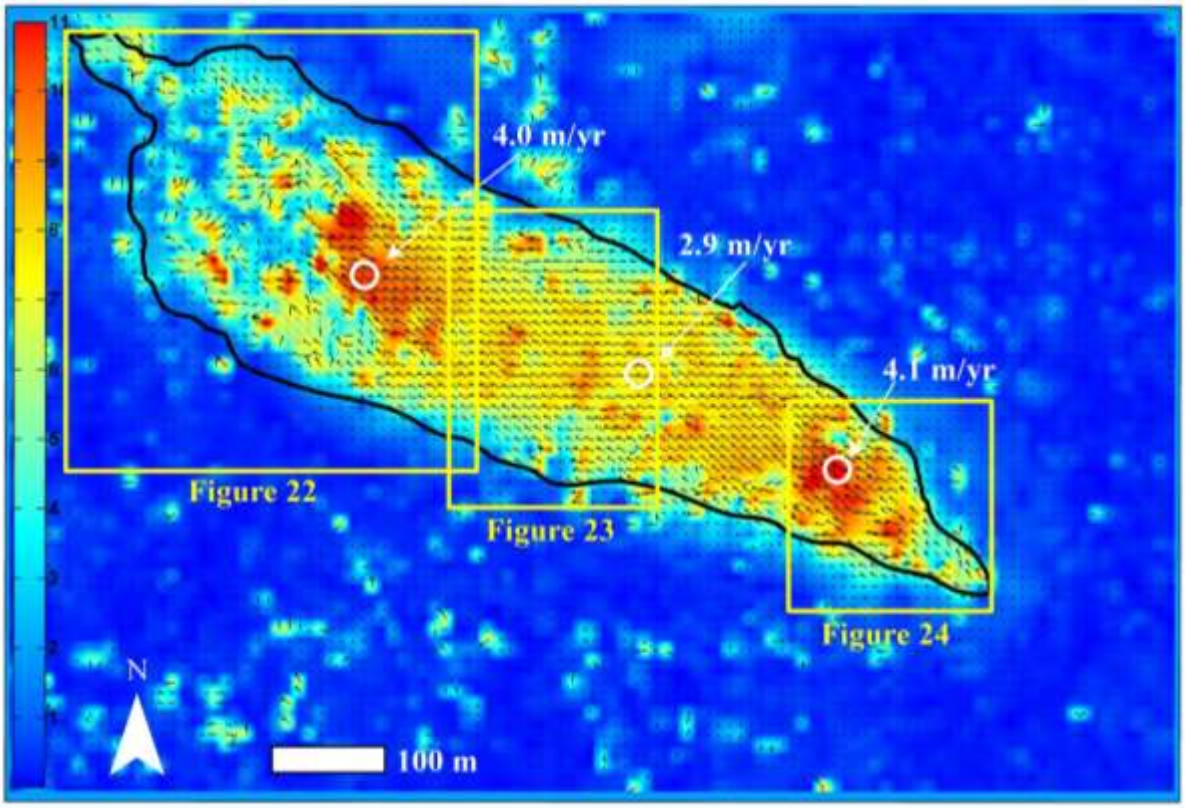

Figure 18 - Surface displacement vectors and their magnitudes, obtained using PIV analysis of airborne LiDAR data. The color scale is in pixels (1 pixel = 1.8 m). Individual pixel vectors and the associated velocities are shown in white.

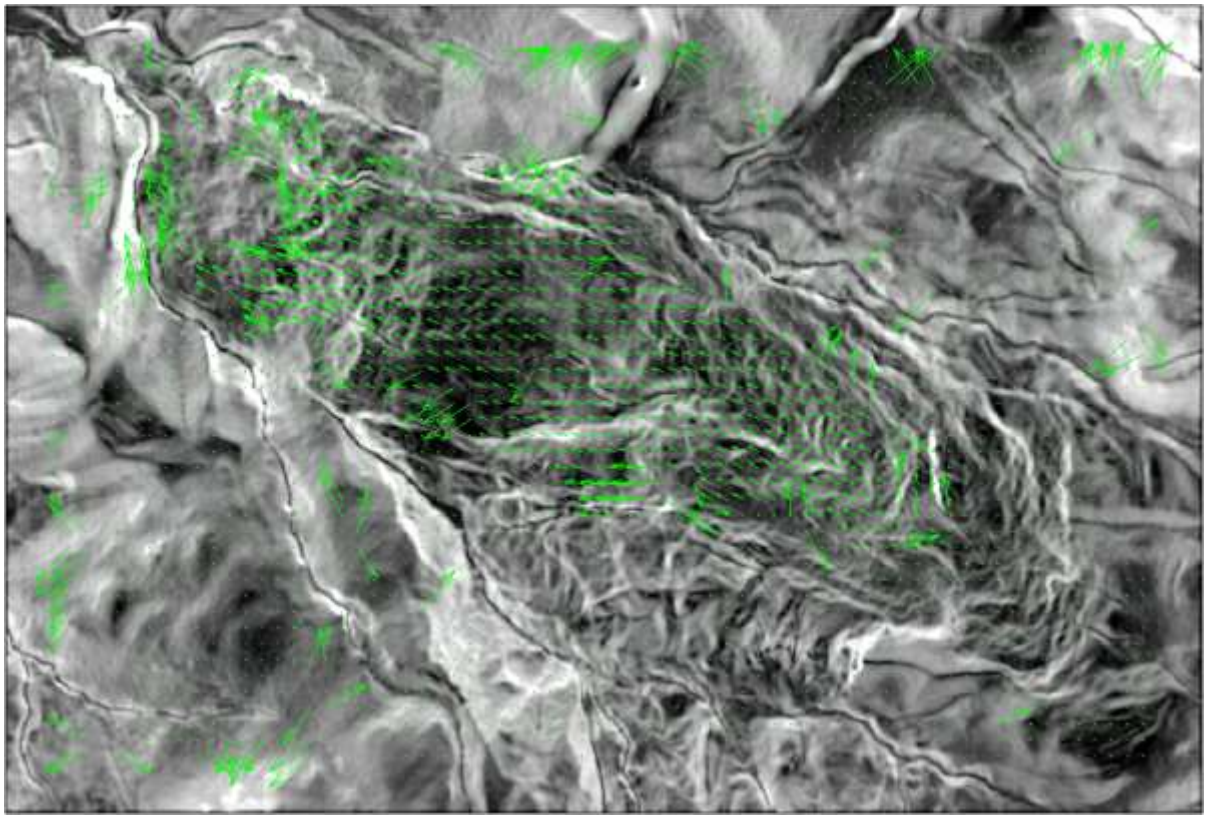

Figure 19 - The initial results of PIV reveal a significant number of erroneous vectors. The data was cleaned up using a filter and manually removing the remaining invalid vectors.

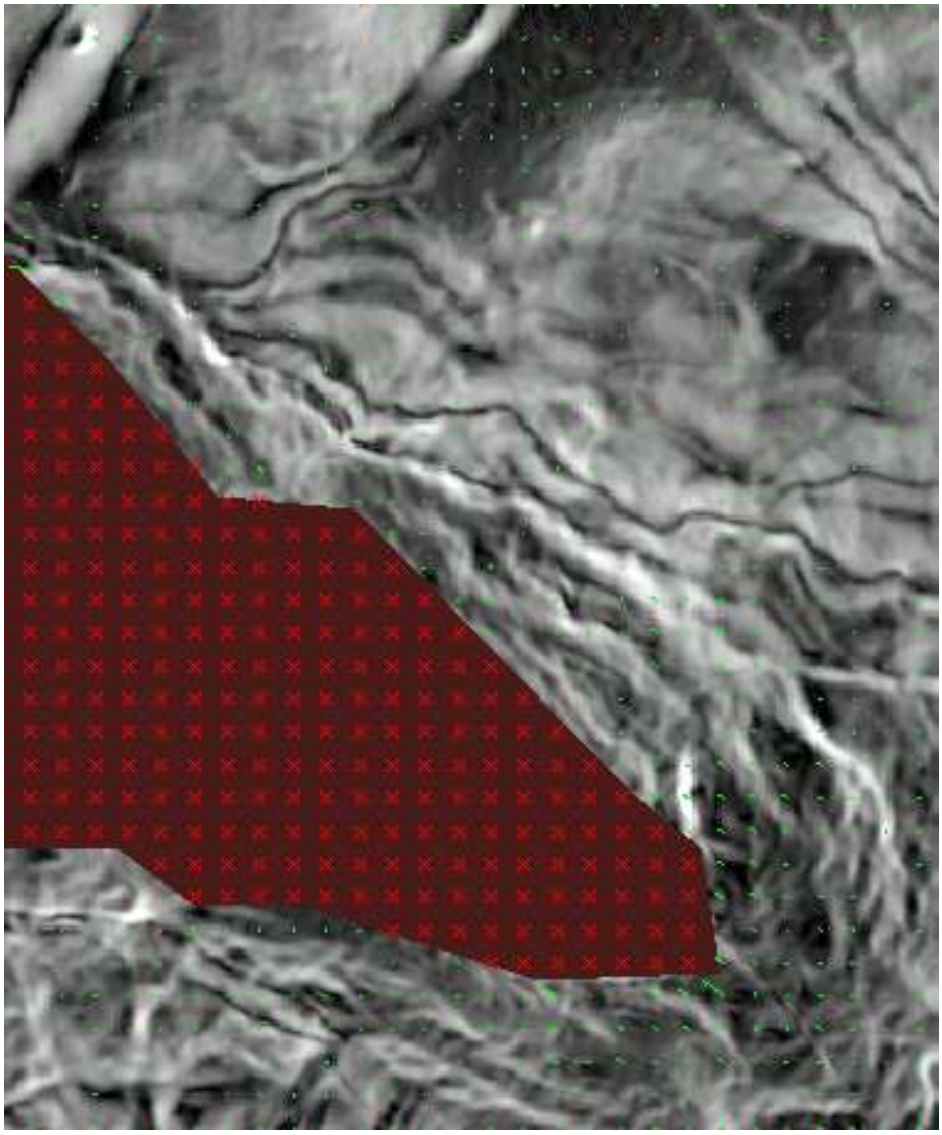

Figure 20 - In order to estimate the accuracy of the PIV method, the unstable terrain was removed (via mask) and the stable regions around the landslide were compared via PIV analysis.

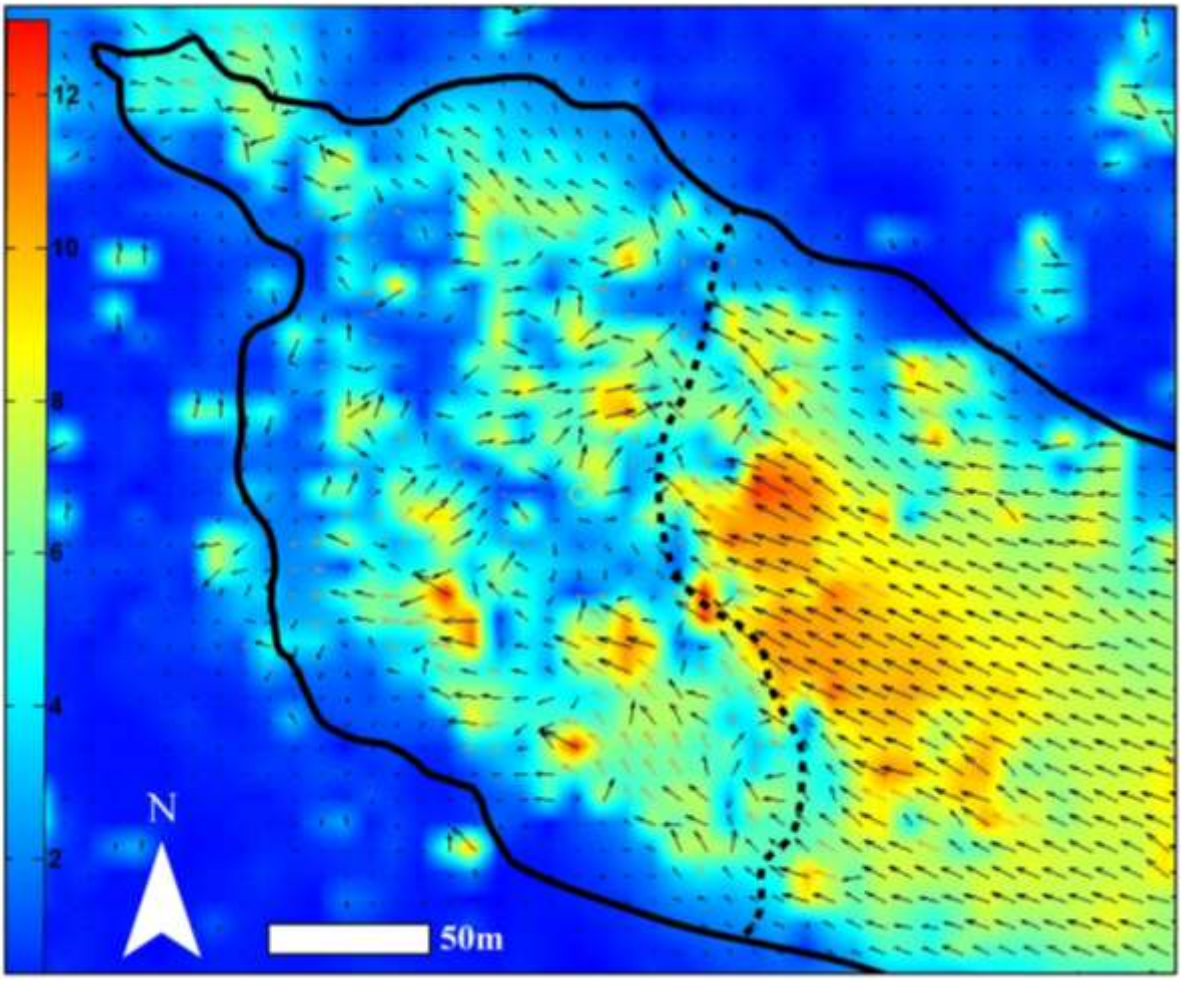

Figure 21 - PIV analysis using airborne LiDAR acquired in 2006 and 2011, highlighting movement in the toe region. The scale is in pixels (1 pixel = 1.8 m). The dashed line approximates the transition from forested, intact soils to the disturbed and unvegetated material on the toe.

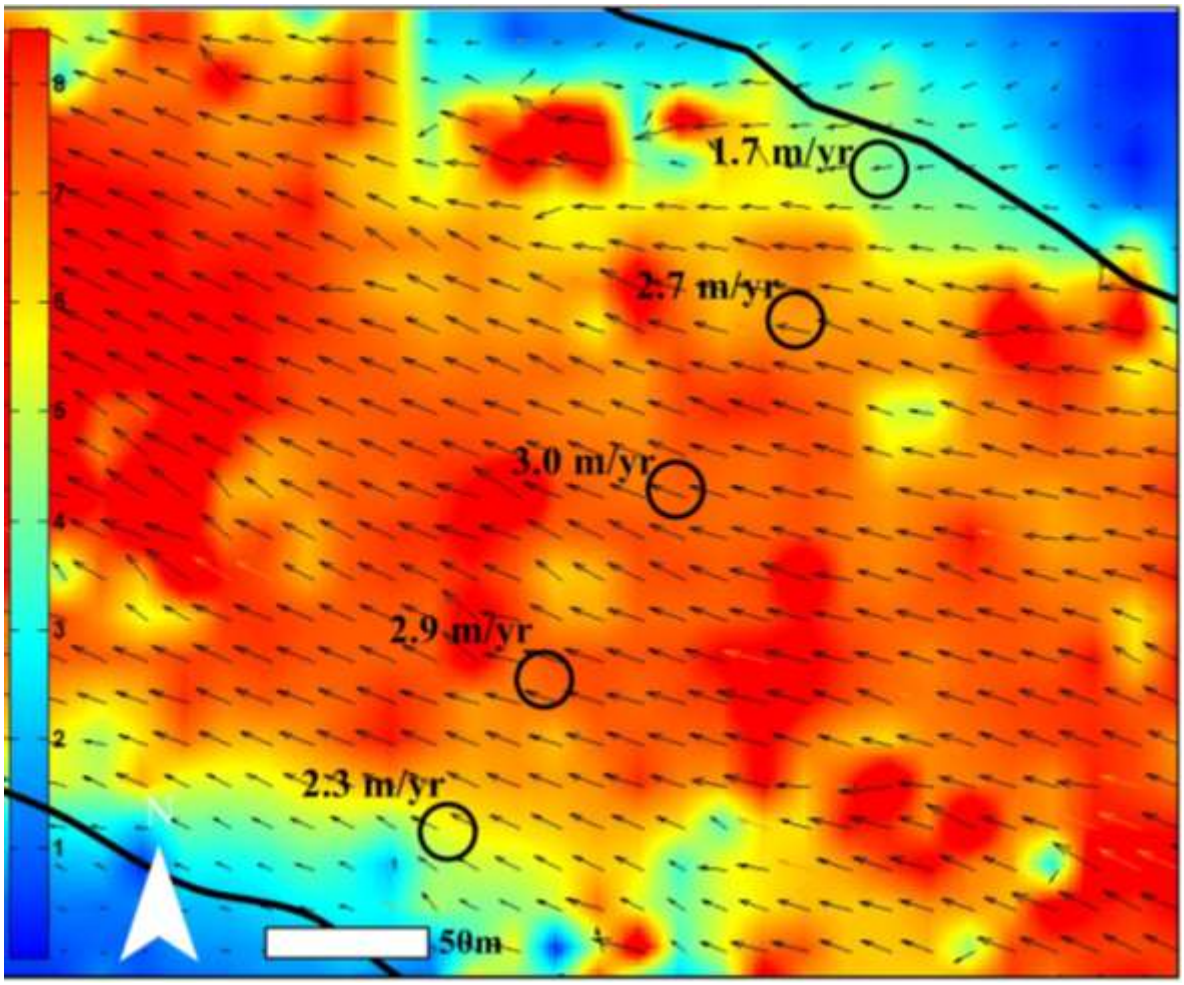

Figure 22 - PIV analysis of the central portion of the main body of the landslide, obtained from airborne LiDAR acquired in 2006 and 2011. The scale is in pixels (1 pixel = 1.8 m). The highest velocities occur in the middle of the flow and decrease along the margins.

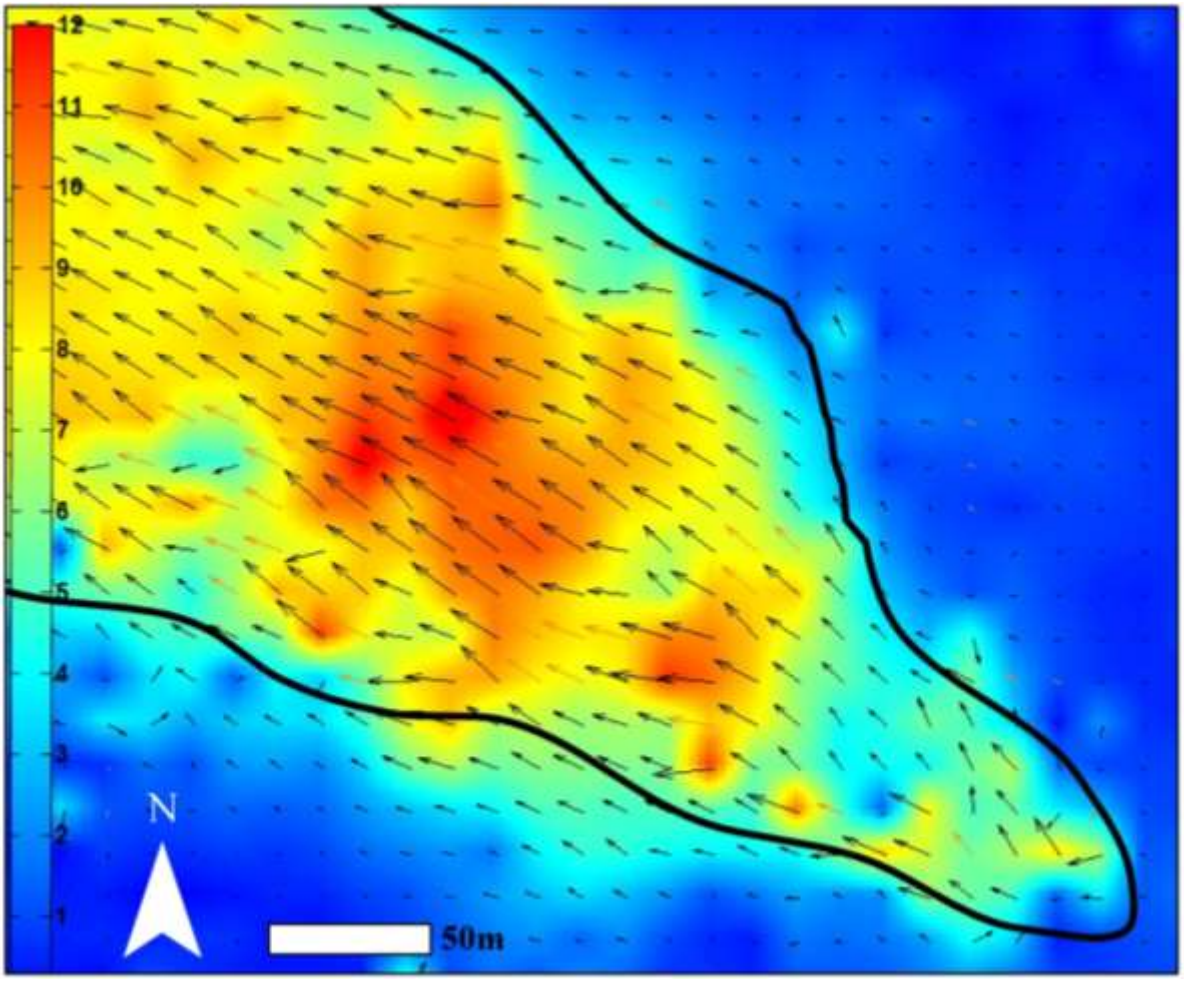

Figure 23 - PIV analysis using airborne LiDAR acquired in 2006 and 2011, highlighting movement at the head of the earth flow.

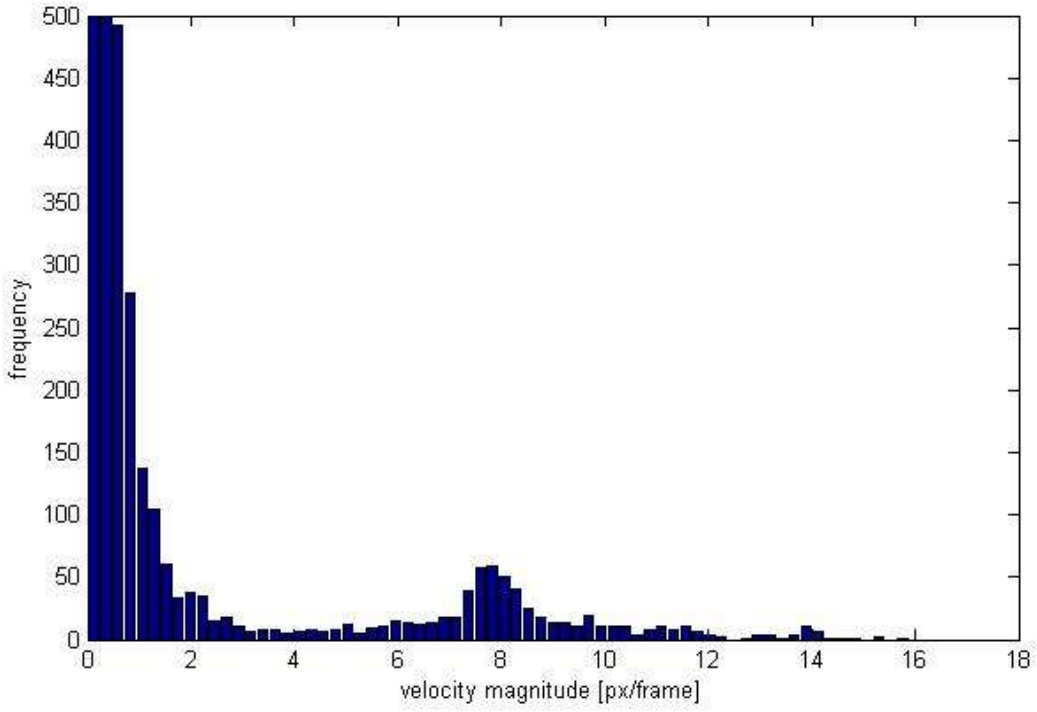

Figure 24 - A histogram showing the velocity distribution of vectors on the Swift Creek landslide obtained by way of PIV. The main mass of the earth flow was displaced around 7.8 pixels during the 5 years (1699 days) between surveys. With a pixel size of 1.8 m x 1.8 m, this yields an annual displacement rate of around 3.0 meters per year.

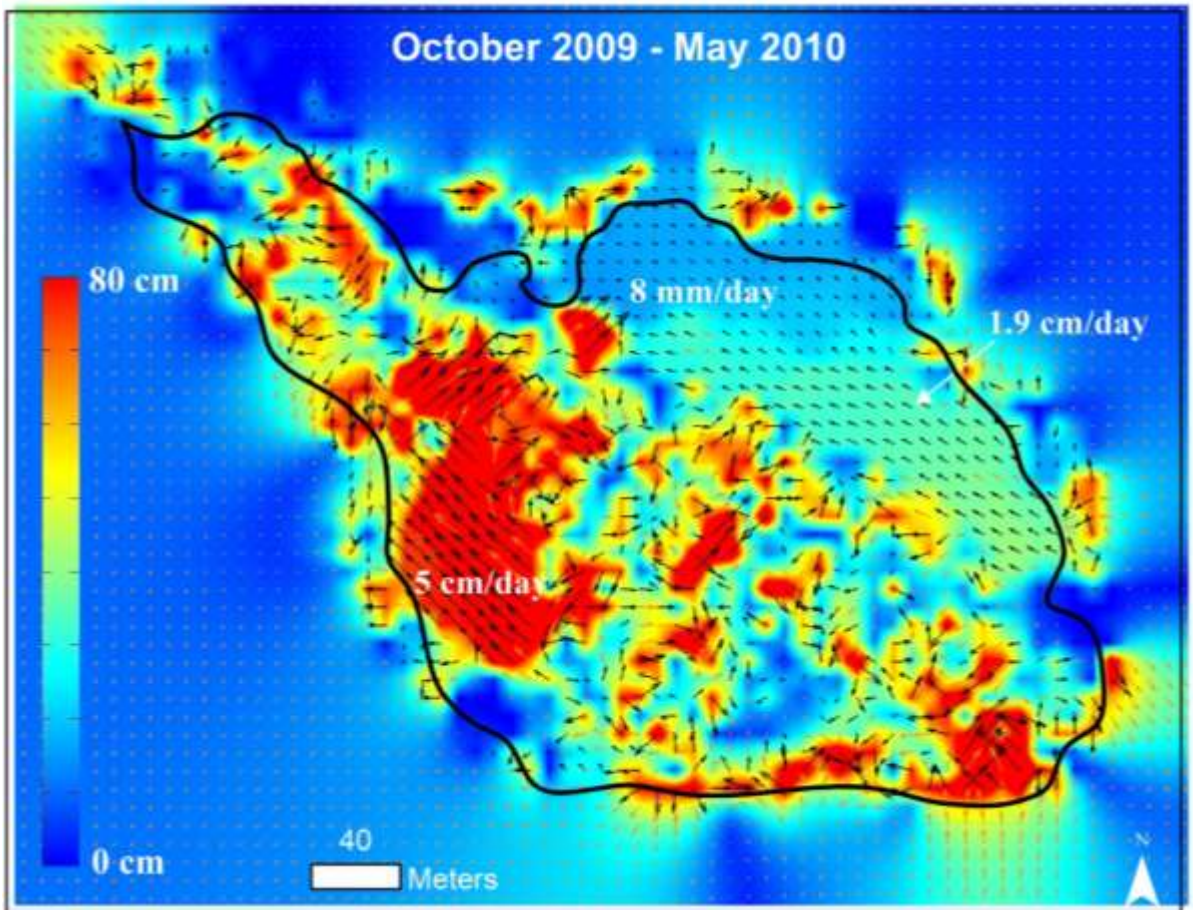

Figure 25 - PIV analysis of the toe using slope-gradient image pairs derived from DEMs and TLS data covering October, 2009 – May, 2010. The scale represents cumulative displacement during the interval; calculated average daily velocities are shown in white.

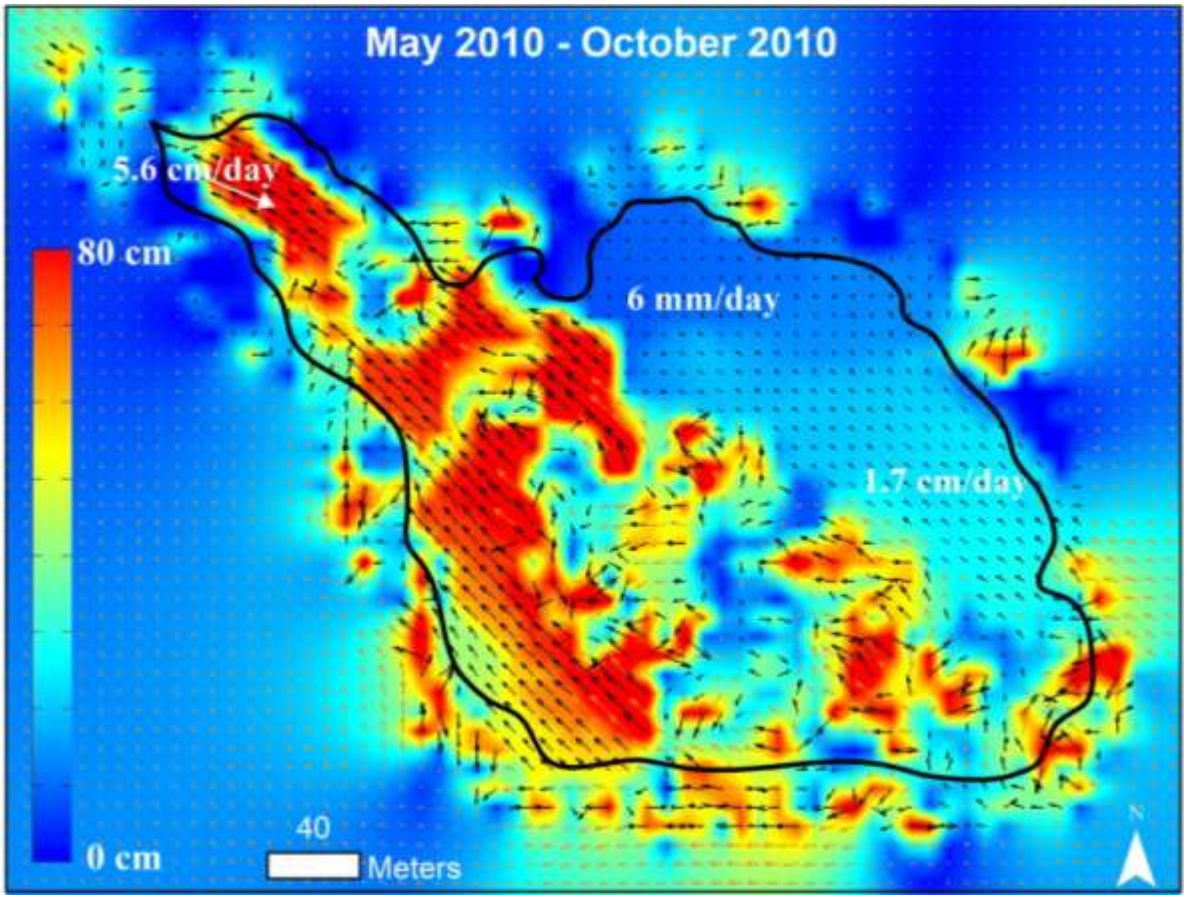

Figure 26 - PIV analysis of the toe using slope-gradient image pairs derived from DEMs and TLS data. This period spans May, 2010 – October, 2010. The scale represents cumulative displacement during the interval; calculated average daily velocities are shown in white.

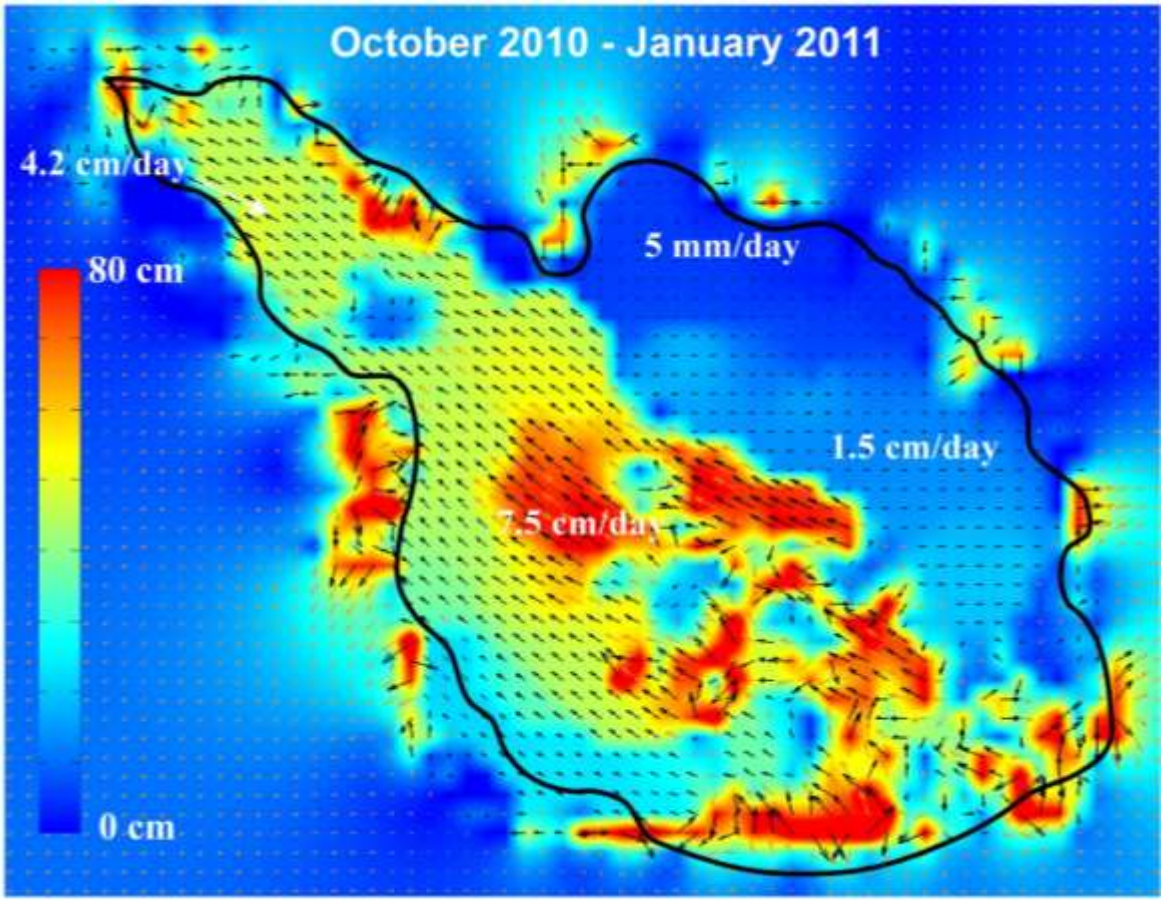

Figure 27 - PIV analysis of the toe using slope-gradient image pairs derived from DEMs and TLS data between October, 2010 – January, 2011. The scale represents cumulative displacement during the interval; calculated average daily velocities are shown in white.

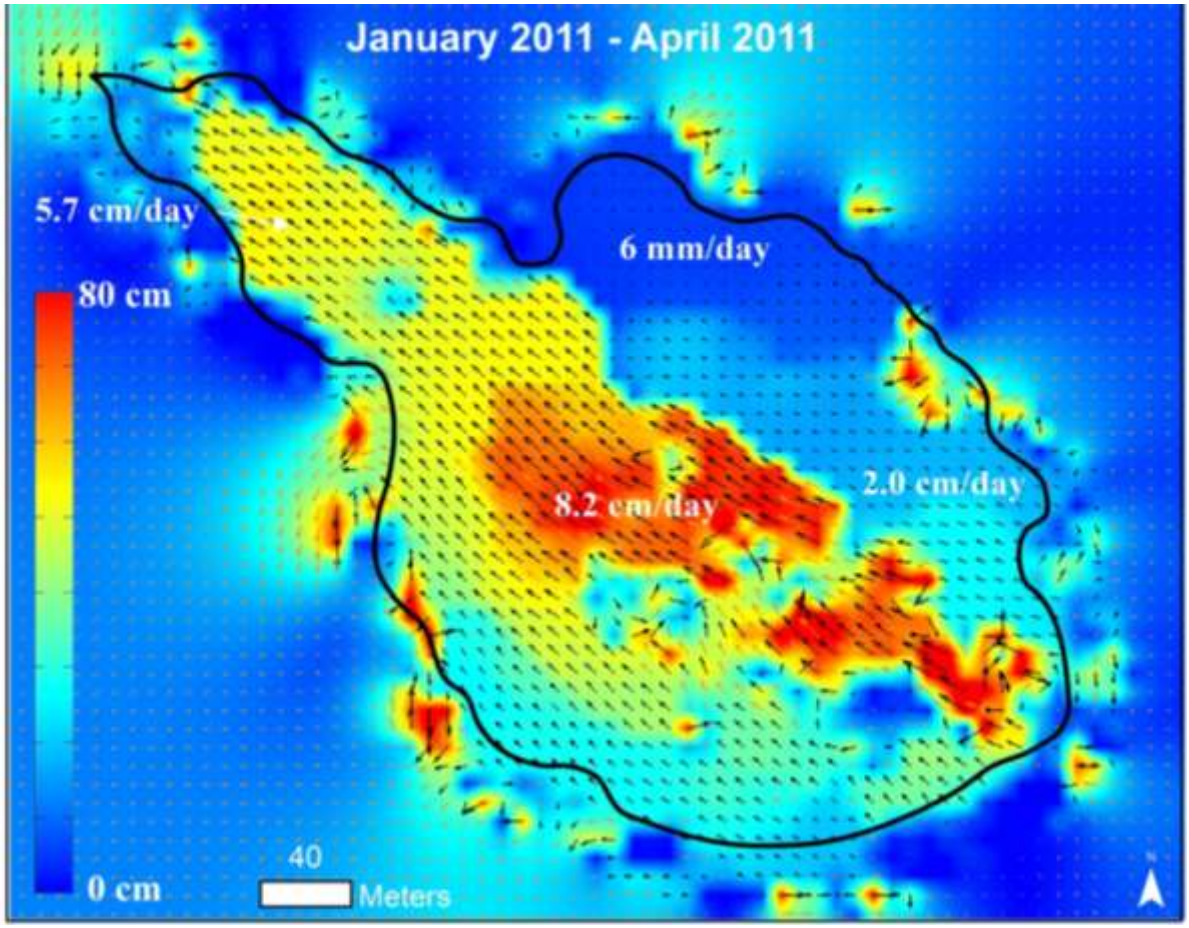

Figure 28 - PIV analysis of the toe using slope-gradient image pairs derived from DEMs and TLS data covering January – April, 2011. The scale represents cumulative displacement during the interval; calculated average daily velocities are shown in white.

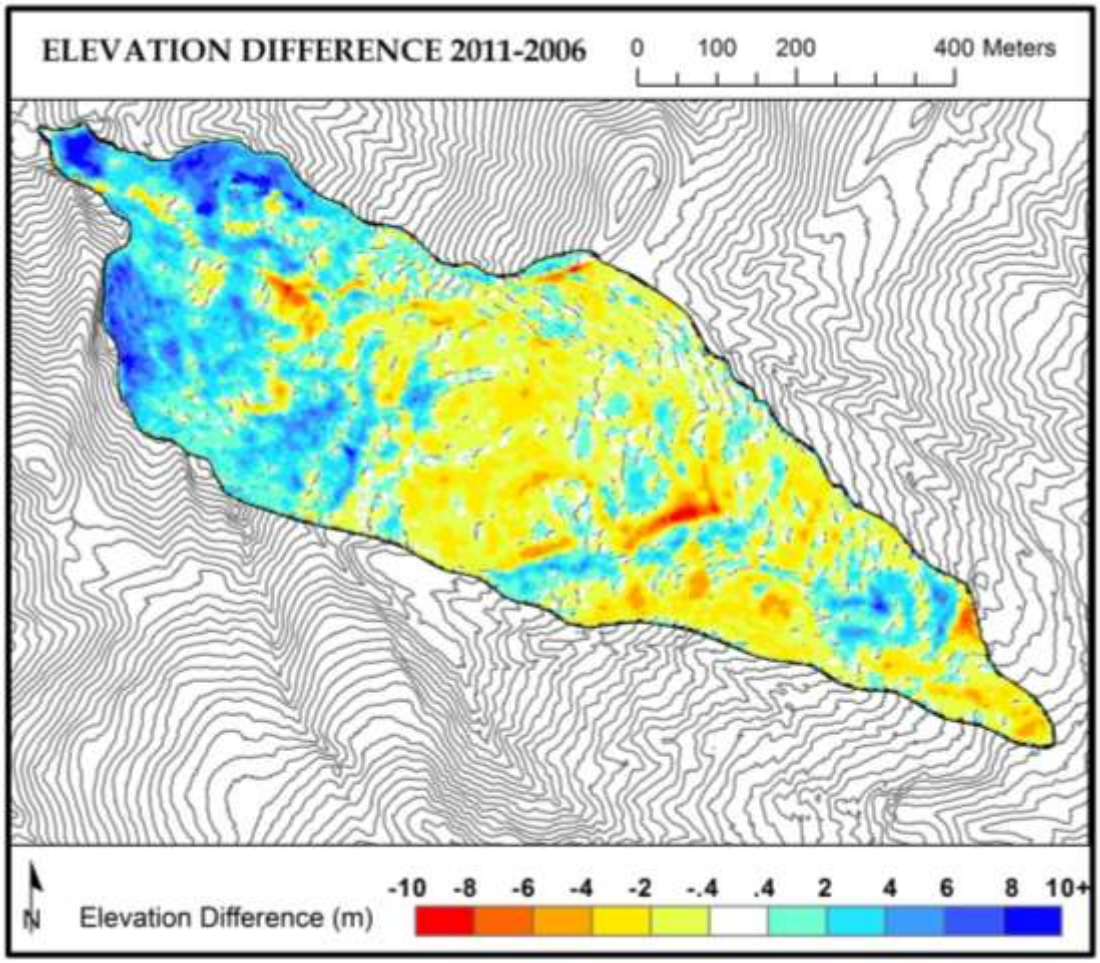

Figure 29 - DEM of difference produced by subtracting the 2006 DEM from the adjusted 2011 DEM. Both DEMs were created from airborne LiDAR data. The 20 meter contour lines shown were derived from the 2011 DEM. The threshold for change detection is plus or minus 40 cm.

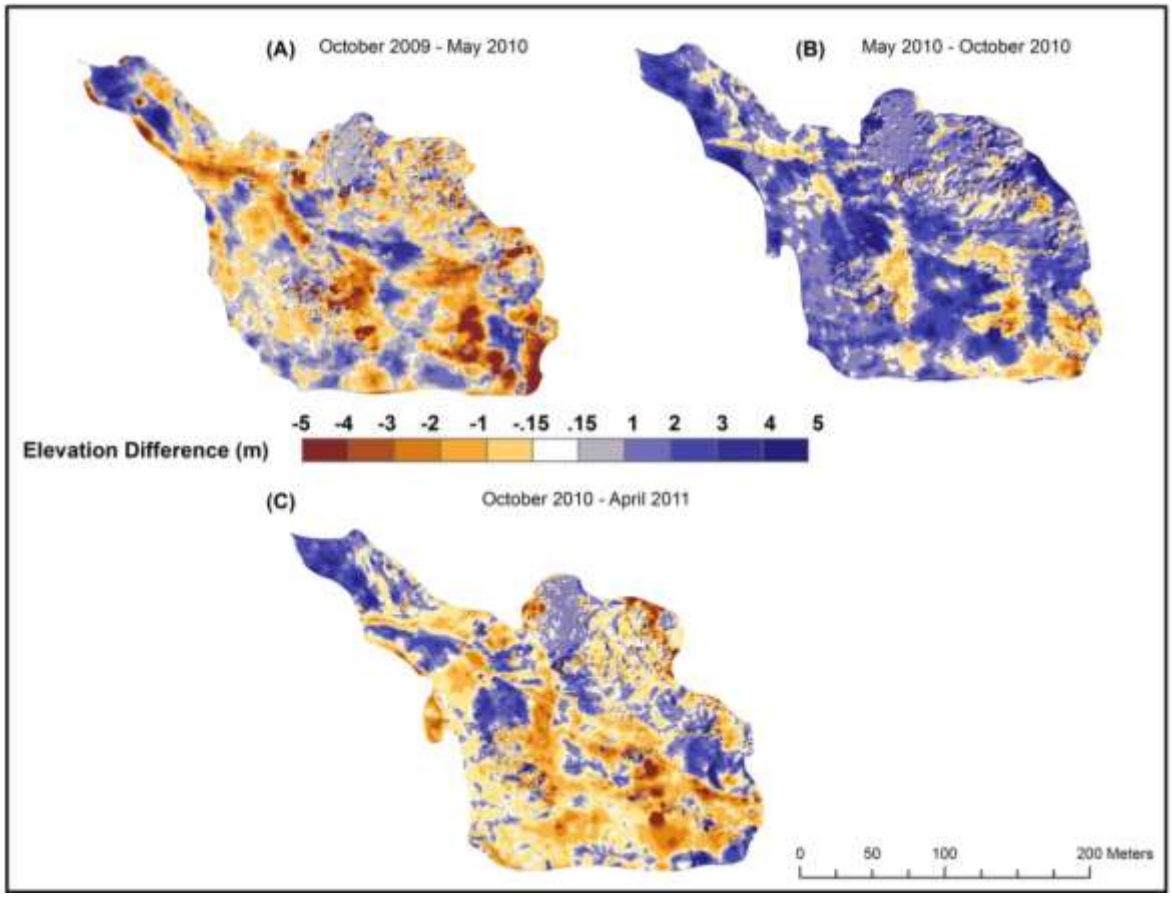

Figure 30 - A series of change detection maps of the toe area. Two of the periods cover the wet seasons (October through April) while the other represents the dry season (May through September).

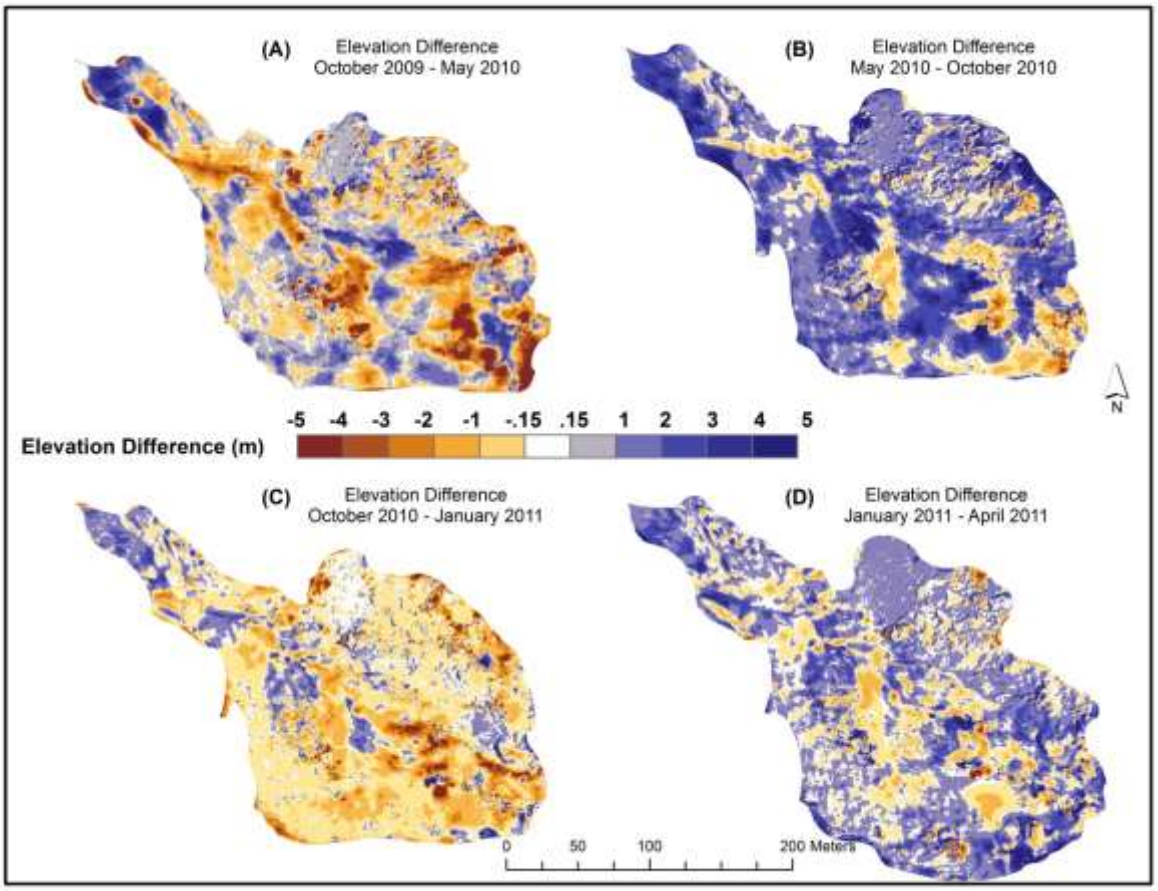

Figure 31 - A series of change detection maps of the toe area covering all four intervals used in this study.

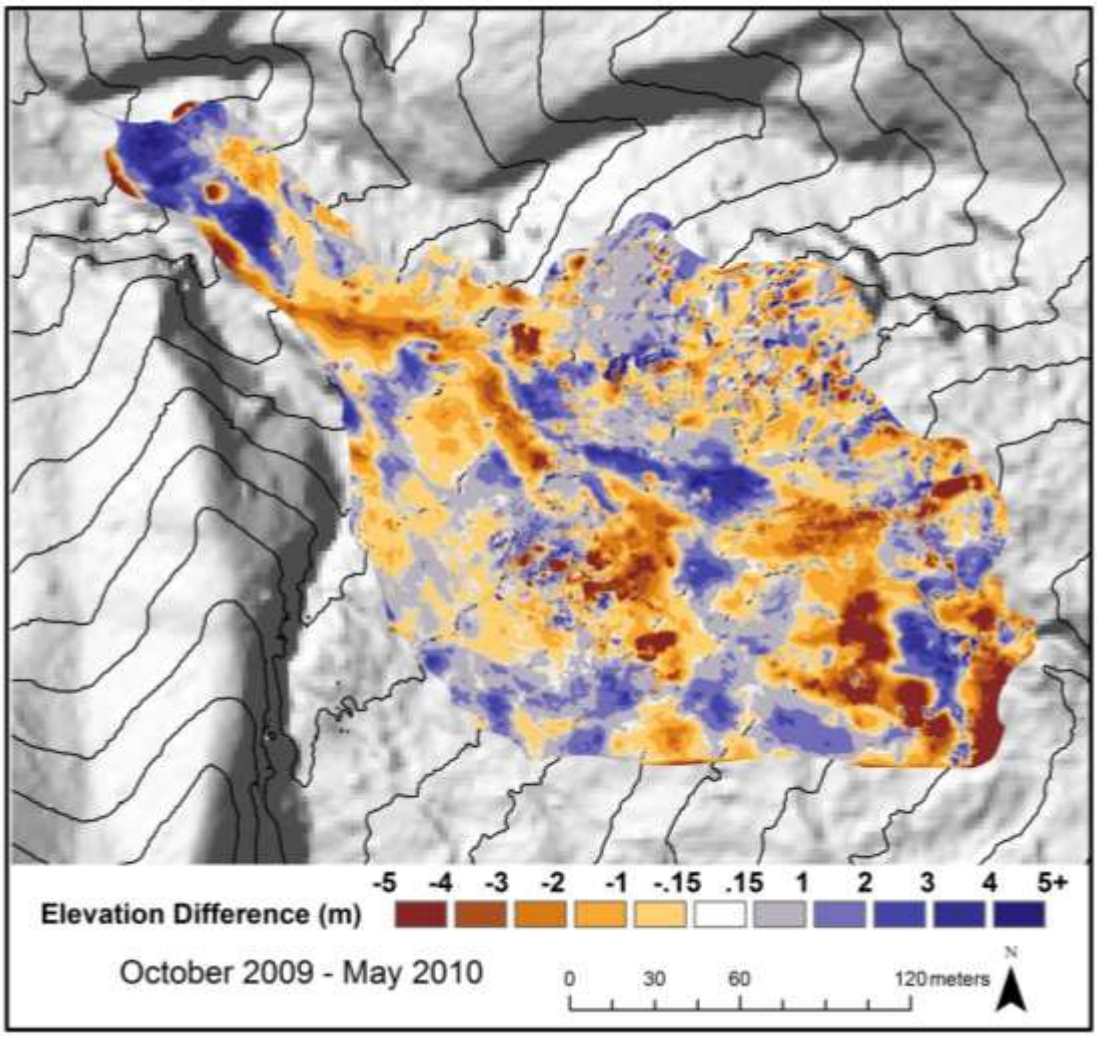

Figure 32 - DEM of difference produced by subtracting the October 2009 terrestrial LiDAR data set from the May, 2010 data set. Covering 206 days of movement, this represents the greatest interval between surveys. The threshold for change detection is plus or minus 0.15 meters.

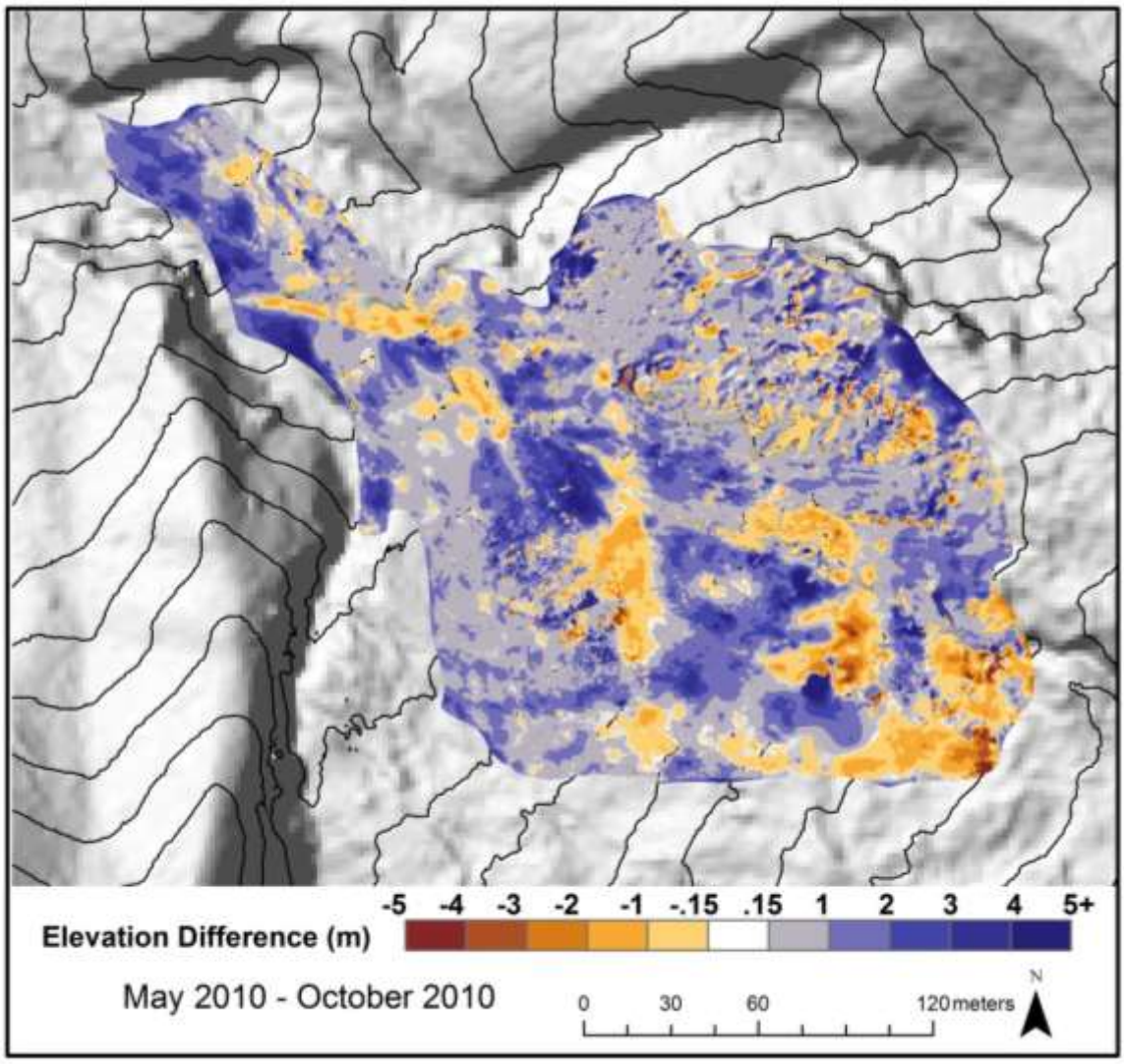

Figure 33 - DEM of difference produced by subtracting the May, 2010 terrestrial LiDAR data set from the October, 2010 data set, representing 152 days of movement. The threshold for change detection is plus or minus 0.15 meters.

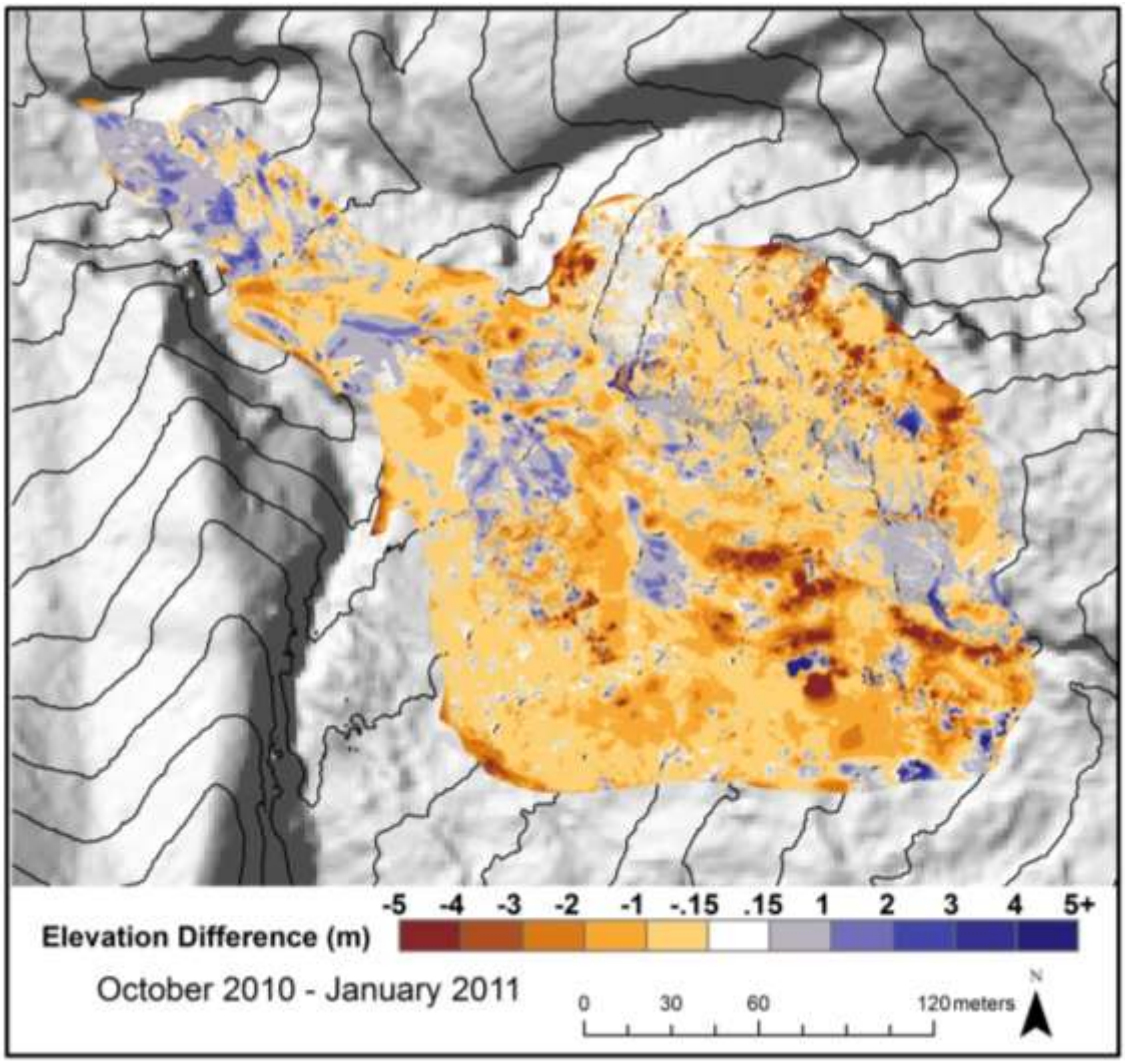

Figure 34 - DEM of difference produced by subtracting the October 2010 terrestrial LiDAR data set from the January, 2011 data set, representing 107 days of movement. The threshold for change detection is plus or minus 0.15 meters.

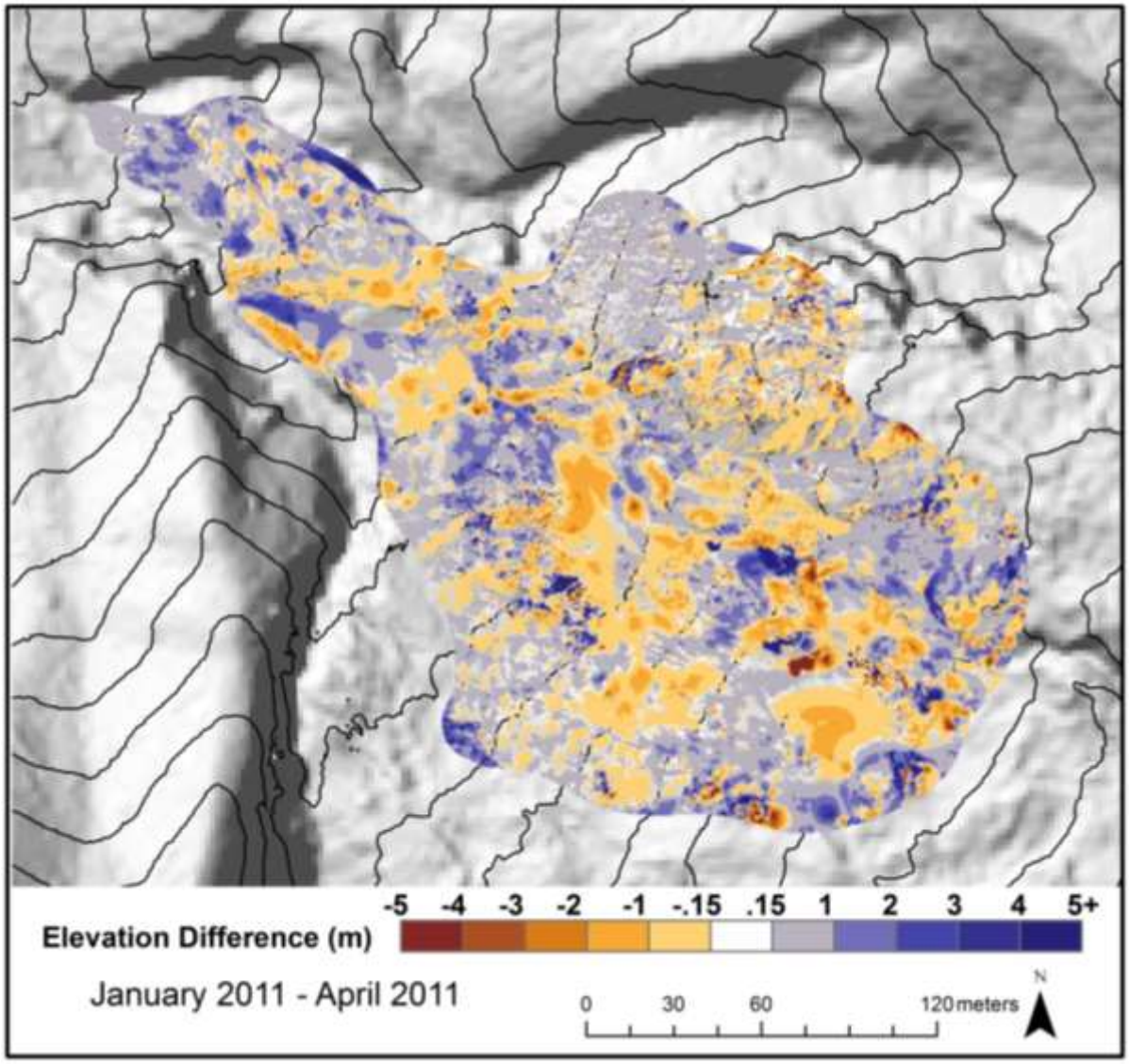

Figure 35 - DEM of difference produced by subtracting the January, 2011 terrestrial LiDAR data set from the April, 2011 data set. Covering 91 days of movement, this represents the shortest interval between surveys. The threshold for change detection is plus or minus 0.15 meters.

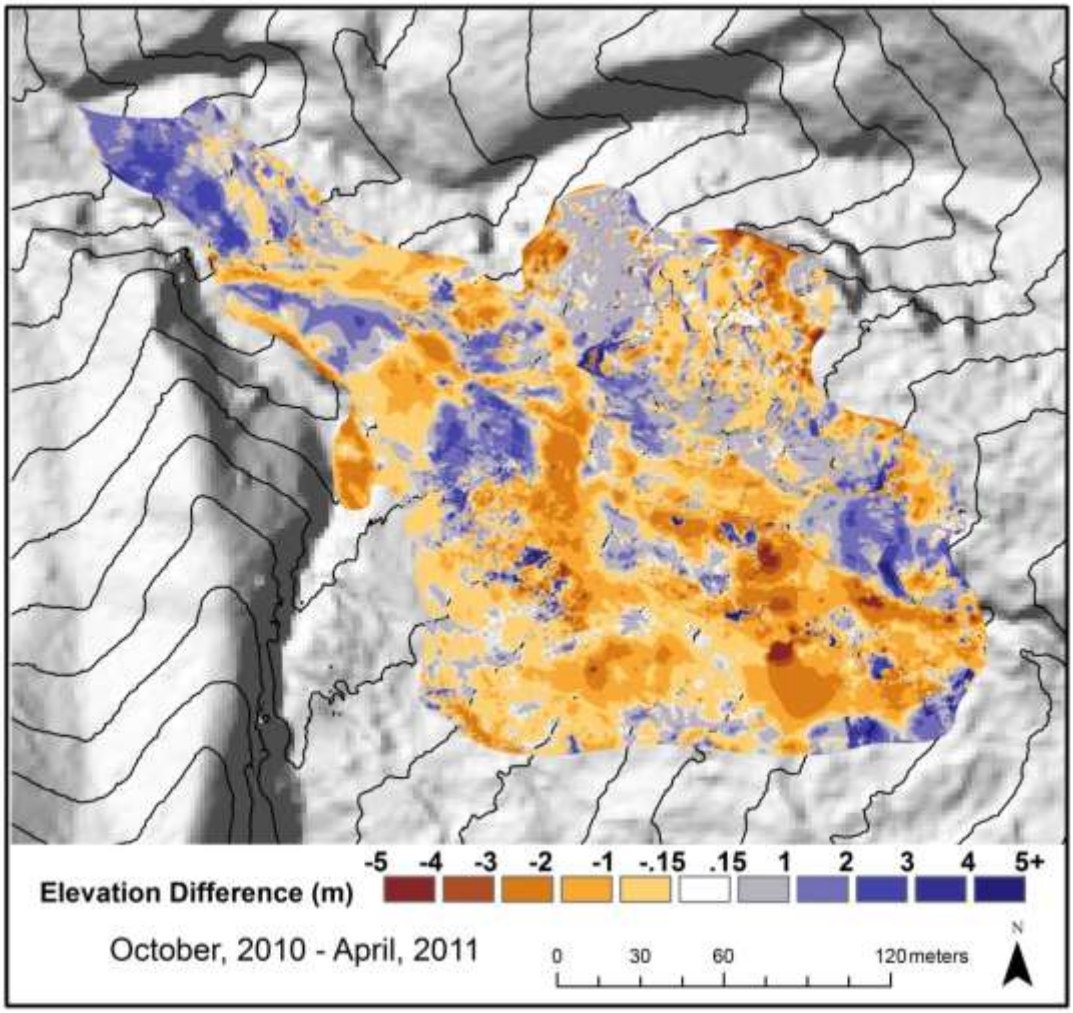

Figure 36 - DEM of difference produced by subtracting the October, 2010 terrestrial LiDAR data set from the April, 2011 data set. Covering 198 days of movement, this period captures similar seasonal weather patterns as the first interval, October, 2009 – May, 2010. The threshold for change detection is plus or minus 0.15 meters.

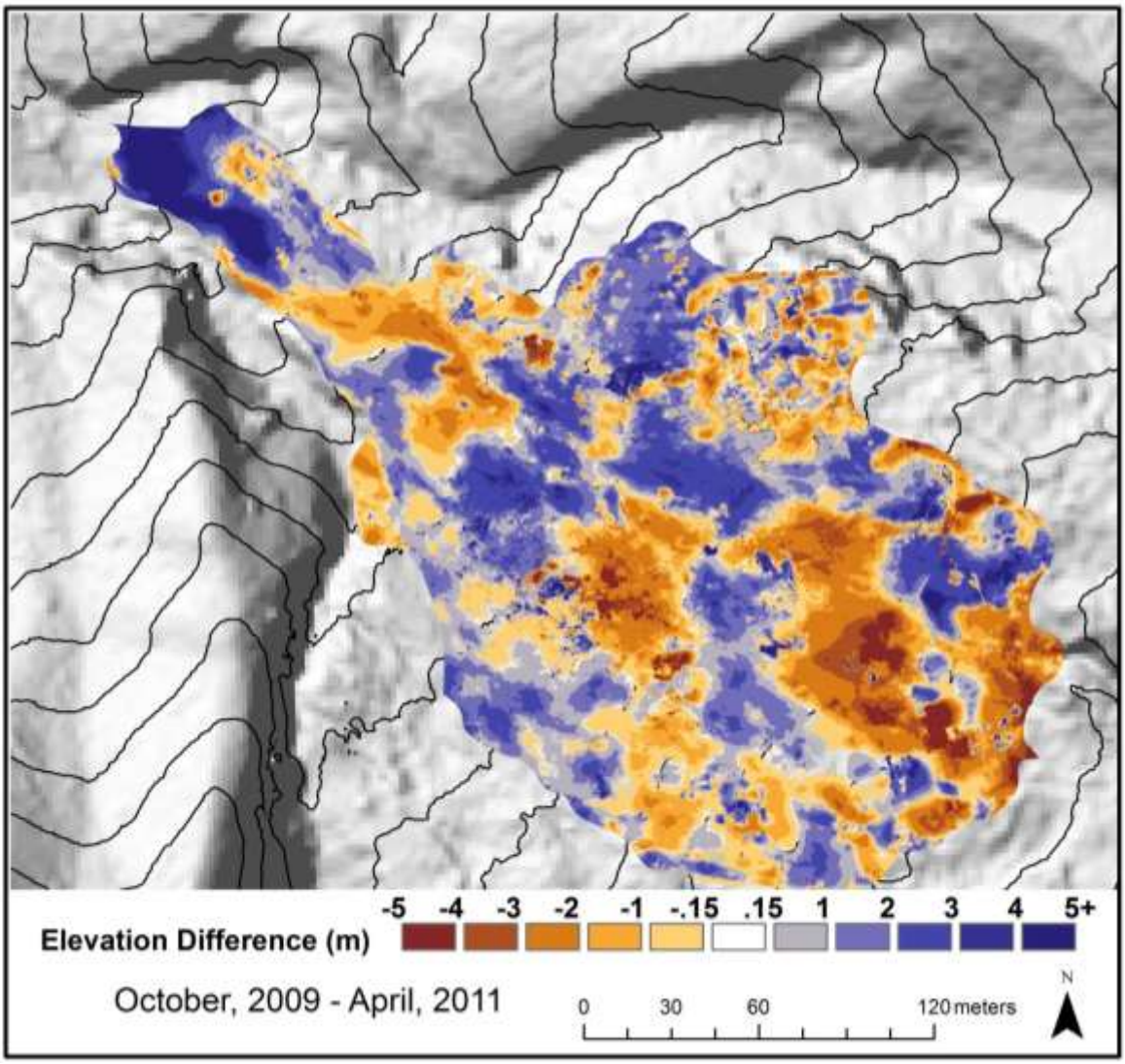

Figure 37 - DEM of difference produced by subtracting the October, 2009 terrestrial LiDAR dataset from the April, 2011 set. Covering 18 months, this represents the cumulative change recorded during the study. The threshold for change detection is plus or minus 0.15 meters.

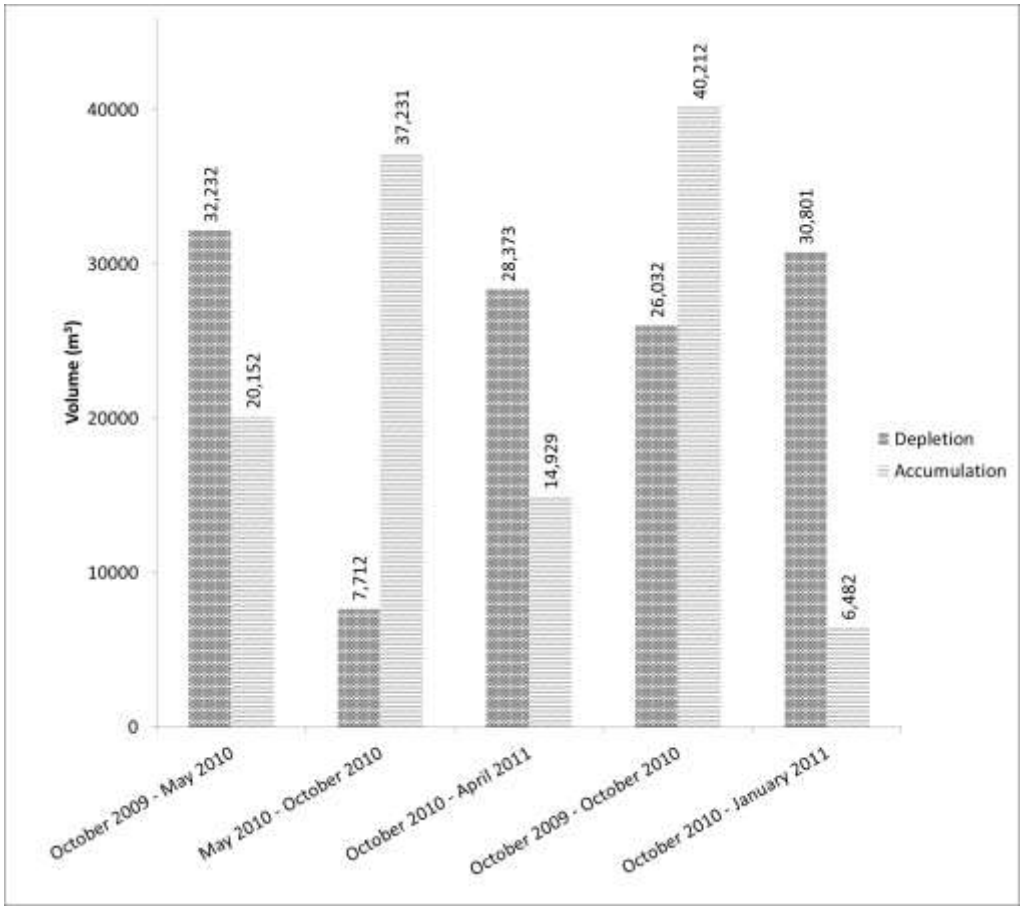

Figure 38 - Volumetric transfer associated with elevation changes at the toe of the Swift Creek landslide during the TLS campaign. The volumes (in cubic meters) were estimated with a cut and fill approach using DEMs derived from LiDAR data. While not a true measurement of mobilized volume, this approach provides a proxy to better understand the seasonal nature of material transport on the toe.

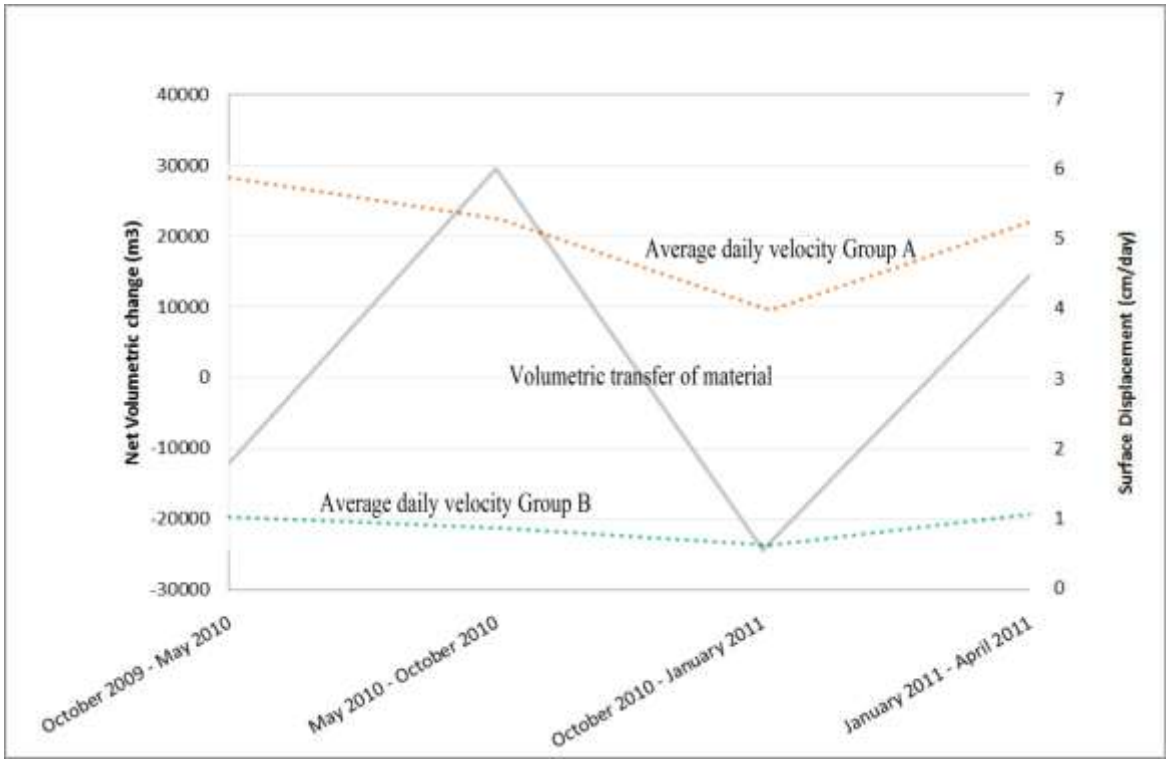

Figure 39 - The toe of the Swift Creek landslide exhibits seasonal changes in both movement patterns and material transport.

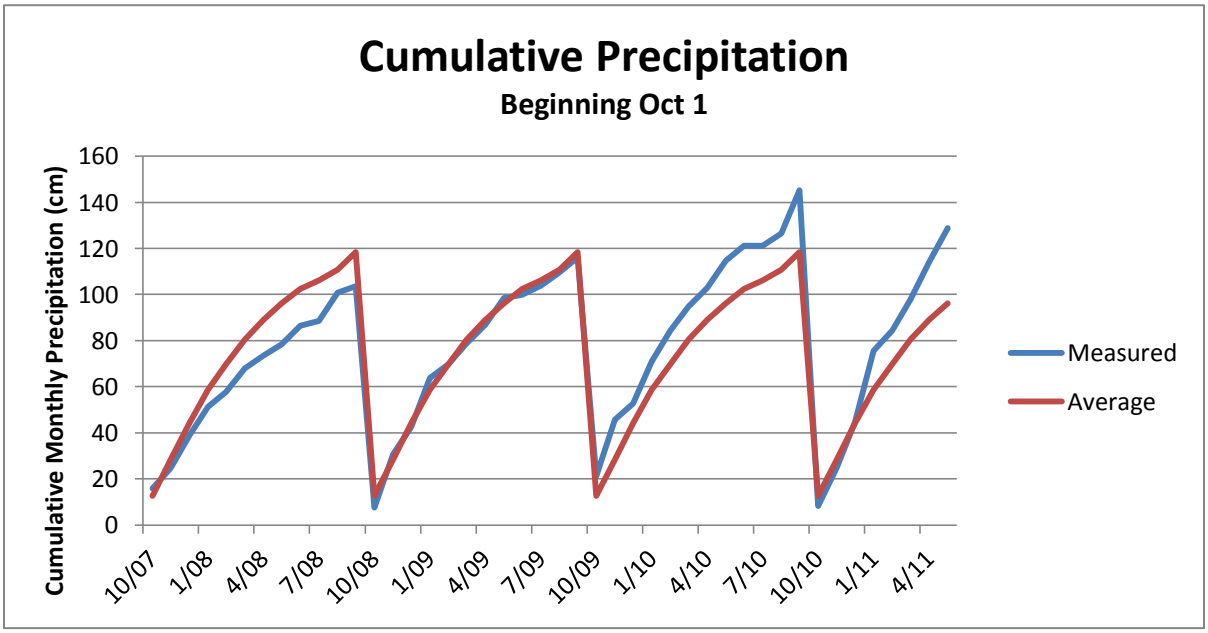

Figure 40 - Cumulative "normal" and actual monthly precipitation data (beginning October 1st) from a weather station located 9.4 km away from the study area.

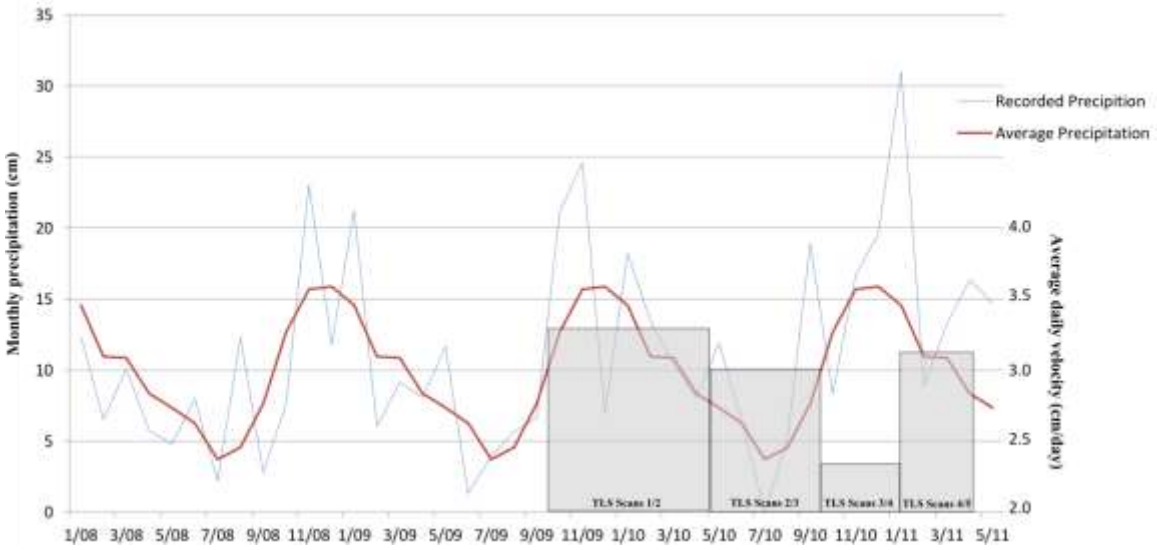

Figure 41 - Monthly precipitation data from nearby Clearbrook weather station is compared to average group velocities of the 25 boulders measured via ICP analysis.

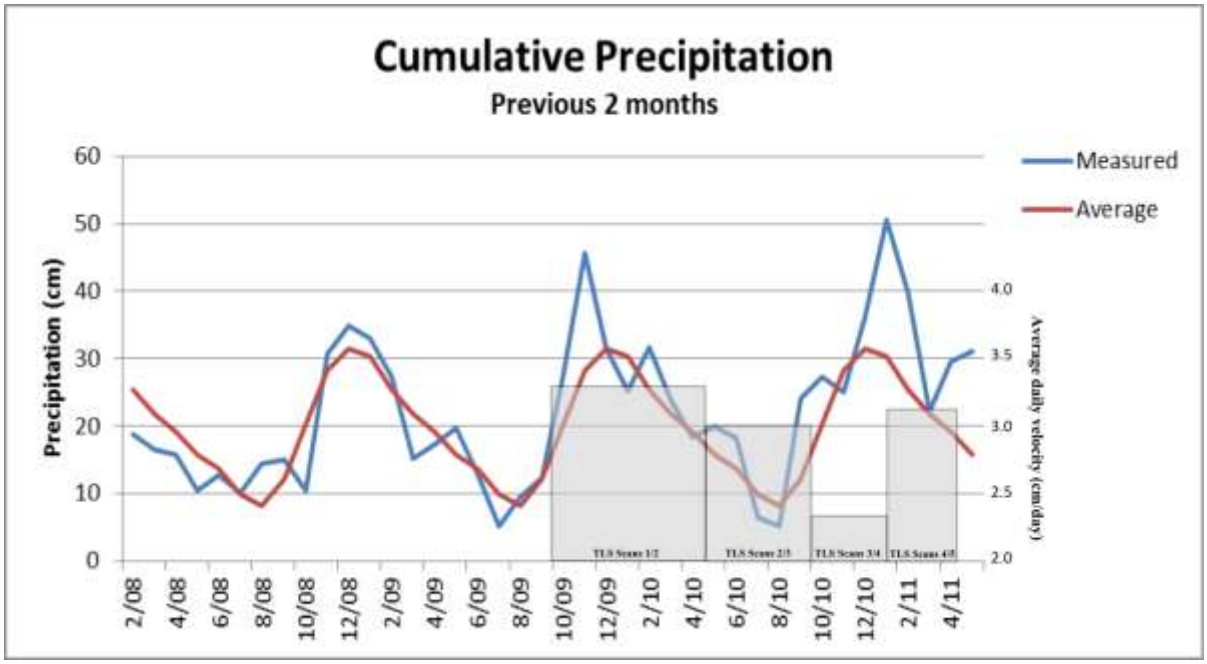

Figure 42 - Antecedent monthly precipitation over two months (~60 days) compared to average group velocities of the 25 boulders measured via ICP analysis.

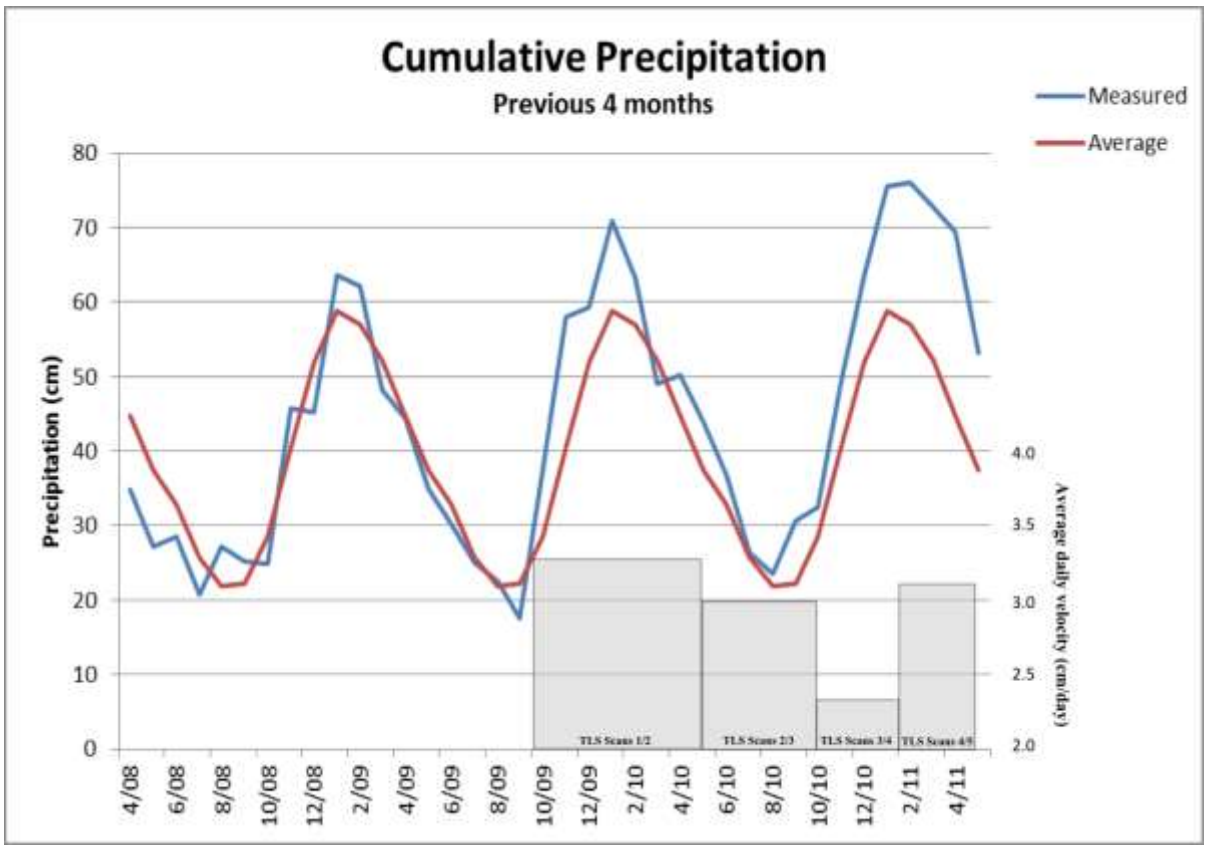

Figure 43 - Antecedent monthly precipitation over four months (~121 days) compared to average group velocities of the 25 boulders measured via ICP analysis.

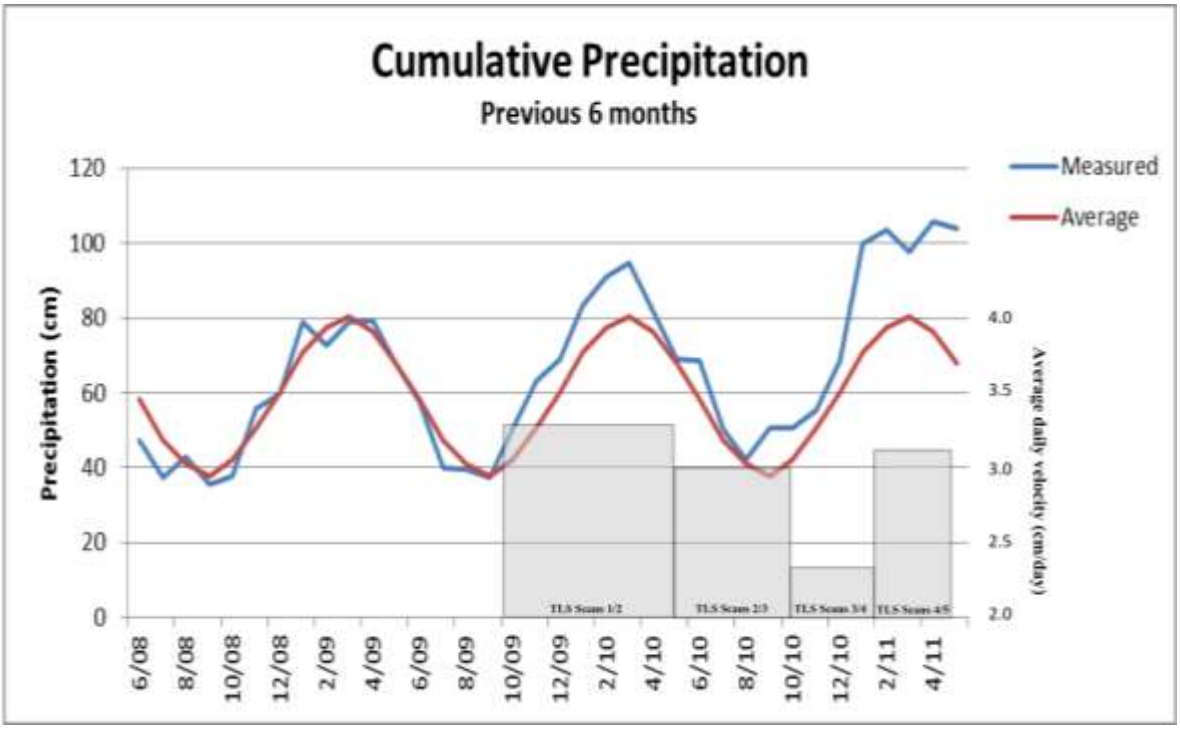

Figure 44 - Antecedent monthly precipitation over six months (~182 days) compared to average group velocities of the 25 boulders measured via ICP analysis.

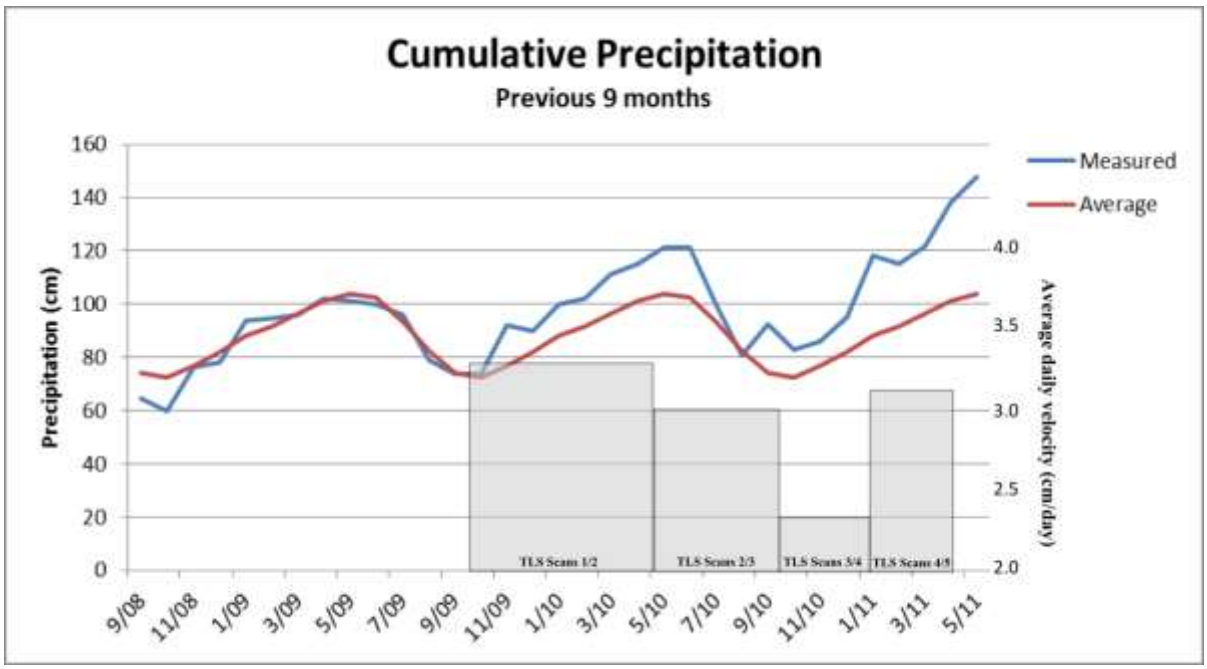

Figure 45 - Antecedent monthly precipitation over nine months (~243 days) compared to average group velocities of the 25 boulders measured via ICP analysis.

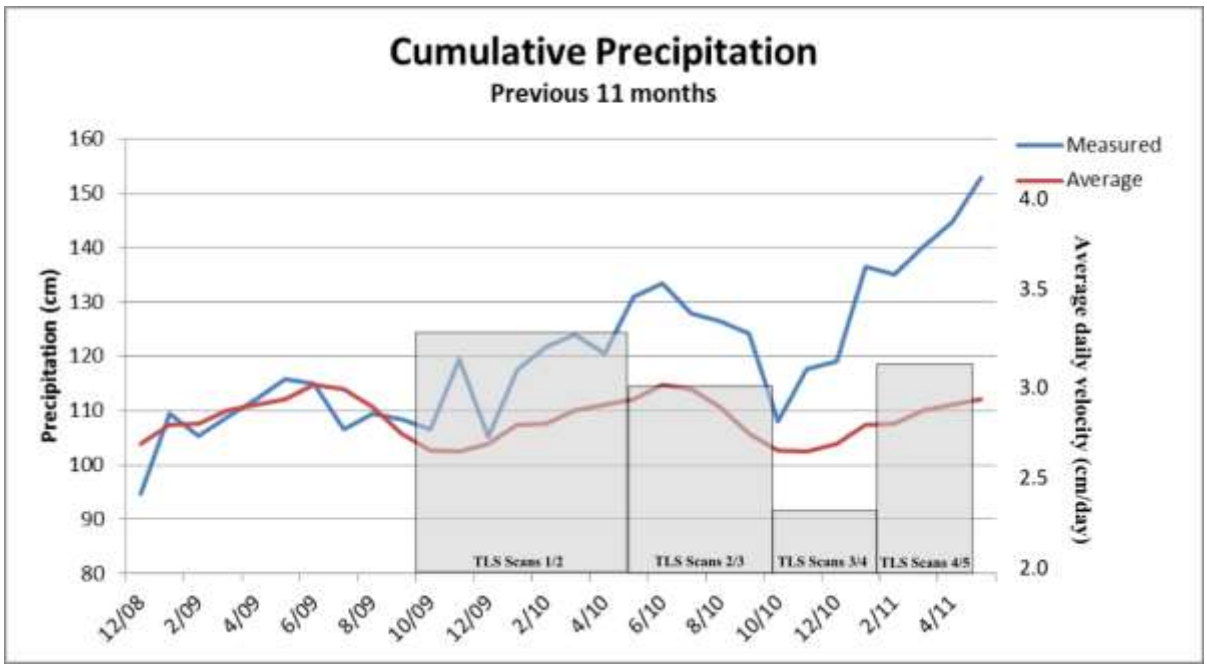

Figure 46 - Antecedent monthly precipitation over eleven months (~335 days) compared to average group velocities of the 25 boulders measured via ICP analysis.

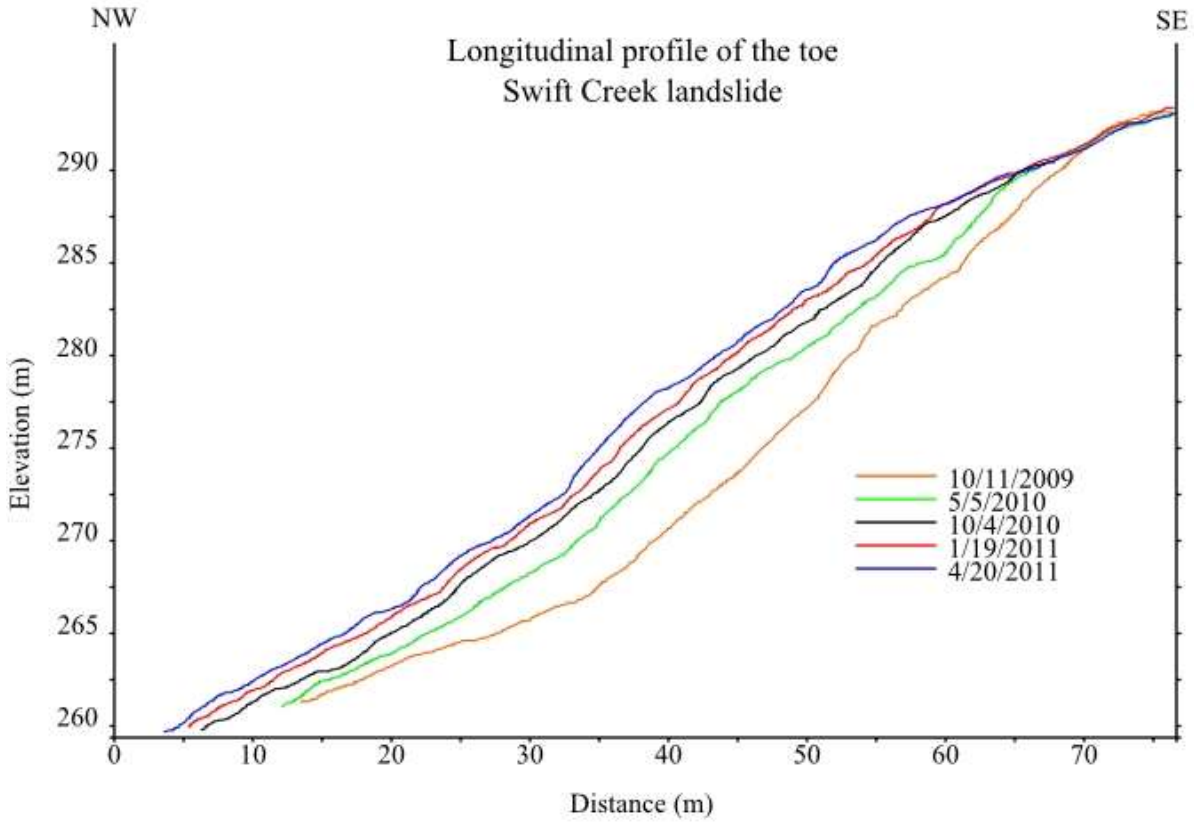

Figure 47 - A series of longitudinal profiles at the front (e.g., the tip) of the Swift Creek landslide. Note the advancing front and the convergence of the profiles above about 290 meters in elevation. Furthermore, there appears to be evidence of a change in slope morphology after October 2009; from somewhat concave to a more even slope.

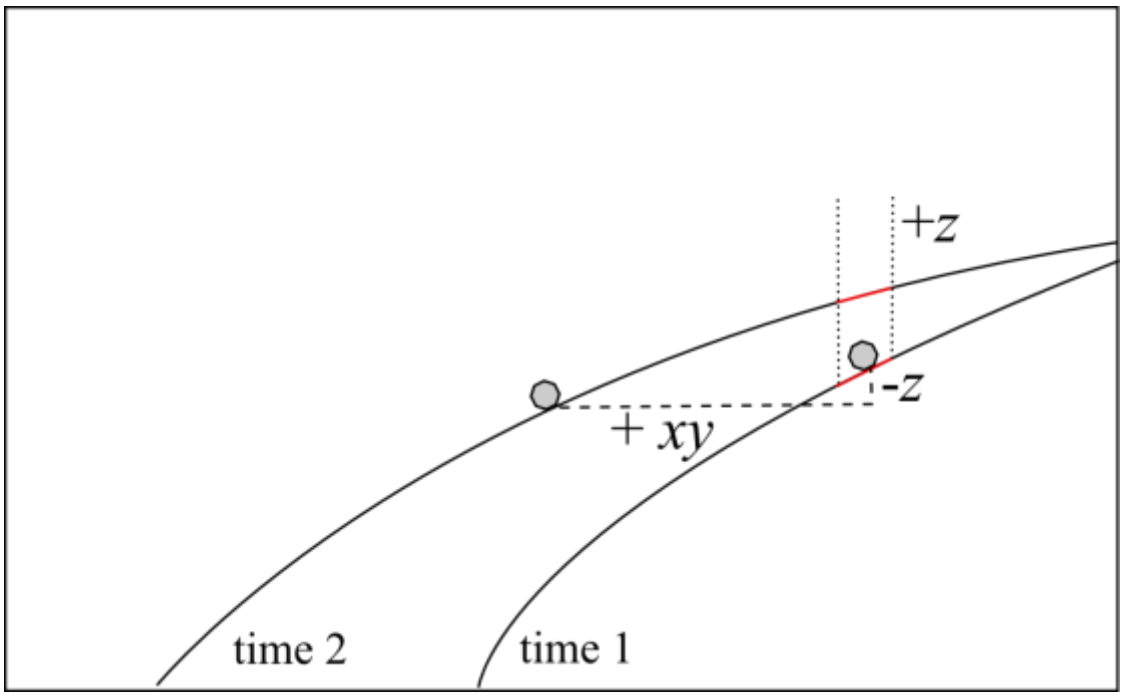

Figure 48 - A schematic diagram (not to scale) depicting how individual elements of the landslide can decrease in elevation in a zone that shows an apparent increase in surface elevation by means of an advancing toe.

Figure 49 - These two images were taken from similar locations in the creek bed below the landslide. The upper image was taken in February, 2007 and the lower image acquired in April, 2011. Together, they show that the creek level has not changed much despite significant advancement of the toe.

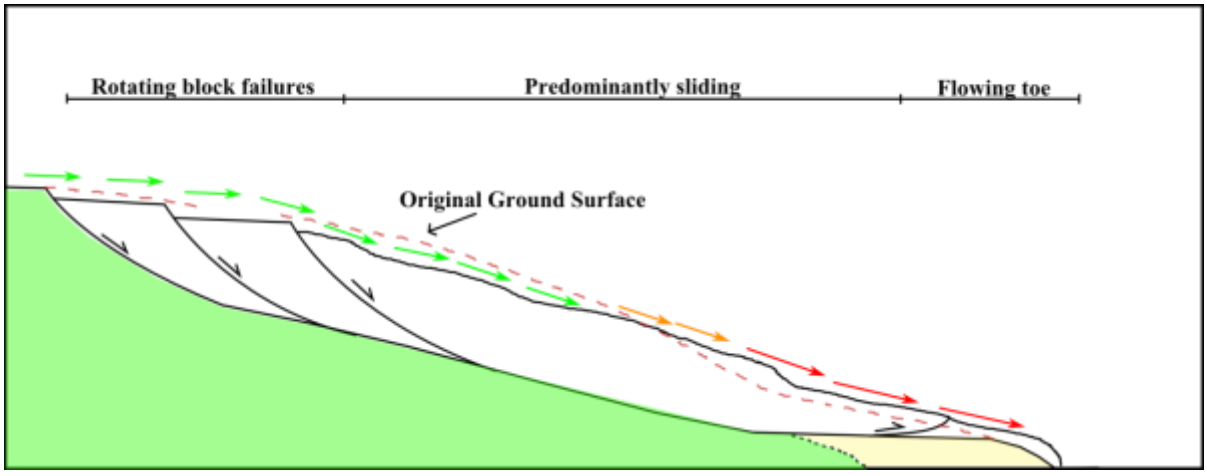

Figure 50 – A schematic cross section illustrating the overall movement patterns. The serpentinite (green) and conglomerate (tan) units are shown below the landslide. The displacement vectors on the surface are based on data obtained using PIV.

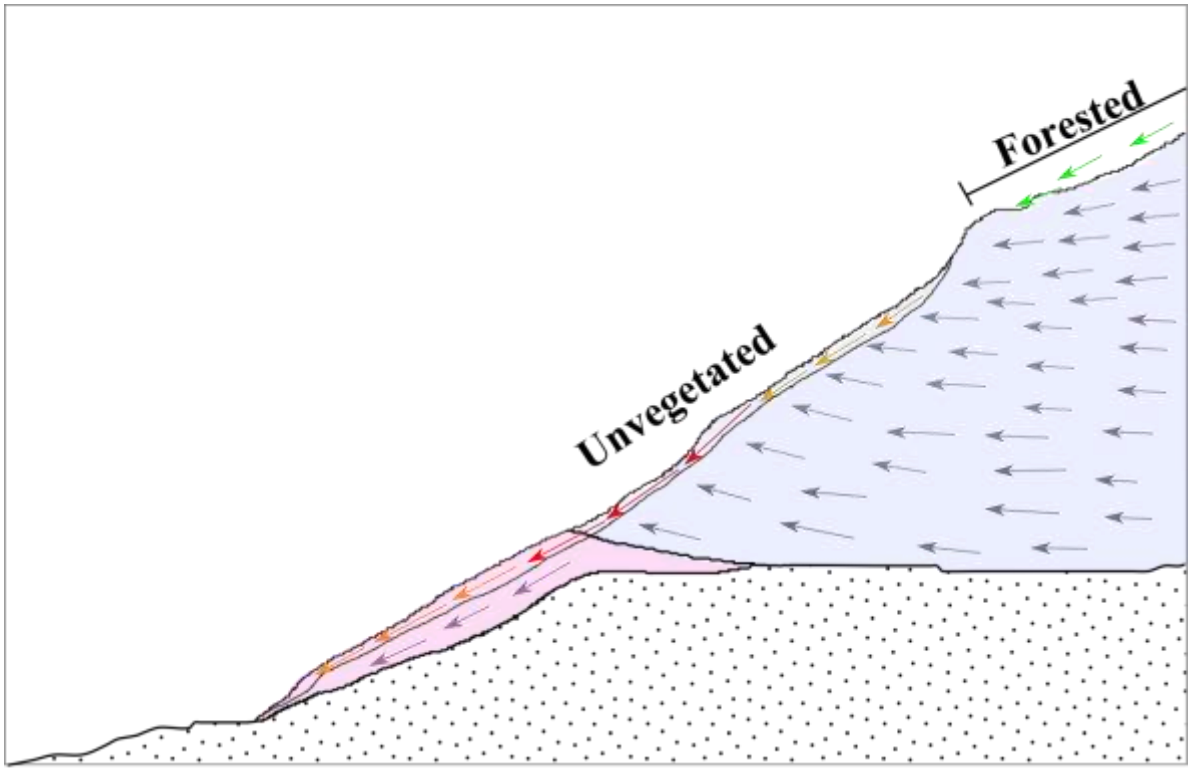

Figure 51 – A schematic illustration to explain the movement patterns observed at the Swift Creek landslide. The grey subsurface vectors are my interpretation. The thin veneer of material on the surface is flowing over the sliding mass (blue). The material at the base of the landslide (pink) is being overrun by the main mass of the landslide.

10.REFERENCES

Abellán, A., Vilaplana, J., and Martínez, J.: Application of a long-range Terrestrial Laser Scanner to a detailed rockfall study at Vall de Núria (Eastern Pyrenees, Spain), Engineering Geology, 88, 136-148, 2006.

Aryal, A., Brooks, B. A., Reid, M. E., Bawden, G. W., and Pawlak, G. R.: Displacement fields from point cloud data: Application of particle imaging velocimetry to landslide geodesy, Journal of Geophysical Research: Earth Surface (2003–2012), 117, 2012.

Baldo, M., Bicocchi, C., Chiocchini, U., Giordan, D., and Lollino, G.: LIDAR monitoring of mass wasting processes: The Radicofani landslide, Province of Siena, Central Italy, Geomorphology, 105, 193-201, 2009.

Bayer, T. M. and Linneman, S. L.: The nature and transport of the fine-grained component of Swift Creek Landslide, Northwest Washington, Earth Surface Processes and Landforms, 36, 2011.

Bremer, M. and Sass, O.: Combining airborne and terrestrial laser scanning for quantifying erosion and deposition by a debris flow event, Geomorphology, 138, 49-60, 2012.

Brückl, E., Brunner, F., and Kraus, K.: Kinematics of a deep‐seated landslide derived from photogrammetric, GPS and geophysical data, Engineering Geology, 88, 149-159, 2006.

Coe, J. A., Ellis, W. L., Godt, J. W., Savage, W. Z., Savage, J. E., Michael, J. A., Kibler, J. D., Powers, P. S., Lidke, D. J., and Debray, S.: Seasonal movement of the Slumgullion landslide determined from Global Positioning System surveys and field instrumentation, July 1998-March 2002, Engineering Geology, 68, 67-101, 2003.

Corsini, A., Pasuto, A., Soldati, M., and Zannoni, A.: Field monitoring of the Corvara landslide (Dolomites, Italy) and its relevance for hazard assessment, Geomorphology, 66, 149-165, 2005.

Corsini, A., Borgatti, L., Cervi, F., Dahne, A., Ronchetti, F., and Sterzai, P.: Estimating mass-wasting processes in active earth slides–earth flows with time-series of High-Resolution DEMs from photogrammetry and airborne LiDAR, Nat. Hazards Earth Syst. Sci, 9, 433-439, 2009.

Cruden, D. M. and Varnes, D. J.: Landslides: Investigation and Mitigation, Special Report 247, edited by: Board, T. R., Chapter 3, pp. 36-75, 1996.

Daehne, A. and Corsini, A.: Kinematics of active earthflows revealed by digital image correlation and DEM subtraction techniques applied to multitemporal LiDAR data, Earth Surface Processes and Landforms, 38, 640-654, 2012.

Derron, M. and Jaboyedoff, M.: LIDAR and DEM techniques for landslides monitoring and characterization, Natural Hazards and Earth System Science, 10, 1877-1879, 2010.

Dewitte, O. and Demoulin, A.: Morphometry and kinematics of landslides inferred from precise DTMs in West Belgium, Natural Hazards and Earth System Science, 5, 259-265, 2005.

Dragovich, J. D., Norman, D. K., Haugerud, R. A., and Pringle, P. T.: Geologic map and interpreted geologic history of the Kendall and Deming 7.5- minute quadrangles, western Whatcom County, Washington, Open File Report 97-92, 39 p., 1997.

Glenn, N. F., Streutker, D. R., Chadwick, D. J., Thackray, G. D., and Dorsch, S. J.: Analysis of LiDAR-derived topographic information for characterizing and differentiating landslide morphology and activity, Geomorphology, 73, 131-148, 2006.

Hungr, O., Evans, S., Bovis, M., and Hutchinson, J.: A review of the classification of landslides of the flow type, Environmental & Engineering Geoscience, 7, 221-238, 2001.

Iverson, R. M. and Major, J. J.: Rainfall, ground-water flow, and seasonal movement at Minor Creek landslide, northwestern California: Physical interpretation of empirical relations, Geological Society of America Bulletin, 99, 579-594, 1987.

Jaboyedoff, M., Choffet, M., Derron, M.-H., Horton, P., Loye, A., Longchamp, C., Mazotti, B., Michoud, C., and Pedrazzini, A.: Preliminary Slope Mass Movement Susceptibility Mapping Using DEM and LiDAR DEM, in: Terrigenous Mass Movements, Springer, 109-170, 2012.

Kasperski, J., Delacourt, C., Allemand, P., Potherat, P., Jaud, M., and Varrel, E.: Application of a Terrestrial Laser Scanner (TLS) to the Study of the Séchilienne Landslide (Isère, France), Remote Sensing, 2, 2785-2802, 2010.

Keefer, D. K. and Johnson, A. M.: Earthflows-Morphology, mobilization and movement., U.S Geological Survey Proffesional Paper, 1264, 1983.

Lichti, D., Gordon, S., and Stewart, M.: Ground-based laser scanners: operation, systems and applications, Geomatica, 56, 21-33, 2002.

Lichti, D.D., Gordon, S.J., and Stewart, M.P.: Angular resolution of terrestrial laser scanners, Photogrammetric Record, 21, 141-160, 2006.

Linneman, S. R. and Pittman, P.: The Source of Asbestiform Chrysotile at Swift Creek WA: Geology, Mineralogy and Sediment Transport, Portland GSA Annual Meeting 18-21 October 2009, Session No. 274., 2009.

Mackey, B. H. and Roering, J. J.: Sediment yield, spatial characteristics, and the long-term evolution of active earthflows determined from airborne LiDAR and historical aerial photographs, Eel River, California, Geological Society of America Bulletin, 123, 1560-1576, 2011.

Malet, J.-P., Van Asch, T. W., Van Beek, R., and Maquaire, O.: Forecasting the behaviour of complex landslides with a spatially distributed hydrological model, Natural Hazards and Earth System Science, 5, 71-85, 2005.

McKenzie-Johnson, A.: Kinematics of the Swift Creek landslide, Northwest Washington, Masters Thesis, Western Washington University, 2004.

Miller, M. M., Johnson, D. J., Rubin, C. M., Dragert, H., Wang, K., Qamar, A., and Goldfinger, C.: GPS determination of along strike variation in Cascadia margin kinematics: Implications for relative plate motion, subduction zone coupling, and permanent deformation, Tectonics, 20, 161-176, 2001.

Monserrat, O. and Crosetto, M.: Deformation measurement using terrestrial laser scanning data and least squares 3D surface matching, ISPRS Journal of Photogrammetry and Remote Sensing, 63, 142-154, 2008.

Oppikofer, T., Jaboyedoff, M., Blikra, L., Derron, M.-H., and Metzger, R.: Characterization and monitoring of the Aknes rockslide using terrestrial laser scanning, Natural Hazards and Earth System Sciences, 9, 1003-1019, 2009.

Petley, D. N. and Allison, R. J.: The mechanics of deep-seated landslides, Earth Surface Processes and Landforms, 22, 747-758, 1997.

Prokop, A. and Panholzer, H.: Assessing the capability of terrestrial laser scanning for monitoring slow moving landslides, Nat. Hazards Earth Syst. Sci, 9, 1921-1928, 2009.

Raffel, M., Willert, C. E., Wereley, S. T., and Kompenhans, J.: Particle image velocimetry: a practical guide, Springer, 2007.

Savage, W. Z. and Baum, R. L.: Instability of steep slopes, in: Debris Flow Hazards and Related Phenomena, Praxis Publishing House and Springer-Verlag, Chichester, U.K., 53-79, 2005.

Schreier, H. and Lavkulich, L.: Spatial and Historic Changes in Sediments in the Sumas River Watershed Affected by an Asbestos Rich Landslide 1993-2009., 2007.

Schwab, M., Rieke-Zapp, D., Schneider, H., Liniger, M., and Schlunegger, F.: Landsliding and sediment flux in the Central Swiss Alps: A photogrammetric study of the Schimbrig landslide, Entlebuch, Geomorphology, 97, 392-406, 2008.

Teza, G., Galgaro, A., Zaltron, N., and Genevois, R.: Terrestrial laser scanner to detect landslide displacement fields: a new approach, International Journal of Remote Sensing, 28, 3425-3446, 2007.

Verdonck, D.: Contemporary vertical crustal deformation in Cascadia, Tectonophysics, 417, 221-230, 2006.

Wawrzyniew, T., McFadden, L.D., Ellwein, A., Meyer, G., Scuderi, L., McAuliffe, J., and Fawcett, P.: Chronotopographic analysis directly from point-cloud data: A method for detecting small, seasonal hillslope change, Black Mesa Escarpment, NE Arizona, Geosphere, 3, 550-567, 2007.

Whatcom County Public Works: Swift Creek Sediment Action Plan, 2012.

White, D., Take, W., and Bolton, M.: Soil deformation measurement using particle image velocimetry (PIV) and photogrammetry, Geotechnique, 53, 619-631, 2003.

11. APPENDIX

11.1. TLS Data Processing

This section describes the methodology I used to process raw terrestrial LiDAR data into georeferenced data sets. The data was processed using a combination of programs developed by the manufacturer of the TLS (Optech, Inc) and an associated third-party software developer (Innovmetric).

11.1.1. Data pre-processing

The parser application (by Optech) is designed to convert raw scan data into a 3D digitized dataset (in several formats) that can be imported into various platforms. The parser application also includes basic data filtering (by range or intensity). The output I used was an 8-bit .pif format intended to be used with the Innovmetric Polyworks software suite designed for the Optech Ilris 3D.

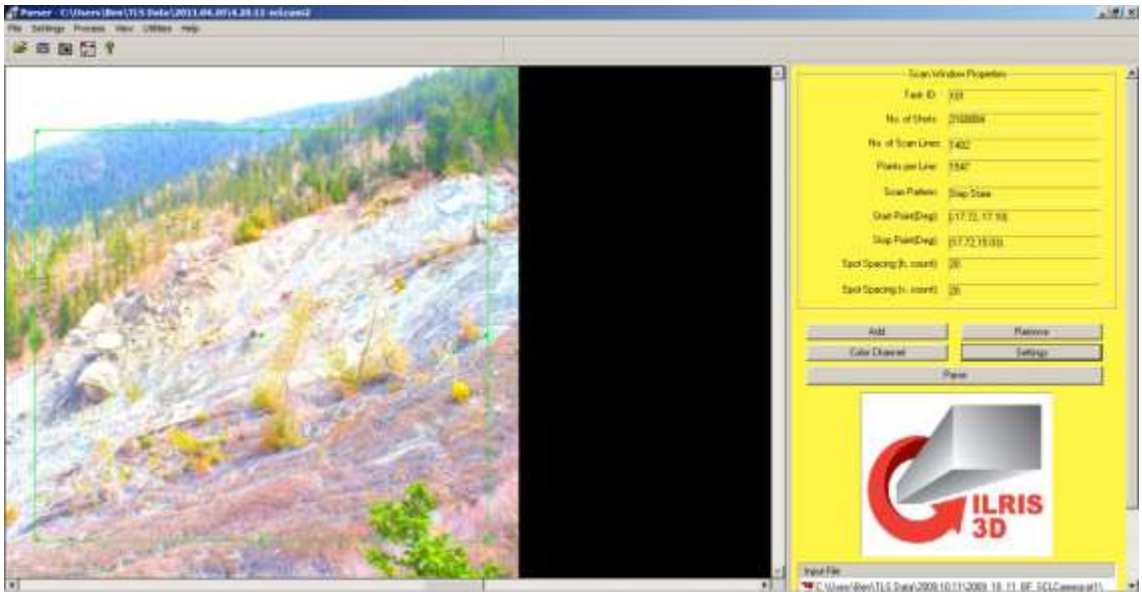

I applied a scale intensity range of 20m. This was chosen through trial-and-error. The shortest distance was chosen because it best scaled the intensity of the pixels in the foreground and background. I also applied a maximum distance range "gate" that varied for each scan. I chose a max distance that retained all of the desired data points over the toe and removed the more distant points that were not of interest in this study. This was done to reduce the number of data points to make subsequent processing more efficient. Lastly I chose to move the origin of the coordinate system of each scan to the "bolt hole" to allow for future georeferencing.

For each scan processed in the parser application, a .pif point-cloud file was produced. In addition to the point data, a .txt parsing log was produced for each parsed scan file that included key details for each dataset such as the point spacing and range.

11.1.2. Alignment of contemporaneous individual scans

Polyworks IMAlign (by Innovemtric) was first used to align scans acquired at the same time. The parsed scan files in .pif format were imported into IMAlign following the instructions in the software manual. The digitized datasets were imported and interpolated to a mesh by IMAlign using the parameters found in the parsing log created for each parsed file. Upon importing each file, I chose to subdivide each file by range (to create smaller scans or subscans) according to the manual. To retain the most data points, I chose a max angle of 89.99 and opted to not subsample the data. I chose the lowest subdivision angle (10) because it produced a better mesh by creating more subscans.

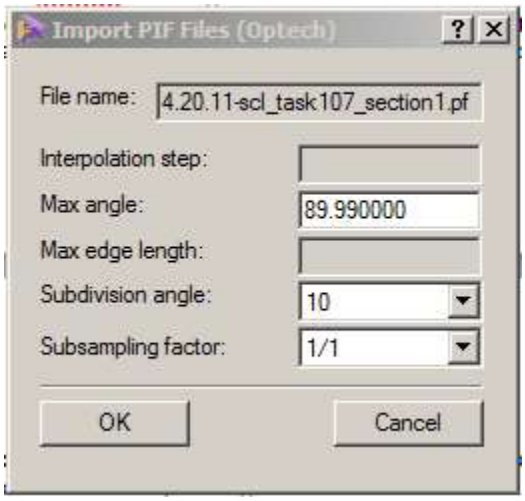

After the initial import, more parameters were defined to produce an interpolated mesh. I chose the maximum number of ranges (5), an interpolation step of zero and a max edge length of 10 (meters). The additional base parameters were copied from the parsing log.

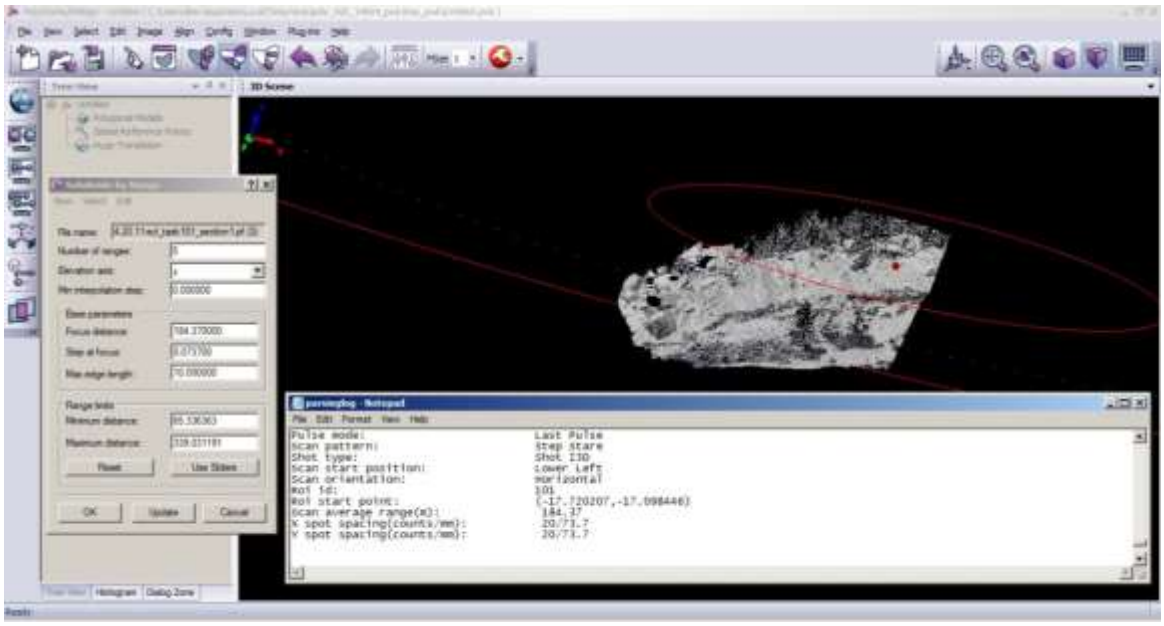

After importing two scan files, the second scan file was aligned to the first using the *align N Point pairs* tool in IMAlign.

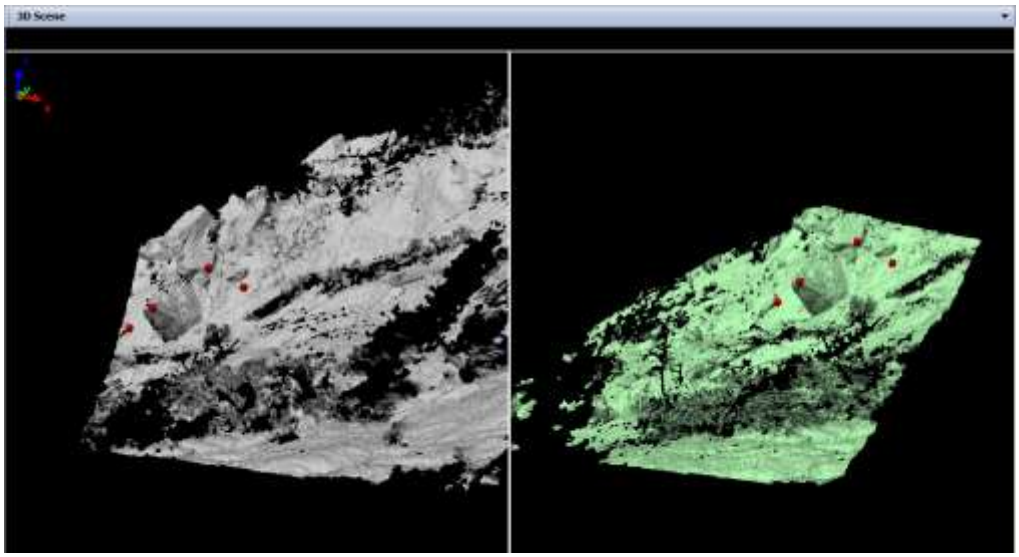

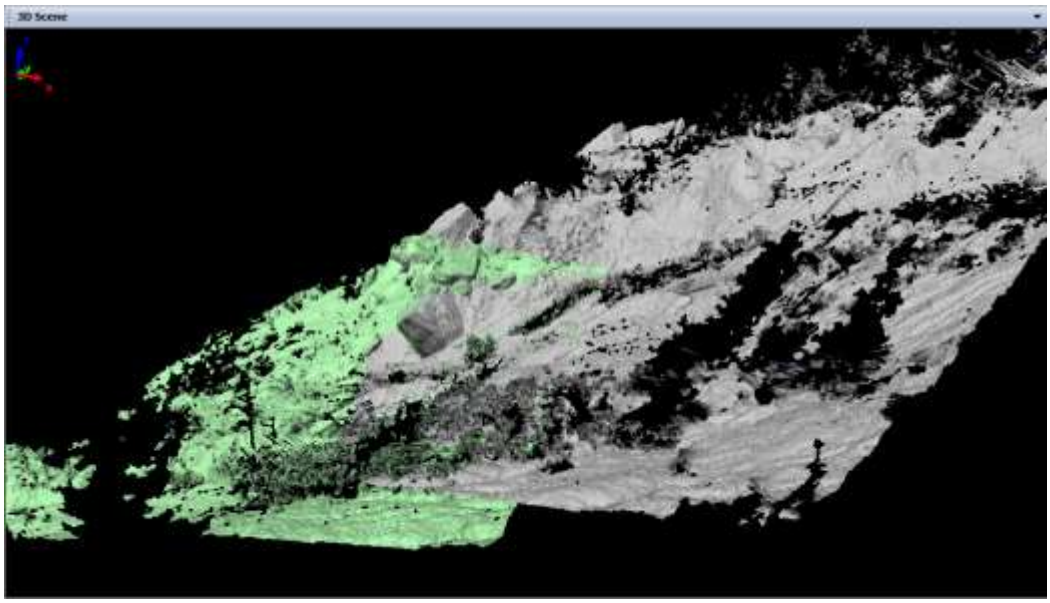

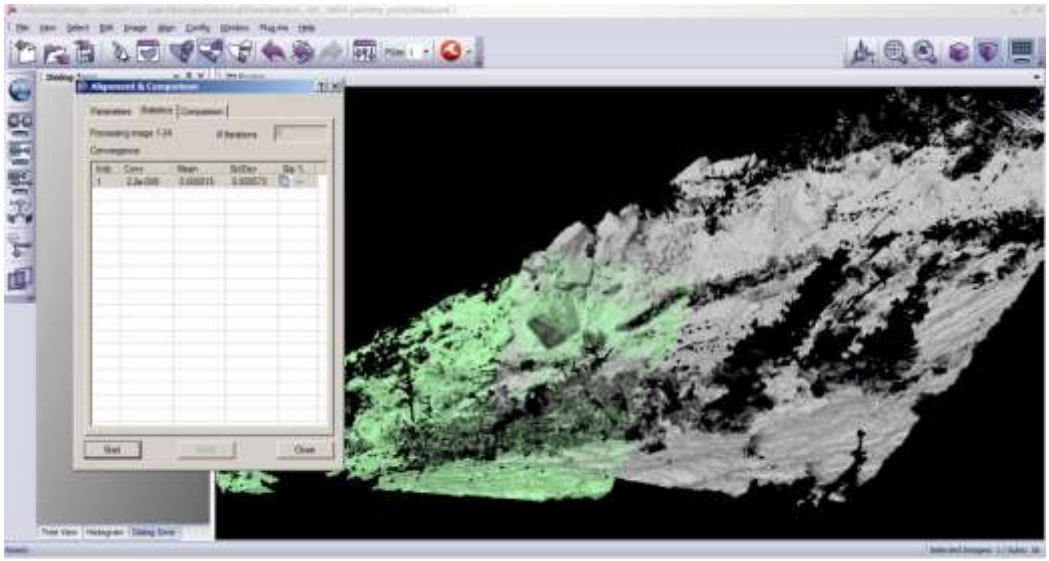

Once the two scans were successfully aligned, the first image was locked so that its position would not be altered during subsequent alignments. The remaining scan files were then imported one at a time following the same procedure

Following the alignment of the last scan file, all but the first scan files are unlocked. A final best-fit alignment was then carried out because some scans overlapped multiple scans.

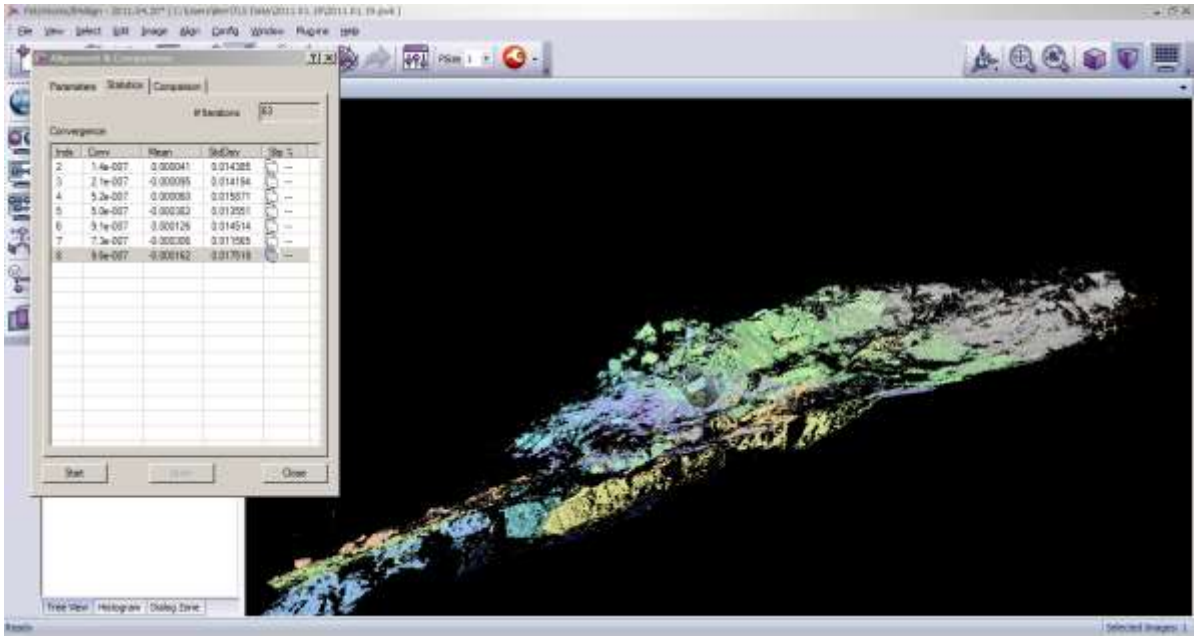

11.1.3. Georeferencing using IMInspect

The method to georeferencing assembled point clouds using IMInspect follows this work flow:

- Identify and create *points* from targets in the point cloud whose coordinates are known

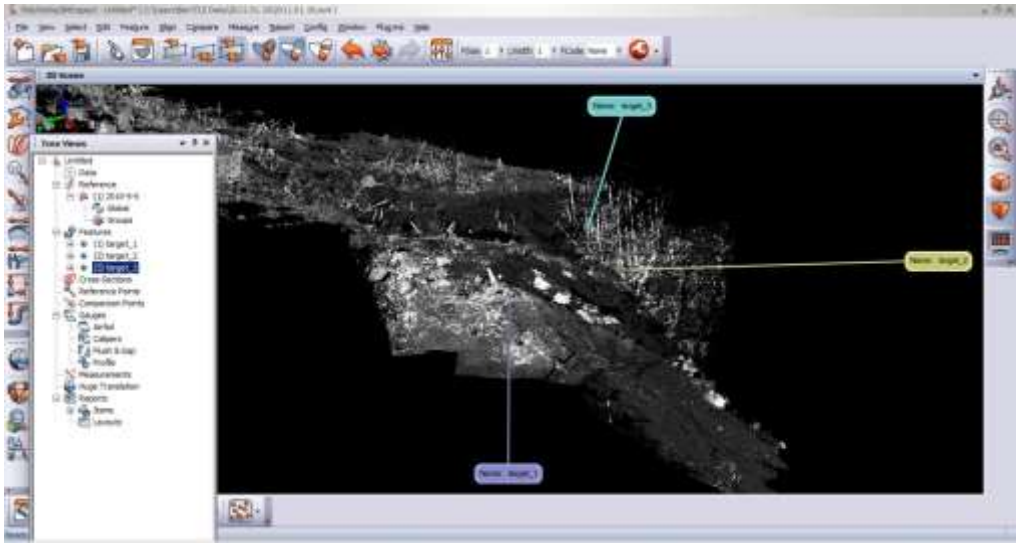

- Preform a hugh translation of the point cloud to transform the coordinate system (0,0,0) closer to the actual position by entering the coordinates of a point in the general area
- Import a point file that contains the coordinates (x,y,z) of three or more points measured in the field

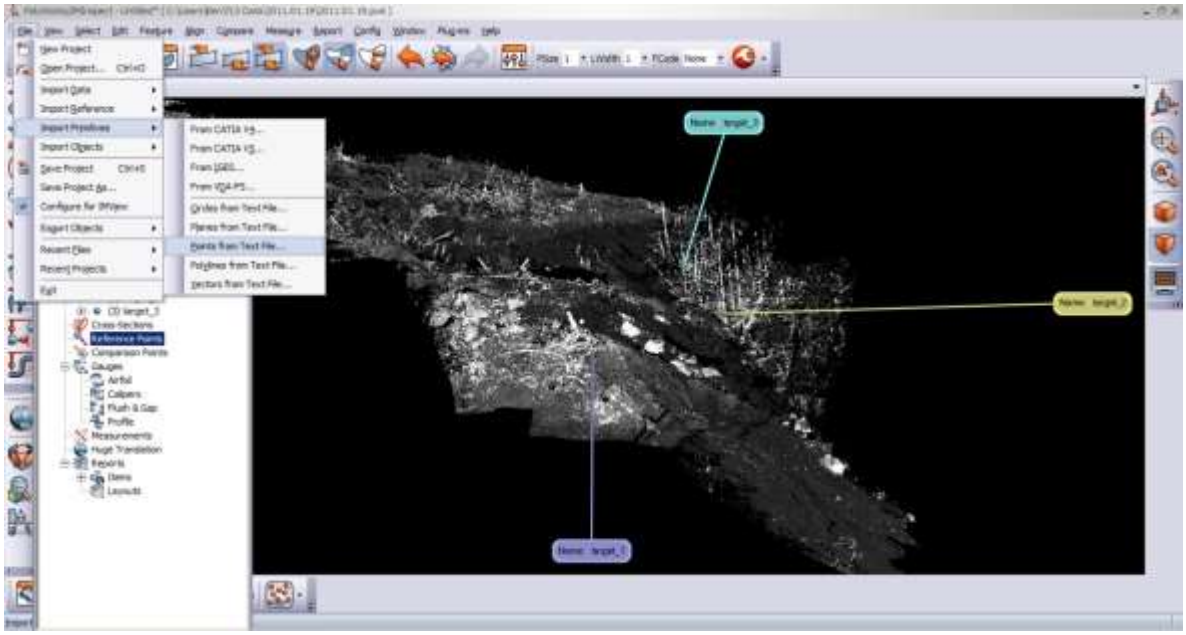

- Align the points in the point cloud with the imported points using *Align N Pairs of Center Points*

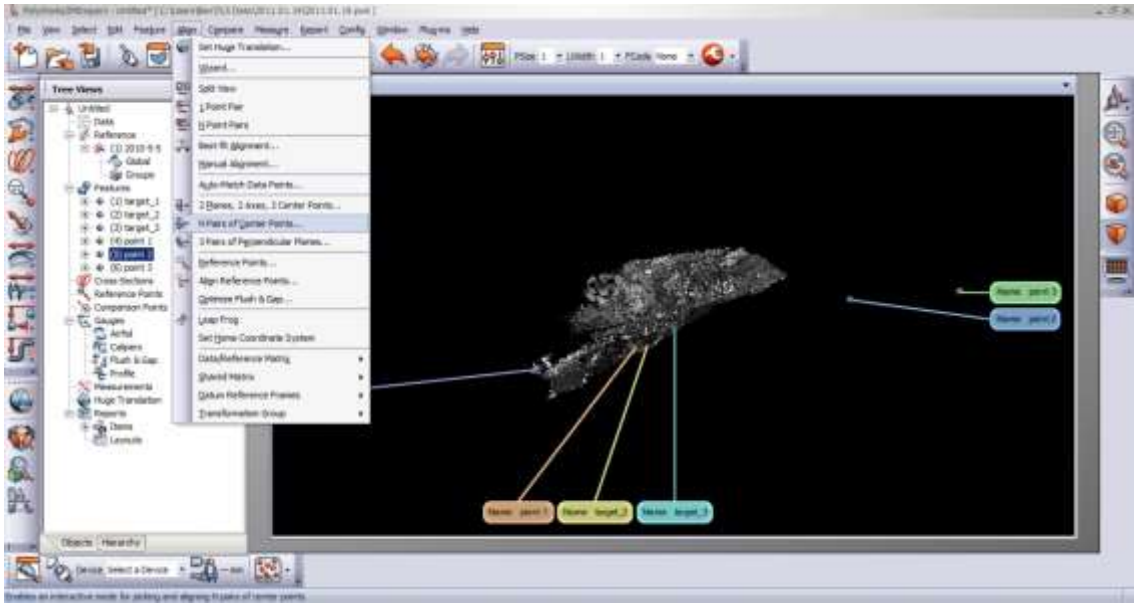

Georeferencing Report

Auto-Match Report of 5/5/2010_TLS

Images transformed by auto-match alignment:

- cam1
- cam2
- cam3
- creek
- South1
- South2
- North1
- North2

Number of matched pairs: 3

Mean deviation: 0.024430409

Match Pair # 1

Point-to-Point Match				
	X	Y	Z	Total
Source Point	554878.77	5417822.4	284.12655	
Destination Point	554878.77	5417822.5	284.13	
Deviation	0.0029670715	0.010802482	0.0034478748	0.011721134

Source Point				
Point Name	X	Y	Z	Distance to Dest. Point

RP 7 1	-182.67348	70.609703	-174.73668	5446111.3

Destination Point			
Point Name	X	Y	Z
Tree	554878.77	5417822.5	284.13

Match Pair # 2

Point-to-Point Match				
	X	Y	Z	Total
Source Point	554925.53	5417709	318.28693	

Destination Point	554925.53	5417709	318.29	
Deviation	0.0014382893	0.024840361	0.0030658056	0.025070129

Source Point				
Point Name	X	Y	Z	Distance to Dest. Point
RP 8 1	-86.36129	65.607193	-91.578674	5445998.4

Destination Point			
Point Name	X	Y	Z
upper	554925.53	5417709	318.29

Match Pair # 3

Point-to-Point Match				
	X	Y	Z	Total
Source Point	554905.18	5417735.5	301.79651	
Destination Point	554905.18	5417735.4	301.79	
Deviation	-0.0044053604	-0.035642842	-0.0065136804	0.036499964

Source Point				
Point Name	X	Y	Z	Distance to Dest.

				Point
RP 7 2	-107.89528	59.409485	-121.29942	5446031

Destination Point			
Point Name	X	Y	Z
lower	554905.18	5417735.4	301.79

- Export the alignment matrix of the aligned data set

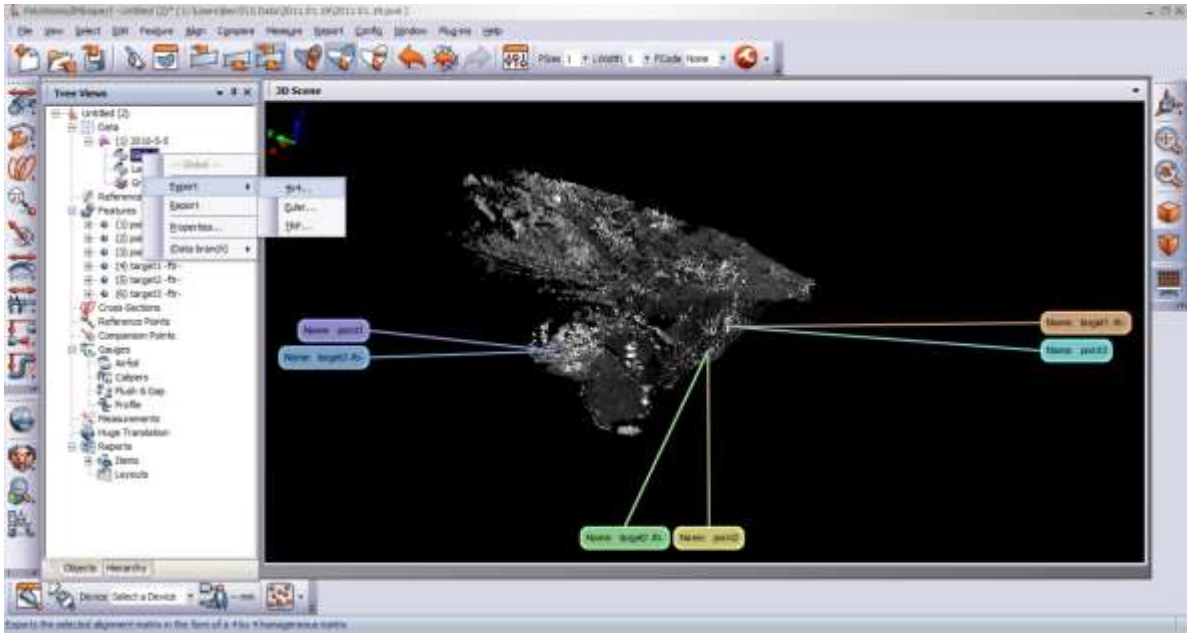

11.2. Georeferencing the remaining datasets

The remaining four assembled data sets also required georeferencing. Instead of following the IMInspect georeferencing method, I chose to align the stable areas in each dataset to the previously georeferenced (May, 2010) data set. This was done because the uncertainty

associated with best-fit alignments is lower than using the above method involving *Align N Pairs of Center Points* which uses three data points for georeferencing where as many thousands of points are used in the *best-fit alignment*.

The following workflow describes the process by which the point clouds were aligned to the georeferenced data set:

- Using IMInspect, I imported the assembled point clouds (saved as IMAlign projects)
- I first imported the non-georeferenced data sets as *data* and the previously georeferenced data set as *reference*
- I aligned the *reference* data set using the alignment matrix from the previous georeferencing process

- I then removed the unstable terrain in the datasets by deleting the selected data points (including the previously georeferenced data set)

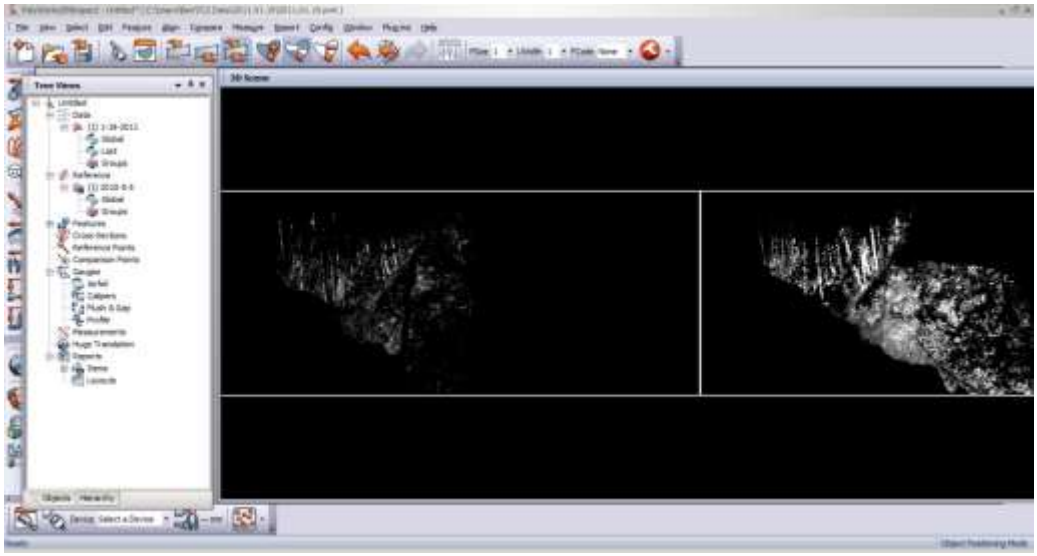

- Working with one data set and the *reference*, I performed a preliminary alignment using *Align N Pairs of Center Points* and then refined the alignment using *Best-fit Alignment*

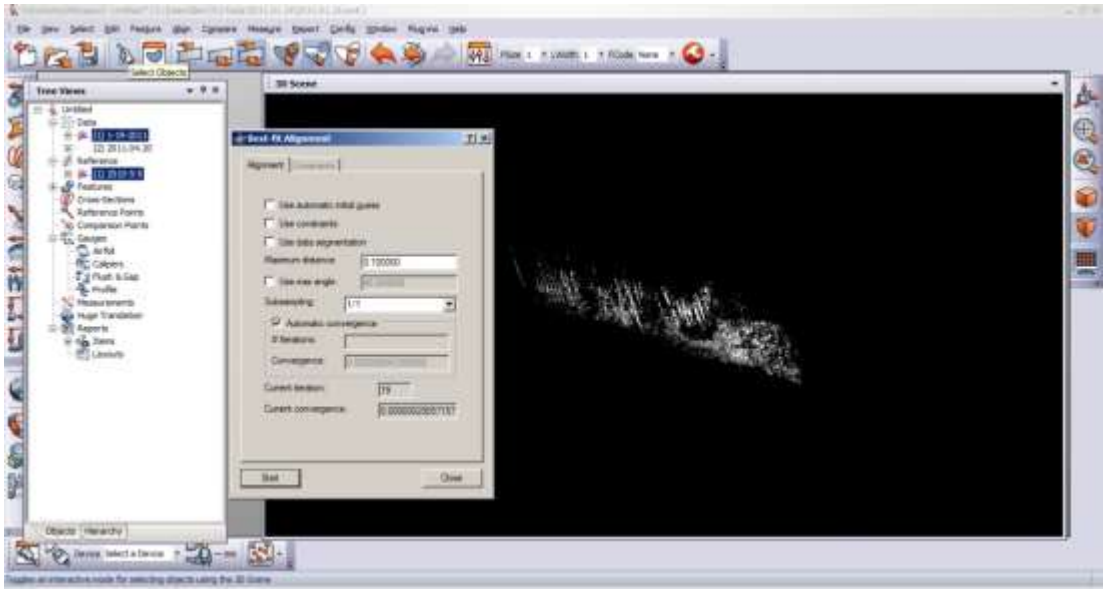

- After a successful alignment (meaning automatic convergence was reached with a max distance .01 m), the unstable terrain was recovered

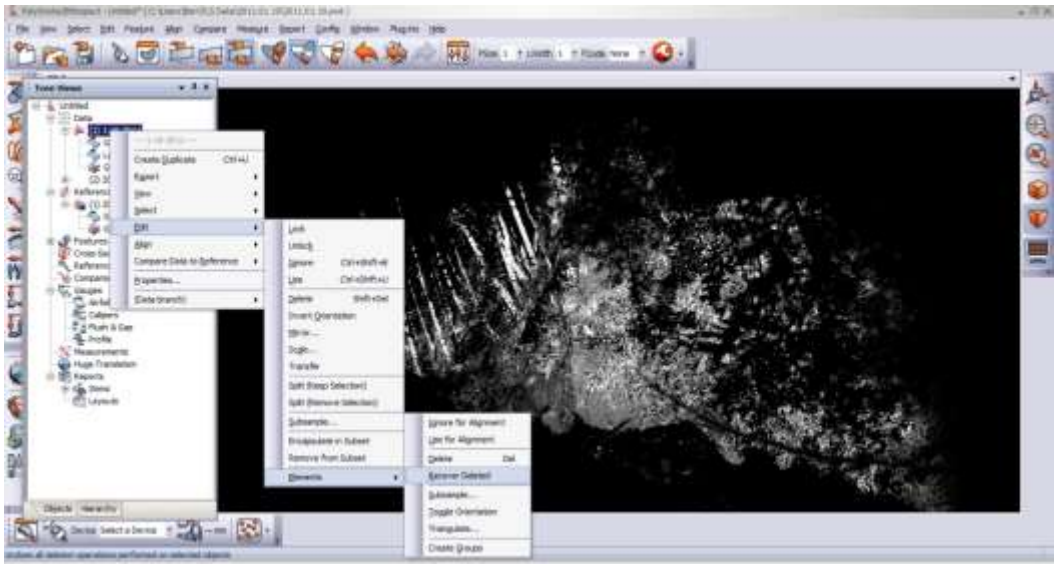

- This process was repeated for each data set
- After all of the data sets were aligned to the previously georeferenced data set, the alignment matrices of the aligned data sets were exported

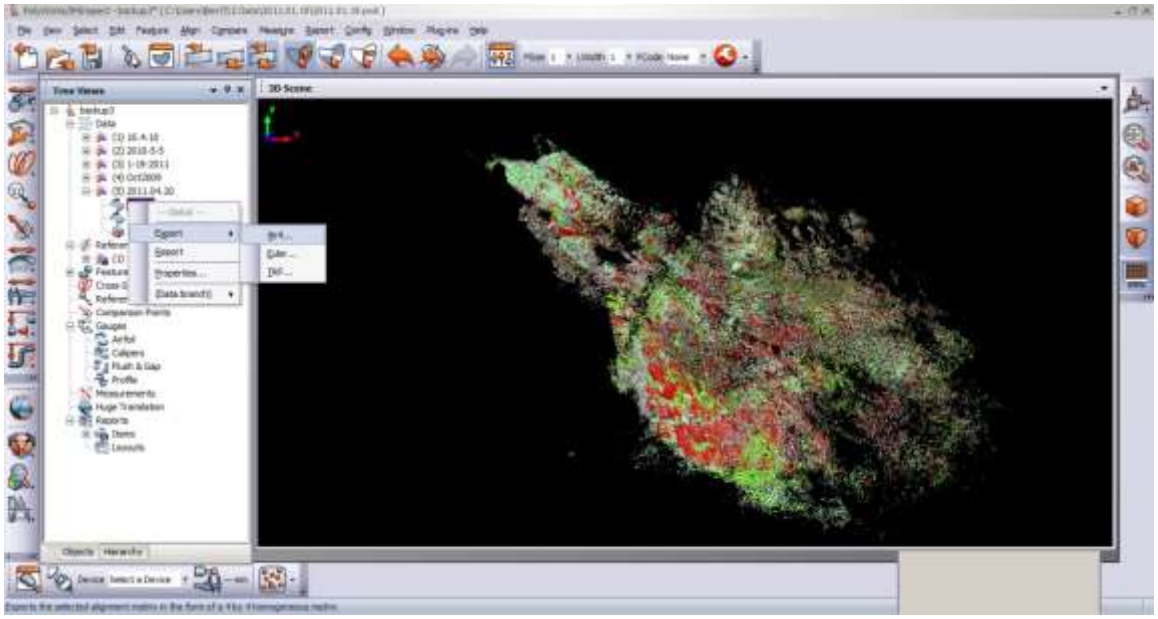

11.3. Verification of alignment

In order to analyze the accuracy of the alignment, a large stable boulder (located near the tip of the toe) was omitted from the alignment process. After the data sets were aligned using IMInspect, the boulder was recovered.

A *data to reference* comparison was completed using the May 2010 data set as the *reference* and the other data sets as *data*. Only areas that were captured in both surveys were used for

the comparison. A maximum distance of 1 m was chosen for the *shortest distance* comparison.

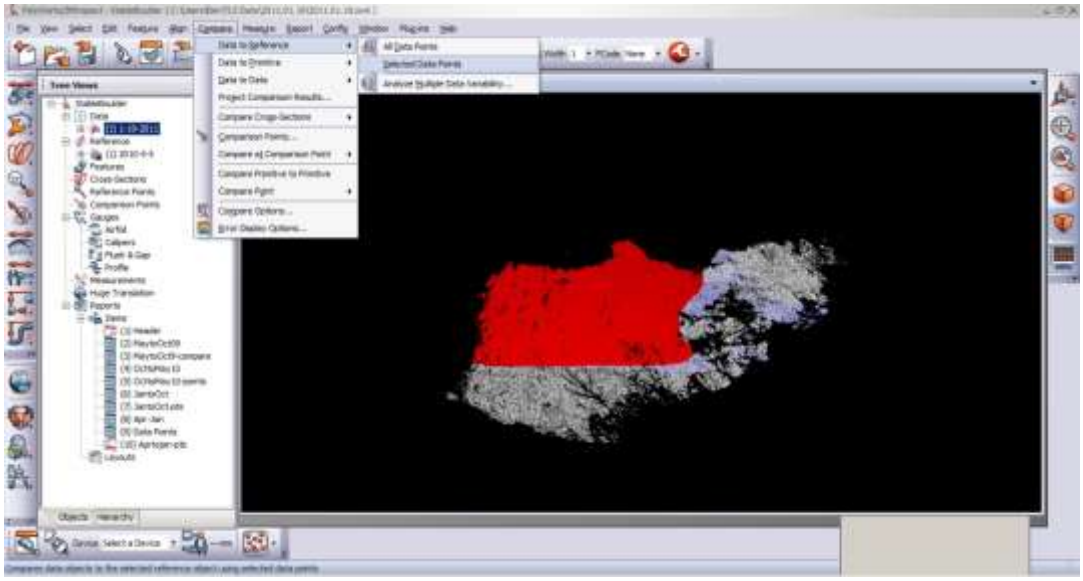

The results of the comparison were recorded in a report. Several thousand points were used in each comparison. The results are shown in **Table 2**.

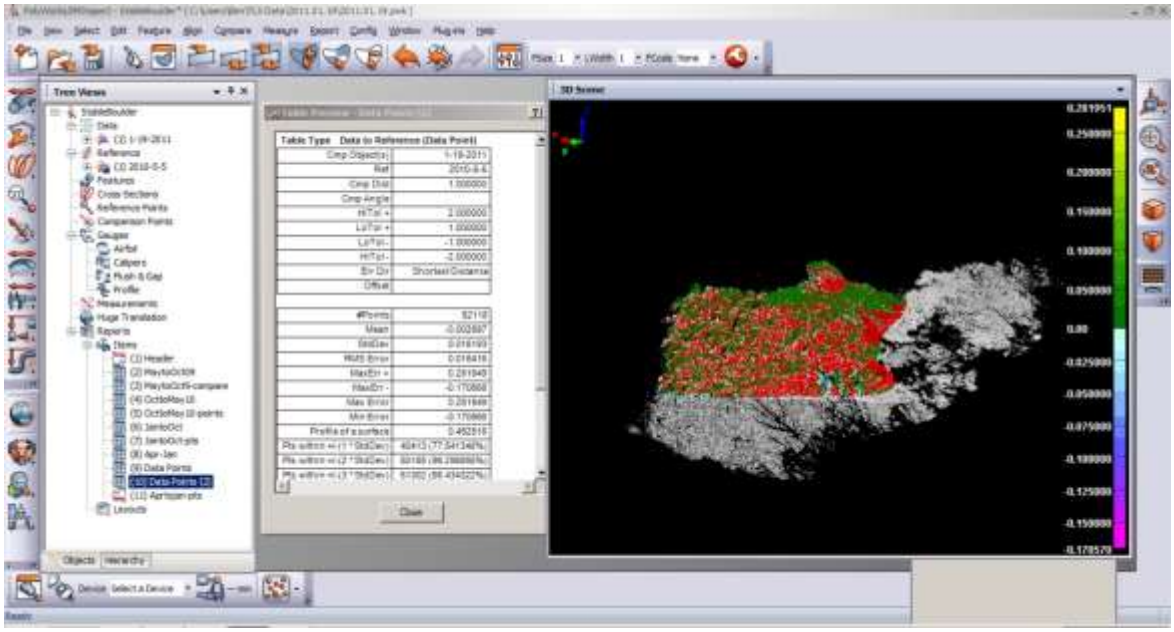

11.4. Measuring individual boulder movement in IMInspect

The process by which I quantified the movement of individual boulders was very similar to the alignment process described in the previous section.

- The datasets were imported into IMInspect and aligned with the alignment matrices obtained in the previous georeferencing steps (using *Align>Matrix>Transform by File* for each data set). It is important to note: the transformational matrices describe a relative change in position; therefore, the original coordinate system is the basis for all of the subsequent transformations. In my case, I first imported the January, 2011 data set during the previous *georeferencing using IMInspect* process; as a result, all of my alignment matrices are based on its coordinate system.

- Each comparison utilized two data sets: the older of the two data sets was imported as *data* and the more recent data set as a *reference*. In this manner, the change in position was recorded as a positive value.

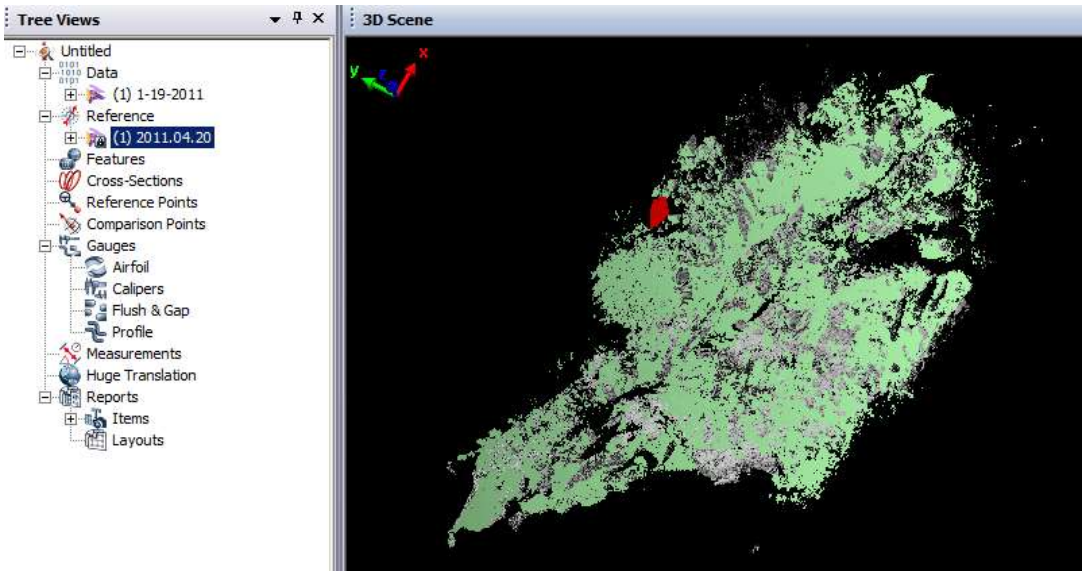

- Each boulder that was identified for monitoring was located in the point clouds and isolated by removing all the other data points

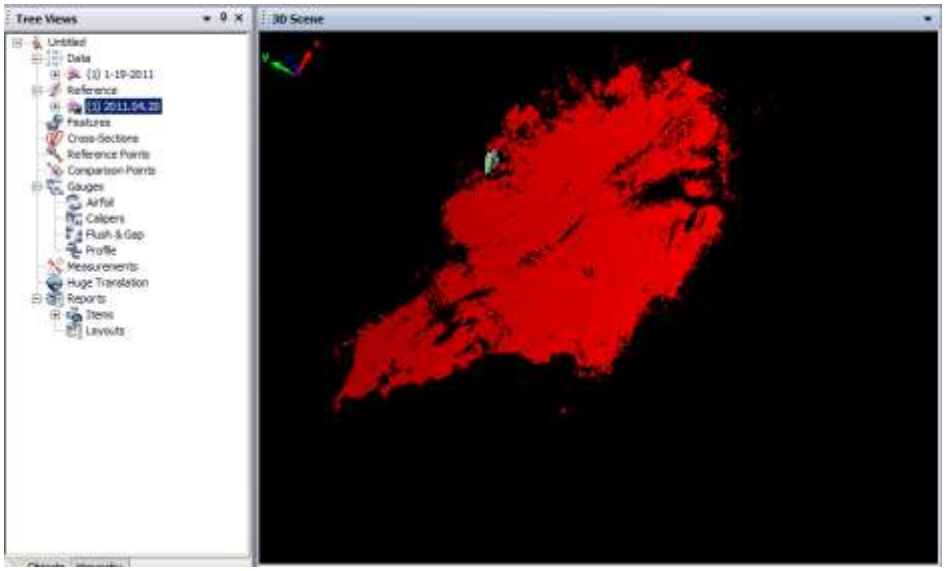

Once the boulder was isolated in all of the data sets, the alignment process was carried out in the following sequence.

- The transformational matrix of the older position (the "before" or *data*) was reset to zero so that the change in position (during the subsequent alignment) from before to after was recorded as the 3D matrix without the need to manually subtract the alignment matrix of the *data* from before and after alignment

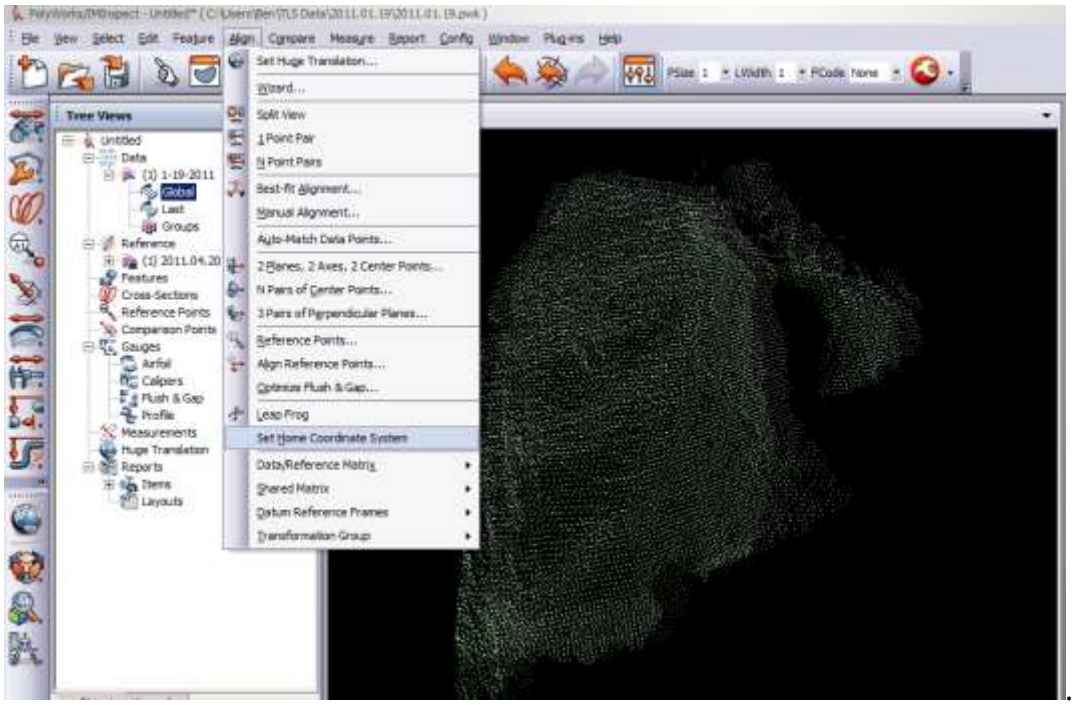

- After resetting the coordinate system of the *data* layer, an initial rough *manual alignment* was completed, followed by a *best-fit alignment.* The variables that described the transformation (i.e., alignment) of the data sets were recorded in the 3D matrix

The same result can be achieved by subtracting the alignment matrices in excel

Aligning January, 2011 to April, 2011

3D matrix of January 2011
Before alignment

0.747	0.627	0.222	54.127
-0.656	0.749	0.091	20.324
-0.109	-0.213	0.971	-524.686
0.000	0.000	0.000	1.000

3D matrix of January 2011
After alignment

0.747	0.627	0.222	53.665
-0.656	0.749	0.091	20.726
-0.109	-0.213	0.971	-524.779
0.000	0.000	0.000	1.000

Matrix Subtraction

0.000	0	0	0.46154
0	0	0	-0.4024
0	0	0	0.09252
0	0	0	0

- To verify the alignment of the displaced boulders, a change comparison was completed in a similar fashion as the stable boulder (using max distance of 1.0 m via *shortest distance* comparison)

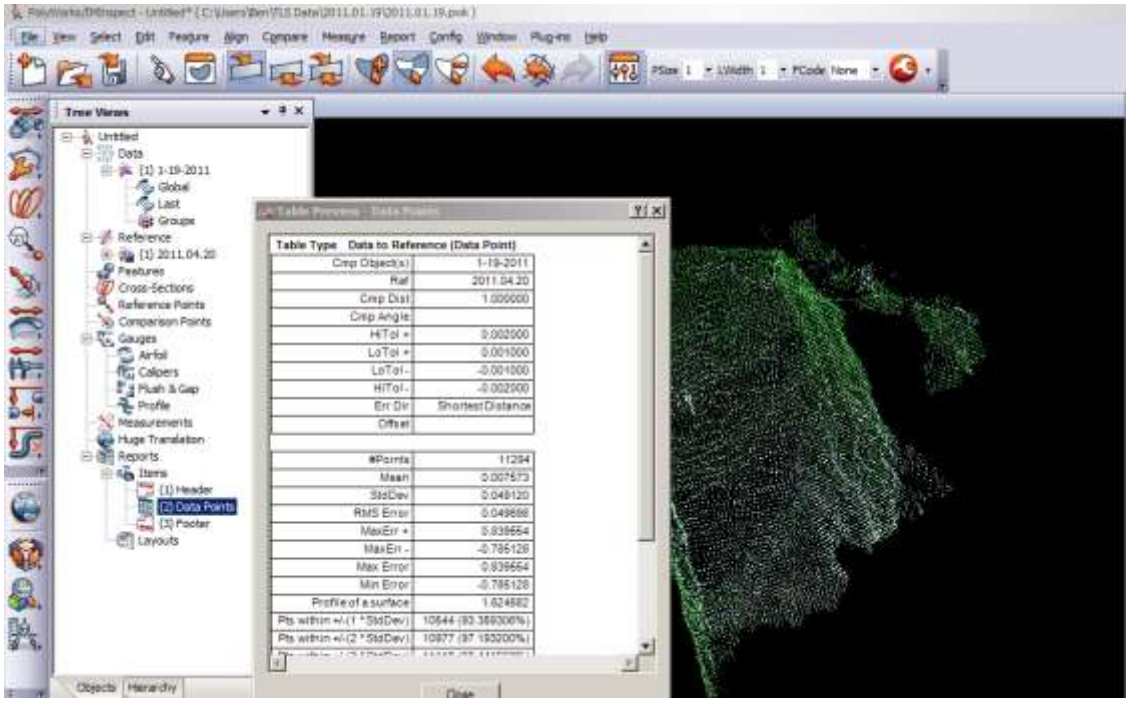

11.5. Creating DEMs from TLS point clouds

The georeferenced data sets were exported from IMInspect to text files in ascii format

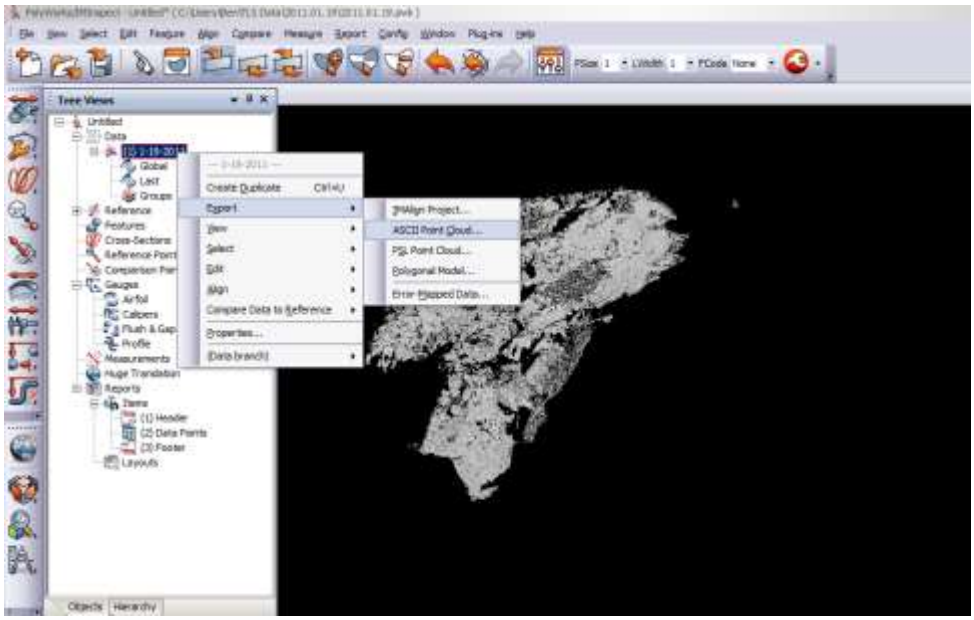

The ascii point cloud files were then imported into ArcGIS 10.1 as *features* using the ArcToolbox (*3D Analyst >conversion >from File >ASCII 3D to Feature Class*).

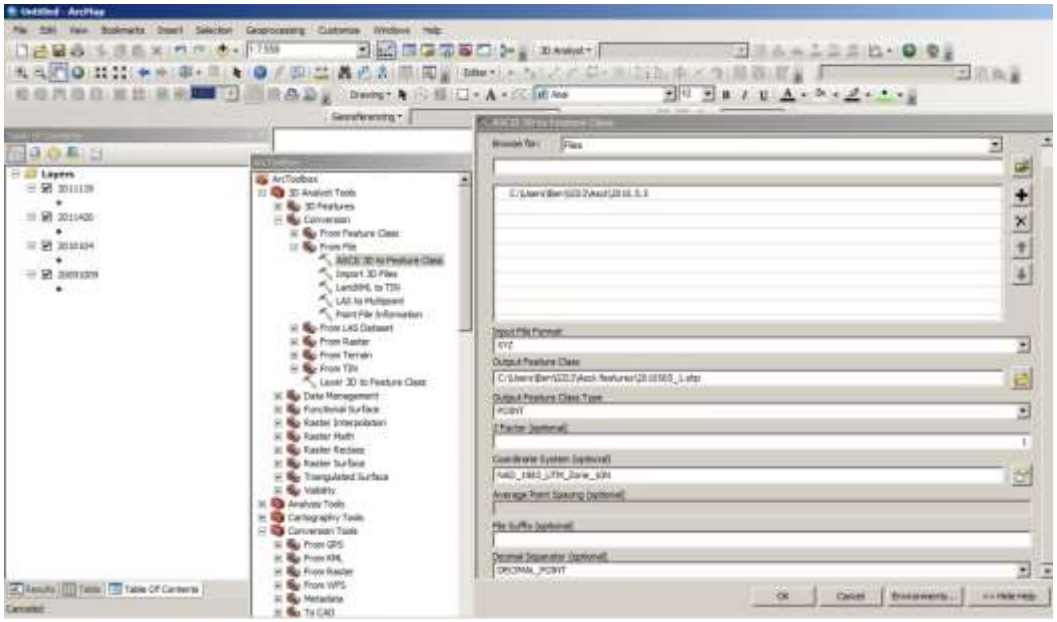

The point features were then interpolated to 0.1 m gridded raster images based on a natural neighbor function (*ArcToolbox >3D Analyst >Raster Interpolation >Natural Neighbor*)

A shape file representing the area captured in each survey was then applied as a mask to the interpolated raster image. This was done to remove interpolation over areas with no point data.

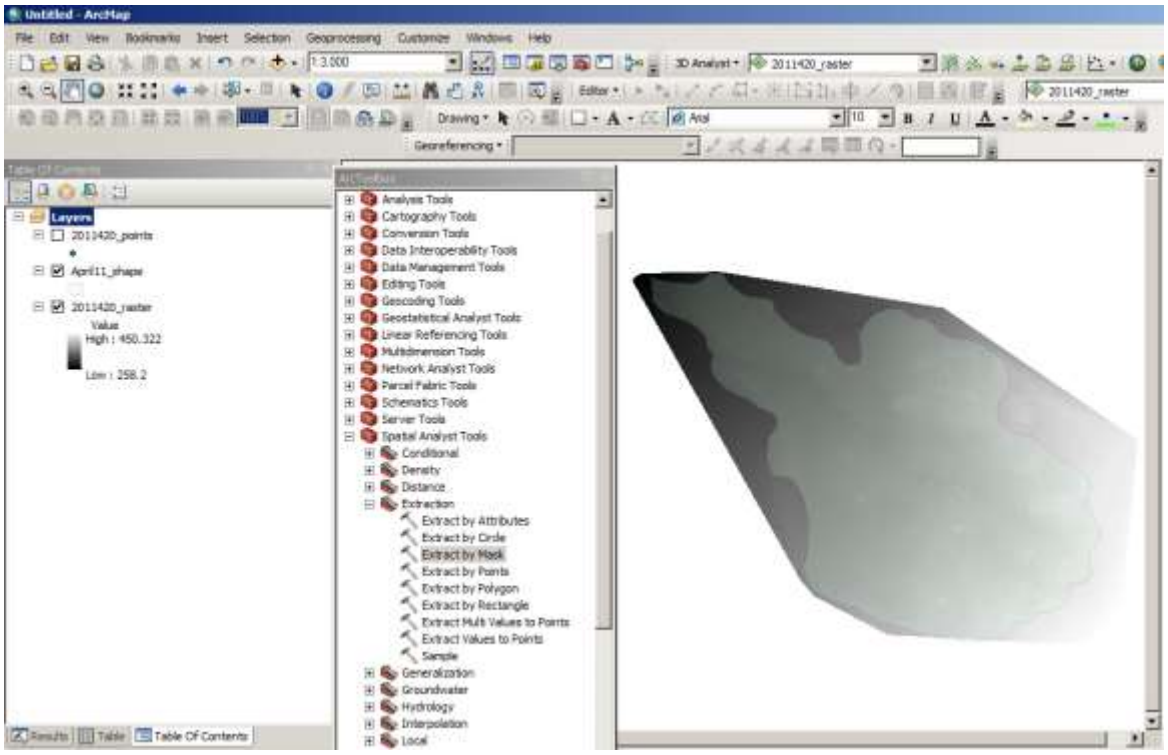

11.6. Applying PIV to TLS data

The TLS DEMs (produced in the previous section) formed the basis for further interpolation using the freeware program PIVlab in MATLAB. The first step was to produce a derived slope-gradient map (*ArcToolbox >3D Analyst >Raster Surface>Slope*). The output of the map was in degrees (0-90). The data was presented in a *stretched* symbology, with a black and white (greyscale) color band.

The greyscale slope-gradient image pairs (before and after) were them imported into PIVlab in MATLAB.

The image pairs were analyzed using a Fast Fourier Transform (FFT) algorithm within the PIV application. I chose an interrogation area of 180 pixels and a step spacing of 60 pixels in a single pass.